



Universidade Federal do ABC
Centro de Ciências Naturais e Humanas
Programa de Pós-Graduação em Física

Pulse modulation for enhanced control in NMR-based Quantum Devices

Gustavo Café de Miranda

Santo André - SP, Janeiro de 2024

Gustavo Café de Miranda

Pulse modulation for enhanced control in NMR-based Quantum Devices

Dissertação de Mestrado apresentada
ao Programa de Pós-Graduação em Física
(área de concentração: Informação Quântica),
como parte dos requisitos necessários para a
obtenção do Título de Mestre em Física.

Universidade Federal do ABC – UFABC
Centro de Ciências Naturais e Humanas
Programa de Pós-Graduação em Física

Supervisor: Prof. Roberto Menezes Serra

Santo André - SP
Janeiro de 2024

Gustavo Café de Miranda

Pulse modulation for enhanced control in NMR-based Quantum Devices/
Gustavo Café de Miranda. – Santo André - SP, Janeiro de 2024-
150 p. : il. (algumas color.) ; 30 cm.

Supervisor: Prof. Roberto Menezes Serra

Dissertação (Mestrado) – Universidade Federal do ABC – UFABC
Centro de Ciências Naturais e Humanas
Programa de Pós-Graduação em Física, Janeiro de 2024.

1. Controle Quantico Ótimo. 2. RMN. I. Roberto Serra. II. Universidade
UFABC. III. Faculdade de Física. IV. Pulse modulation for enhanced control in
NMR-based Quantum Devices

CDU 02:141:005.7



MINISTÉRIO DA EDUCAÇÃO
Fundação Universidade Federal do ABC
Avenida dos Estados, 5001 – Bairro Santa Terezinha – Santo André – SP
CEP 09210-580 · Fone: (11) 4996-0017

FOLHA DE ASSINATURAS

Assinaturas dos membros da Banca Examinadora que avaliou e aprovou a Defesa de Dissertação de Mestrado do candidato, GUSTAVO CAFÉ DE MIRANDA realizada em 19 de Janeiro de 2024:

Documento assinado digitalmente
gov.br CELSO JORGE VILLAS BOAS
Data: 19/01/2024 19:23:48-0300
Verifique em <https://validar.itd.gov.br>

Prof.(a) CELSO JORGE VILLAS BOAS
UNIVERSIDADE FEDERAL DE SÃO CARLOS

Documento assinado digitalmente
gov.br ROBERTO SILVA SARTHOUR JUNIOR
Data: 22/01/2024 11:20:38-0300
Verifique em <https://validar.itd.gov.br>

Prof.(a) ROBERTO SILVA SARTHOUR JUNIOR
CENTRO BRASILEIRO DE PESQUISAS FÍSICAS

Prof.(a) JONAS FLORIANO GOMES DOS SANTOS
UNIVERSIDADE FEDERAL DA GRANDE DOURADOS

Prof.(a) NORTON GOMES DE ALMEIDA
UNIVERSIDADE FEDERAL DE GOIÁS

Documento assinado digitalmente
gov.br ROBERTO MENEZES SERRA
Data: 19/01/2024 17:12:30-0300
Verifique em <https://validar.itd.gov.br>

Prof.(a) ROBERTO MENEZES SERRA
UNIVERSIDADE FEDERAL DO ABC - Presidente

* Por ausência do membro titular, foi substituído pelo membro suplente descrito acima: nome completo, instituição e assinatura

"O presente trabalho foi realizado com apoio da Coordenação de Aperfeiçoamento de Pessoal de Nível Superior - Brasil (CAPES) - Código de Financiamento 001"

ou

"This study was financed in part by the Coordenação de Aperfeiçoamento de Pessoal de Nível Superior - Brasil (CAPES) – Finance Code 001"

*Dedico este trabalho aos meus pais, Lígia e Marcos.
This work is dedicated to my parents, Lígia and Marcos.*

Acknowledgments

I am grateful to my parents, Lígia and Marcos, for their presence in my life, their support, and for believing in my most unexpected professional choices whichever they were, I am who I am thanks to you; To my godfather, Beto, for the ever amazing conversations, laughter, and for being my main reference of a truly joyful scientist; To Carlos and Jefferson for making a great team during unending experimental days (and nights) at the spectrometer.

Finally, I would also like to thank UFABC for financing, in 2.5 years, my studies and this research via the UFABC stipend.

“If a lion could speak, we would not understand him”
(Ludwig Wittgenstein)

“I have long been curious – I had a very bizarre project at one point of trying to make a game that a cat could win against its owner [...] is there a ‘cat-chess’, where cats could play against each other, and if we tried to play a cat we’d always loose?”
(Stephen Wolfram)

“ita et vos per linguam nisi manifestum sermonem dederitis quomodo scietur id quod dicitur eritis enim in aera loquentes tam multa ut puta genera linguarum sunt in mundo et nihil sine voce est si ergo nesciero virtutem vocis ero ei cui loquor barbarus et qui loquitur mihi barbarus”

E assim se vós entregásseis por meio da linguagem um discurso sem clareza, da mesma maneira se compreenderá o que se diz como se falasse ao vento. Mesmo existindo variadas linguas inteligíveis, nenhuma existe sem a voz. Porém se desconheço as virtudes da voz, serei eu mesmo como um estrangeiro ao falar, e será como um estrangeiro aquele que me fala. (Paulus, Ad Corinthios 14:9-11)

“A change in definition is a change of technique”
(Ludwig Wittgenstein – Lectures on the Foundations of Mathematics)

Resumo

Neste trabalho, é fornecida uma revisão sobre os métodos de controle de qubit em computação quântica por RMN. É dada ênfase significativa à utilização de pulsos modulados para aprimorar o controle do qubit e a fidelidade de portas lógicas, discutindo como vários aspectos do controle do qubit podem ser otimizados: atenuação dos efeitos prejudiciais do ruído, como inhomogeneidades no campo magnético, erros de calibração e compensação da largura espectral dos pulsos de RF. Uma atenção especial é dada ao emprego da análise de séries de Fourier no design de pulsos modulados para superar certos efeitos, como a Propriedade de Dilatação e o Fenômeno de Gibbs. Através da simulação de qubits de RMN e métodos de otimização, os melhores pulsos numéricos para sistemas homonucleares e heteronucleares são identificados. Embora numericamente, os pulsos alcancem alta fidelidade, seus resultados experimentais, conforme testados em Clorofórmio em um espectrômetro Varian de 500MHz, são considerados satisfatórios em média. Além disso, é fornecida uma discussão sobre sistemas quânticos abertos e matrizes de Choi. Foi desenvolvido um algoritmo determinístico para a Tomografia Quântica de Processos para acessar o ruído típico para qubits no espectrômetro. Matrizes de Choi experimentais foram então identificadas, e o ruído correspondente agora é incorporado na otimização dos pulsos. As reexecuções dos pulsos com a robustez de ruído incorporada não foram testadas no espectrômetro devido a limitações de tempo e foram deixadas para pesquisas futuras.

Palavras-chaves: Controle Quantico Ótimo. RMN. Tomografia Quântica de Processos.

Abstract

In this work an oversight on qubit control methods in NMR quantum computing is provided. Significant emphasis is placed on the utilization of modulated pulses to enhance qubit control and logic gate fidelity, discussing how various aspects of qubit control can be optimized: mitigation of the detrimental effects of noise such as inhomogeneities in the magnetic field, calibration errors, and compensation of the spectral width of RF pulses. Special attention is given to the employment of Fourier series analysis in the design of modulated pulses to overcome certain effects, such as the Dilation Property and the Gibbs Phenomenon. Through simulation of NMR qubits and optimization methods, the best numeric pulses for both homonuclear and heteronuclear systems are identified. Although numerically, high fidelity is achieved by the pulses, their experimental results, as tested on Chloroform in a 500MHz Varian spectrometer, are found to be satisfactory on average. Moreover, a discussion on quantum open systems and Choi matrices is provided. A deterministic algorithm for Quantum Process Tomography was developed to access the typical noise for qubits in the spectrometer. Experimental Choi matrices were then identified, and the corresponding noise is now incorporated in the optimization of the pulses. Reruns of the pulses with the incorporated noise robustness were not tested in the spectrometer due to time limitations, and are left for future research.

Keywords: Quantum Optimal Control, NMR, Quantum Process Tomography

List of Figures

Figure 1 – Comparison in Optical Quantum Memory efficiency	12
Figure 2 – Bit-flip in the Bloch Sphere	25
Figure 3 – Phase flip channel in the Bloch Sphere	26
Figure 4 – Amplitude damping in the Bloch Sphere	29
Figure 5 – Ancilla-Assisted QPT	32
Figure 6 – NMR Scheme	39
Figure 7 – Examples of molecules - Heteronuclear/Homonuclear/Mixed	40
Figure 8 – State vector rotating in Larmor frequency	43
Figure 9 – Iodotrifluoroethylene (Trifluorine) molecule and chemical shift	44
Figure 10 – Change of frame to rotating frame	45
Figure 11 – 12 qubit molecule (mixed system)	50
Figure 12 – A BEC printer	54
Figure 13 – Fourier transform of square function	63
Figure 14 – Fourier transform of multiple square functions	65
Figure 15 – Truncated Fourier Transform of Sinc() function	66
Figure 16 – GRAPE stepwise	70
Figure 17 – Strong modulation	71
Figure 18 – Gibbs Phenomenon detail	76
Figure 19 – Pulse modulation by Fourier series: Example	79
Figure 20 – Example of stochastic gradient descent with different initial values	80
Figure 21 – Loss function plot (heteronuclear) comparison of three modulations – Dependency on initial values	83
Figure 22 – Three type of pulses – Amplitude and Phase	84
Figure 23 – Loss Function Plot (Homonuclear)- Dependency on interaction hamiltonian (200 μ s)	85
Figure 24 – Loss Function Plot (Homonuclear)- Dependency on interaction hamiltonian (195 μ s)	86
Figure 25 – Initial state for homonuclear system	87
Figure 26 – Final state for homonuclear system under three types of pulses	88
Figure 27 – Ideal frequency overlap	91
Figure 28 – Fourier transform of offsetted modulated pulse	92

Figure 29 – Fourier transform of offsetted pulse	93
Figure 30 – Bloch sphere of multiple offsetted square and modulated pulses (Numerical)	94
Figure 31 – Bloch sphere of multiple offsetted modulated pulses (Numerical) - detailed	95
Figure 32 – Offsetted pulse fidelities (heteronuclear)	96
Figure 33 – Offsetted pulse fidelities (homonuclear)	97
Figure 34 – Loss function for multiple offsets	98
Figure 35 – Loss function for multiple offsets (detailed statistics)	99
Figure 36 – Typical implementation of a C-NOT gate in NMR	101
Figure 37 – Modulated C-NOT circuit (Separated)	102
Figure 38 – Histogram of C-NOT optimization losses	102
Figure 39 – Modulated C-NOT circuits (overlaped)	103
Figure 40 – $\chi^2(U_t, U_g)$ loss function for C-NOT gates of overlapping rotations over J-Coupling	104
Figure 41 – Plot of state Fidelities for the overlapping C-NOT gates	105
Figure 42 – Spectrometer at UFABC	109
Figure 43 – Fidelity by number of Fourier coefficients (Amplitude dependency)	112
Figure 44 – Amplitude limitation	114
Figure 45 – Pulse robustness to small offsets	115
Figure 46 – Comparison of numerical and experimental fidelity for offsetted square pulse	115
Figure 47 – Bloch Plots for numerical and experimental offsetted square pulse	116
Figure 48 – Comparison of numerical and experimental fidelity for offsetted modulated pulse	117
Figure 49 – Bloch Plots for numerical and experimental offsetted modulated pulse	117
Figure 50 – Bloch Plots for numerical and experimental offsetted modulated pulse on $\langle y_+ y_+ \rangle$	119
Figure 51 – Bloch Plots for numerical and experimental modulated pulse on $\langle y_+ y_+ \rangle$ on resonance frequency	120
Figure 52 – Chi Matrix retrived by search algorithm	124
Figure 53 – Choi matrix for Fourier Series pulse - Theory and Experiment	125
Figure 54 – Choi matrix for initial and final state Experiment for the square pulse, and Pauli vector retrieved.	126
Figure 55 – Path on the Bloch sphere for a Fourier series pulse - QPT (Theory)	127
Figure 56 – Path on the Bloch sphere for a Fourier series pulse - QPT (Experiment)	128
Figure 57 – Pauli Noises in time	129
Figure 58 – Stroboscopic QPT (Experiment)	130

List of Tables

Table 1 – Typical T1 and T2 times of Chloroform in NMR	11
Table 2 – Table of pulse fidelities by type	111
Table 3 – Pulse fidelities by coarse graining	113

List of abbreviations and acronyms

BEC	Bose Einstein Condensate
GRAPE	Gradient Ascent Pulse engineering
FID	Free Induction Decay
NMR	Nuclear Magnetic Resonance
QOC	Quantum Optimal Control
QOCT	Quantum Optimal Control Theory
QPT	Quantum Process Tomography
QST	Quantum State Tomography
RF	Radio frequency
RWA	Rotating Wave Approximation

Contents

1	Introduction	1
I	Quantum Mechanics in NMR	7
2	A few elements of Quantum Mechanics and Quantum Channels	9
2.1	Quantum States	13
2.2	Quantum Channels	17
2.3	Axioms of quantum mechanics via quantum channels	20
2.4	Types of Quantum Noise	22
2.5	Quantum Process Tomography	29
2.5.1	QPT in Action	31
2.5.1.1	QPT Example	34
3	The NMR Setting	37
3.1	Hamiltonians in NMR	40
3.1.1	Zeeman Hamiltonian (\mathcal{H}_{Zeeman})	41
3.1.2	RF Hamiltonian (\mathcal{H}_{RF})	42
3.2	Homonuclear Systems	44
3.2.1	Rotating Frame	44
3.3	Heteronuclear systems	47
3.4	Example: Mixed systems	49
II	Quantum Optimal Control	51
4	A few elements of Quantum Optimal Control Theory	53
4.1	Controllability in Quantum systems	54
4.1.1	A note on controllability in open quantum systems	58
5	Signal Processing and Qubit Control	61
5.1	Time and Frequency domain	61
5.2	Modulating pulses in time	63
5.3	A mathematical detour on uncertainty and Fourier transforms	66
5.4	Modulating RF pulses through the GRAPE algorithm	68
6	Modulating RF pulses by Fourier Series	73
6.1	Fourier Series and discontinuous functions	73
6.1.1	The Gibbs Phenomenon	75
6.2	Bypassing digital to analog conversion	76

6.3	Numerical Results	80
6.3.1	Initial value dependency	80
6.3.2	Modulation comparisons: the effect of \mathcal{H}_{int} in homonuclear systems	84
6.4	Robustness to resonance offset	89
6.4.1	Multi frequency pulses	89
6.4.2	Robustness to offset (Heteronuclear case)	93
6.4.3	Robustness to offset (Homonuclear case)	96
6.5	Two Qubit Gates	100
III Experiments in NMR		107
7 Experimental Results		109
7.1	Varying Pulse type	111
7.1.1	Oscillatory limits of RF generator	111
7.2	Varying time and number of points	113
7.3	Robustness to frequency offset	114
7.4	Experimental Quantum Process Tomographies	119
7.4.1	An inverting algorithm for QPT	120
7.4.2	Experimental Results	124
7.4.3	Adding noise to the control optimization	131
IV Conclusion and further research		133
Conclusion and Future Research		135
Bibliography		141
Appendix		147
APPENDIX A Appendix 1: Wilbraham-Gibbs Constant in the square function example		149

Chapter 1

Introduction

Nuclear Magnetic Resonance (NMR) Quantum Computing is a sophisticated field that combines principles from quantum mechanics, computer science, and NMR spectroscopy. It is an interesting platform for tests of principles for quantum computing that uses the nuclear spin states of atomic nuclei as qubits, the fundamental units of quantum information [29, 40, p.7, p.137].

In the realm of quantum computing, qubits are the quantum analog of classical bits. However, unlike classical bits, which can be either 0 or 1, qubits can exist in a superposition of states, allowing them to be in a superposition of 0 and 1, while also providing other quantum resources as entanglement[15, 27, p.11, p.11]. The property of entanglement, when in tandem with interference, is what gives quantum computers their potential for massive parallelism and computational power, but also reveals its weaknesses, as such effects are fragile and may be lost due to the environment coupling and decoherence.

In the density matrix formalism, the state of such a qubit can be represented as:

$$\rho = \begin{pmatrix} |\alpha|^2 & \alpha\beta^* \\ \alpha^*\beta & |\beta|^2 \end{pmatrix} = |\alpha|^2|0\rangle\langle 0| + |\beta|^2|1\rangle\langle 1| + \alpha^*\beta|0\rangle\langle 1| + \alpha\beta^*|1\rangle\langle 0|, \quad (1.1)$$

where ρ is the density matrix of the qubit, α and β are complex numbers called *probability amplitudes*, such that $|\alpha|^2+|\beta|^2= 1$. We call the states in Equation (1.1), when $\alpha = 1, \beta = 0$, the *ground state*, also denoted $|0\rangle$, and the opposite, when $\alpha = 0, \beta = 1$ the *excited state*, also denoted $|1\rangle$. α and β , are not themselves probabilities but allow us to calculate probabilities through what is known as the *Born rule*. This is, sometimes, what is meant by saying that Quantum Mechanics is a probabilistic theory [57, p.55].

In the NMR Quantum Computing field, one leverages the principles of NMR spectroscopy, a technique widely used in chemistry and medicine, to manipulate and read out the states of qubits. The spin states of atomic nuclei can be controlled using magnetic fields and radio frequency (RF) pulses [40, p.33, 137]. In our case these spin

states of atomic nuclei are called qubits, where pulse modulation plays a crucial role. The study of such pulses in NMR is the central topic of this work. The idea is to apply a sequence of precisely timed and shaped RF pulses to the system of qubits to perform quantum operations with optimal control. The timing, shape, and phase of these pulses can be adjusted to achieve precise control over the qubits and perform complex quantum computations [40, p.142].

Modulation RF pulses can be done in a myriad of ways, but not all are useful or experimentally viable. The study of how to control a system by the best change of parameters is called Optimal Control Theory. In this field the equations of motion are parameterized by *controls* that can be manipulated during the evolution of the system externally. This is common practice in the fields of engineering, automation and robotics, where the system has constant external feed-backs that determine where it should follow next. One may think of an automated car that changes its course due to a stream of real-time inputs from a camera attached to the vehicle. How an image input translates to parameters as torque, how much gas must be pumped, and if the system has to pull the breaks, is the study of Classical Optimal Control Theory.

In Quantum Mechanics, however, a measurement changes the system irreversibly, this property makes it impossible to produce real-time feedback, and different strategies than the ones provided by the classical theory are necessary. This leads to the development of Quantum Optimal Control (QOC), a field that studies measurement-free ways of controlling a system. This means that most of QOC relies on strategies that demand that the equations of motion are thoroughly known, and that the control is decided prior to the evolution it acts on. Because in Quantum Mechanics the evolution of a system is determined by its hamiltonian, one way to exercise control is by continuously tuning parameters in the hamiltonian so that the expected evolution is as desired. In experimental practice, such parameters are controlled by RF (or microwave) pulse's amplitude and phase, frequency offsetting, laser interference, external magnetic field gradients, etc.

The decision on the best possible control is usually made by optimization algorithms that computationally minimize metrics of quantum state similarity, as fidelity or distance between unitary transformations, in order to find the best parameters. In the literature one typically finds two well known algorithms: (Gradient Ascent Pulse Engineering) GRAPE and Chopped random-basis (CRAB), that are off the shelf in known Quantum Control Software tools [5, 31]. In our work, we have found that such algorithms, gave unsatisfactory results in NMR devices, as these took long optimization times, optimized on the states (instead of unitary transformations), which causes loss of generality, and produced strong modulated pulses that are inadequate to our experimental apparatus.

Luckily alternative methods are available, and this brings us to the central theme of this work: Fourier-based pulse modulation, designing the pulse sequence in the frequency

domain using Fourier transforms, is a particularly powerful and well tested technique [44]. This approach allows for the design of pulse sequences that can selectively target specific qubits or transitions in a molecule of interest, enabling more precise and efficient quantum operations. The Fourier transform is a mathematical tool that transforms a function of time (or space) into a function of frequency. It is widely used in signal processing and quantum mechanics. A strong advantage comes from the fact that Fourier transforms can be used to design pulse sequences in the frequency domain, which can then be transformed back into the time domain for implementation (this is due to the duality property of Fourier transforms). In this work we have developed an optimization algorithm inspired in this principle to find the best pulses in NMR using Fourier series modulation in order to achieve optimal control. The optimizations were then tested in our 500 MHz spectrometer at UFABC in many different experimental settings as frequency offset, amplitude and phase modulation limits, durations, coarse-graining, etc. By probing this method in various regimes we have found interesting use cases and unexpected results.

Finally, in quantum computing, the computation process is terminated by a measurement, this is typically the NMR spectrum of the system measured by an antenna producing the data from a Free Induction Decay (FID), which can be analyzed via Fourier transforms to determine the states of the qubits [40, 29, p.51, p.50]. Therefore, the use of pulse modulation, and Fourier-based techniques discussed here, must occur prior to the measurement, and acts by subjecting the qubits to the control of operations, leading to more accurate, reliable, and sometimes faster quantum computations.

Moreover, another technique is discussed in this work: Quantum Process Tomography (QPT) [15, 36, 37, p.389], which is a powerful tool used to characterize quantum processes. It involves measuring a quantum system before and after a quantum operation, formally known as a *quantum channel* $\mathcal{E}(.)$, and using these measurements to reconstruct the process matrix, which fully describes the quantum operation in these specific times. Given a quantum channel $\mathcal{E}(.)$, the process matrix is often represented in the Choi matrix form $[\Lambda_{\mathcal{E}}]_{i,j} = \chi_{ij}$, where

$$\mathcal{E}(\rho) = \sum_{i,j} \chi_{ij} E_i \rho E_j^\dagger, \quad (1.2)$$

which provides a convenient and physically meaningful representation of the quantum process [15, p.391]. Characterizing both the unitary (general qubit rotations) and non-unitary (such as bit flips, phase flip, amplitude damping) processes [35].

In the context of NMR Quantum Computing, QPT can be used to characterize how well the quantum operations performed by the radiofrequency pulses. This includes not only the intended quantum operations, but also any unintended effects such as decoherence (caused by the lack of homogeneity in the field, or residual gradients), which can degrade

the performance of the quantum computer. Machine learning techniques can be applied to QPT to learn the process matrix more efficiently and accurately. This can involve training a machine learning model on a set of input-output pairs from the quantum process $\mathcal{E}(\cdot)$, and using this model to predict the output for a new input. The machine learning model can be trained to learn the process matrix directly [53], or it can be trained to learn a parametric model of the process matrix, which can then be optimized to find the best fit to the data. For our purpose, the same principle is applied for a deterministic algorithm that was built to solve this inverse problem. This means that the use of machine learning for this task is not strictly necessary, but to substitute it with a deterministic algorithm more technical additions are needed. We shall see that the deterministic algorithm has some limitations and is unable to give satisfactory results, the possible reasons and solutions for this are discussed, and give way to the possibility that a Machine learning model may possibly overcome such difficulties. This possibility is however left for future endeavors.

Once the process matrix inversion problem is solved, it can be used to improve the performance of the NMR Quantum Computer. One way to do this is by incorporating the acquired process matrix into the Hamiltonian of the NMR system. The Hamiltonian is the operator that describes the energy of the system and determines its time evolution. By incorporating the information gained by the process matrix into the Hamiltonian, we can account for the effects of decoherence and other unintended quantum operations, and design our pulse sequences to mitigate these effects [5], directly on a simulational level. This approach can be used to find better modulated pulses: By incorporating the learned process matrix into the physical Hamiltonian (creating then an effective Hamiltonian that may not be an observable), we can design pulse sequences that not only perform the desired quantum operations, but also minimize the effects of decoherence and other unintended quantum operations. This can lead to more accurate and reliable quantum computations. Although this would be an interesting approach, we have tackled this problem by taking another route: by the Choi matrix, one can skip the learning of complex parameters in the effective Hamiltonian, and apply the non-unitary part of the matrix entirely at the end of the pulse, thereby forcing the pulse optimization to account for decoherence, without explicitly knowing the origin of the noise (this can be called an agnostic to cause approach).

The combination of QPT and Hamiltonian engineering by pulse modulation provides a powerful approach for improving the performance of NMR Quantum Computers, and any other hardware, as it is translatable to other Quantum Devices, such as Superconductor Circuits [5]. By knowing the process matrix of the quantum operations, we can account for the effects of decoherence and other unintended quantum operations, and design pulse sequences to mitigate these effects. This topic shall be discussed more thoroughly in a later chapter in this text.

The text in this dissertation is divided in the following streamlining of information:

Section I is devoted to the theoretical aspects of quantum channels and NMR. In Chapter 2 we discuss some of the fundamentals of open quantum systems and the quantum channels formalism. A short discussion on Quantum Process Tomography (QPT) and Choi Matrices is given. Chapter 3 discusses quantum systems in NMR and gives a construction of the hamiltonians in such systems, giving a special focus to the distinction between heteronuclear and homonuclear systems. In Section II, interest is shifted to Quantum Optimal Control (QOC), the area of research is introduced in Chapter in 4. Then, in Chapter 5, the use of signal processing for control (in a general sense) is discussed, with special attention on Fourier transforms and how one relates frequency and time domain. In the end of this chapter the GRAPE algorithm is scrutinized, as it is a cornerstone of pulse engineering. Moving to Chapter 6 a solution for Quantum Control by Fourier series is presented. The chapter begins by the most common issues of strong modulations and digital to analog conversion, which are later shown to be solvable with Fourier series modulation. Our Numerical results are then presented, and discussions on different optimization strategies and effects of our hamiltonian model in the modulation are taken into account. In the end, numerical tests for resonance offset in pulse modulation are further presented. In Section III the experimental results of the prior discussions are shown. Chapter 7 gives experimental results for variations in pulse type, tests on the RF limits, coarse graining and robustness to frequency offset, providing empirical validation to the theoretical frameworks discussed. At the end of the chapter, experimental results for quantum process tomography of the modulated pulses are shown. In the last Section (IV), we give some considerations on the results obtained and how further research could be followed through. This dissertation is supplemented with an appendix, which provides additional depth on specific topics such as the Wilbraham-Gibbs constant in the square function example.

Part I

Quantum Mechanics in NMR

Chapter 2

A few elements of Quantum Mechanics and Quantum Channels

A lot of material is already available in the topic of Quantum Mechanics. This theory is already more than a century old and surely has achieved a level of both formalism and applications that were unfathomable to the scientists that first pioneered it¹ [49]. An undergraduate physicist at the end of her major should already be quite familiar with it in the setting of closed quantum systems, as it surely went through much of the standard books such as Sakurai's Modern Quantum Mechanics [47], Ramamurti Shankar's books [51], Cohen-Tannoudji's [16], Le Bellac [33] (the authors personal favorite) and many others. Another presentation of the research field in the same terms as the references cited, would not be of great addition, as the endeavor of producing a text of equal brilliance on this framing would surely fail. Specially if written by a Master candidate as myself. Therefore, in this Section I wish to provide the reader with something different: The following pages will provide an introduction to the formalism of open quantum systems, via quantum channel formalism. This is a topic that is not usually covered in the books cited above², but is the standard language of Quantum Information Processing, so it covers, in a graduate level, a nice addition to the knowledge gained by the interested undergraduate reader.

As stated above, most of Quantum Mechanics that is taught in undergraduate courses focuses in closed systems, as these have nice analytical results and are surely quite enough for a semester course in Physics. However, such systems are only approximately true, in the sense that can only be used whenever one can disregard the interaction with the environment. One of the central questions of modern Quantum Mechanics is then: how does one add the environment to the formalism, making it possible to speak of Open

¹ Erwin Schrödinger famously said “In the first place it is fair to state that we are not experimenting with single particles, any more than we can raise Ichthyosaura in the zoo.”, an affirmation that is very much outdated since the advent of single atom trapping – which resulted in the Nobel prize of 1997 (cooling and trapping atoms) and 2012 (single atom manipulation)

² Although some of them give nice introductions to the subject in an undergraduate level.

Quantum Systems, and how closed systems can be described as a special case of this larger theory.

Moreover, this new formalism should be able to explain exactly how are the dynamics that take one case to the other, i.e., when an open system can be approximated by a closed one, or when a closed system can no longer be considered as such. This is where a central definition in the field comes in: *Decoherence*. In simple terms, decoherence is the observed effect that Quantum Systems lose many of their signature properties (such as interference, coherence, entanglement) when interaction with the environment is present [15, 57, p.398, p.111]. This process is sometimes referred as the “classicalization” of the system, we will however avoid this terminology as quantum systems that are “classicalized” are not classical systems, and hence the terminology can be misleading. A somewhat better wording is to say that, quantum systems are probabilistic by nature, such probability rules are, however, very much different from usual probability theory, as the domain space of the probability function is a complex Hilbert space (i.e, $p : \mathcal{H} \rightarrow [0, 1]$) , so when one says that the system suffers “classicalization” what is meant is that the probability functions domain becomes similar to a classical probability distribution (i.e, $p : \mathbb{R} \rightarrow [0, 1]$). This is still only partially true, as the reader may realize by reading through the rest of this Chapter.

Much can be said about when and where decoherence is present. In the case of collider Physics, some authors argue that decoherence occurs very rapidly even in short interaction times [39], as the number of particles is very large and interactions are quite strong (being mediated by the strong force). It could be argued that the number of interactions in large colliders are so large, and strong, that decoherence times become very short, so that usual approximations (e.g., to formally integrate over infinitely long time) used for calculating scattering cross sections of many particles imply that the states are fully decohered when measured ³, these approximations makes the problems sufficiently tractable so that one can focus on observables of interest like cross-sections, decay rates, particle spectra, and the S-matrix [32, 39]. However, in other fields of high energy Physics decoherence is of special importance when studying quantum systems that show entanglement and coherence: e.g. the context of black hole and quantum information [1] for the former, and neutrino oscillations [25] for the latter.

But what about systems that decohere slowly, relatively to the system interactions? Let us give some estimates on time in Quantum Mechanics to gain some intuition: A typical undergraduate example of durations in quantum mechanics is given by the ammonia inversion frequency, that is about 23.79 GHz [22, p.204]. This means that a typical period

³ In technical terms, the density matrix of N-particles is diagonalized and off-diagonal terms (interference terms) vanish. When dealing with particle colliders, the dynamics of the jets (collimated streams of hadrons arising from dynamics of the strong force at high energies) itself lead to decoherence and may wash out nearly all observable traces of interference.

in a quantum system is about 0.26 ns. If the interaction time with the ambient in such a system is about 1000 or 10000 times slower (but still very fast!), let us say 2.6 μ s, then some of the quantum correlation properties and quantum probability distributions could be sustained in many cycles. This is an unusual, but familiar, example, let us provide a more standard one below.

A graduate level example is given by the object of study of this dissertation: NMR qubits. A nuclear spin is also a quantum system, and, when it is $1/2$ and under the influence of a external magnetic field, its energy levels can be labeled *up* or *down* according to the orientation of the reference (external) field direction. One can then manipulate the external field to set the state in a up/down superposition, by the nature of superpositions, this state now has the observable property of coherence. The amount of time needed for a system to lose coherence in NMR is called the T2 time⁴, or *spin-lattice relaxation time* [40, p.43]. After a few multiples of the T2 time has passed, the coherence in the system energy eigenbasis is lost as the superpositions phase information is lost.

By talking about T2 time, the reader may have inferred that there is another time threshold called T1, and there is: When manipulating the external field to set the state as up (or down), one can then ask how much time the system stays in the desired state. Because the set states are usually out of equilibrium states, these will naturally return to equilibrium eventually, the time it takes for e^{-1} of the spin population to return to equilibrium is called the *T1 time*, or *spin-spin relaxation time*⁵. It is important to note that T1 time is not necessarily related to coherence (or decoherence for that matter), as it is a measure of how much the collective behavior of relaxation has occurred, and therefore is not directly related to interference. Nonetheless it is an important measure as it tells us how much time one can guarantee that the spins are in the desired direction.

Some typical values of the T1 and T2 times for a Chloroform molecule in NMR are
Table 1 – Relaxation times in the chloroform sample used in our experiments discussed in
Section 7 [6, p.99].

	Hydrogen-1	Carbon-13
T_1 Longitudinal relaxation	7.36 s	10.55 s
T_2 Transversal relaxation	4.76 s	0.33 s

typically in liquid state NMR, these respect the inequality $T1 \geq T2$ [40, p.44]. But things may differ in solid state NMR.

These time thresholds are of special importance for NMR applications, as not only these are examples of how much decoherence affects systems that are isolated and tightly

⁴ To be precise, the T2 time is given when e^{-1} of the population of spins have lost coherence. Because in NMR the experimental situation is such that some Avogadro numbers of spins are available, one can then consider that around a few multiples of T2 are enough to consider that the system decohered.

⁵ In NMR terms we say that the *the magnetization has relaxed*.

controlled, but are also commonly used to characterize materials, as these indicate how broad resonance lines are. As will be shown in the Chapter 5, the application of gates in NMR quantum computing range from $10\text{ }\mu\text{s}$ to 10 ms , so, dividing T2 by the larger one of these, gives us a minimum and maximum number of 500 to 476000 gates for Hydrogen and 33 to 33000 for the Carbon-13 in the chloroform example.

On a side note, there are quantum systems dedicated to the maximization of decoherence times (T_1 in this case). Such devices are known as *Quantum Memories*, because their major use cases are not focused in controllability of the system, but in storage of its information or state. Quantum Memories are a nice addition to this discussion as they provide an experimental achievement of unprecedented precision, and give us an idea of what is attainable in terms of coherence times. In the literature, one finds very long coherence times: 10 minutes [56] and 6 hours [59] for Yterbium atoms in ion traps quantum devices. In other platforms things may differ: Figure 1 shows a comparison table restricted to light-matter realizations of Quantum Memories,

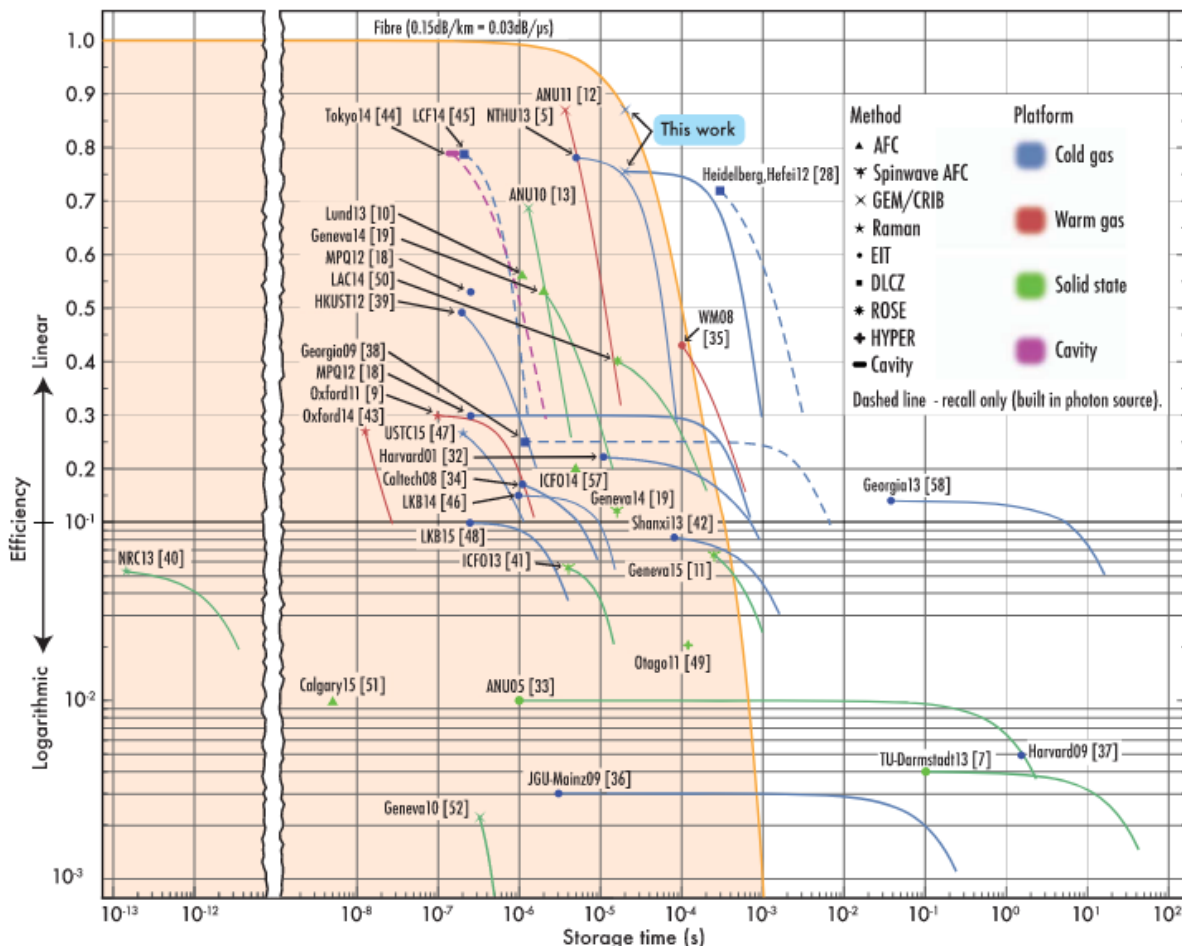


Figure 1 – Figure from [14] (dated 2016) shows a comparison of the efficiencies and storage times of quantum memories that output an optical state. The data plotted is restricted to memories that have the capacity of capture-release a quantum state (solid lines) and recall-only (dashed lines).

The importance of discussing these numbers early on is to give the reader a rough idea of time limitations in quantum devices, and how much decoherence plays a major role in determining the time scale of these processes. The formalism of Quantum Channels and Quantum Maps was created in order to study and deal with noise in this setting, through an information theory framework [15, p.353]. In the following sections we will discuss this formalism and provide the axioms of Quantum Mechanics through the goggles of Quantum Information Theory.

We end this introduction by noting that decoherence is not only a function of time as the prior discussion may have lead to believe. Decoherence is mostly determined by interactions with the environment, and so by how strong and how many of such interactions exists. As a relevant example to this dissertation, decoherence may be also caused by: unintended fluctuations in the control system, due to instability and range limitations of the used electronic; or by inhomogeneities in the magnetic field surrounding the qubit; or by laser intensity, etc. Notwithstanding, the exact limits of when and where decoherence occurs are still elusive. As it is still possible to observe coherence in systems that are on the boundary of quantum to classical physics. This is the case with Mesoscopic Physics and the much known result of coherent light backscattering [2, 3], where coherence quantum effects still occur, but the system is large compared to the systems discussed in this text.

2.1 Quantum States

The main object of study of Theoretical Quantum Mechanics are the *states*. The reader with a background in Physics may remember that usual undergraduate texts refer to the state as a *ket* in a Hilbert space, i.e., $|\psi\rangle \in \mathcal{H}$. This formalism only works for closed quantum systems, and so will be regarded only as a special case of the *density matrix formalism*, below. In this informational setting we shall refer to the state as a density operator, following the definitions in [57, p.105]

Definition 2.1.1 (Density Operator). *The density operator ρ corresponding to an statistical ensemble $\mathcal{E} \equiv \{p_X(x), |\psi_x\rangle\}_{x \in \mathcal{X}}$ is defined as*

$$\rho \equiv \sum_{x \in \mathcal{X}} p_X(x) |\psi_x\rangle \langle \psi_x|, \quad (2.1)$$

particularly,

Definition 2.1.2 (State). *A density operator ρ is called a state when it is positive semi-definite and has trace equal to one. The set of all states in the Hilbert space \mathcal{H} is denoted by $\mathcal{D}(\mathcal{H})$.*

By positive semi-definite, we follow the usual definition as

$$\langle \varphi | \rho | \varphi \rangle \geq 0 \quad \forall \varphi \in \mathcal{H}, \quad (2.2)$$

or more commonly by requesting that all eigenvalues are larger or equal to zero. The trace requisite is to ensure that the density matrix gives a probability distribution where the probability amplitudes (by using the Born rule) all add up to one.

$$\sum_{x \in \mathcal{X}} p_X(x) = 1. \quad (2.3)$$

Some care should be taken with these definitions, as the class of density operators is non bijective with the one on statistical ensembles. More formally: for every statistical ensemble there is a unique density operator, but a given density operator could be produced by many different ensembles, [57, p.106].

Let us give some examples. The simplest distribution, and usually the first example in probability theory is the uniform distribution, where $p(x) = 1/|\mathcal{X}|, \quad \forall x \in \mathcal{X}$, the density operator that corresponds to this ensemble is the one where all orthogonal states are equally possible, also called the *maximally mixed state*

$$\rho = \frac{1}{|\mathcal{X}|} \sum_{x \in \mathcal{X}} |x\rangle\langle x| = \frac{1}{|\mathcal{X}|} \mathbb{I}. \quad (2.4)$$

In the simpler case of $\{|x\rangle\}$ being an orthonormal basis, the state is then made of distinguishable parts, as these can be separated by straightforward projection of operators $\{|x\rangle\langle x|\}$, for each x . This is true even if the state is not in a uniform distribution, as in Equation (2.1). This state is sometimes called “classical”, but this terminology may be misleading, as it can still have properties that would be indubitably called ‘quantum’ (e.g., coherence between matter waves; and also the fact that quantities in Quantum Mechanics are measure-dependent, in the sense that the choice of measurement basis gives different outcomes). Because the kets $|x\rangle$ are orthonormal, then the operator is diagonal in this basis and its diagonal is the exact probability distribution of the system.

In undergraduate quantum mechanics courses, usually the sole operator studied is the one for the *pure state*, written as

$$\rho = |\psi\rangle\langle\psi|. \quad (2.5)$$

This state is very special in the field of Quantum Computation, and has a quantity motivated by the problem of characterization of pure states, called *purity*, expressed as

$$\mathrm{Tr}\{\rho^\dagger \rho\} = \mathrm{Tr}\{\rho^2\}. \quad (2.6)$$

One can easily show that pure states respect the following theorem

Theorem 2.1.3. $\mathrm{Tr}\{\rho^2\} = 1 \iff \rho \text{ is a pure state.}$

Whenever a state is not pure, it is called a *mixed state*, and has the general form of the Equation (2.1) in the Definition of a density operator, but now with the restriction that $p_x(x) < 1, \forall x$. In the special case of $\{|\psi_x\rangle\}$ being an orthonormal basis, i.e., $\langle\psi_x|\psi'_x\rangle = \delta_{xx'}$, the purity gives

$$\begin{aligned} \mathrm{Tr}\{\rho_{\text{mix}}^2\} &= \mathrm{Tr}\left\{\left(\sum_{x \in \mathcal{X}} p_X(x) |\psi_x\rangle\langle\psi_x|\right)\left(\sum_{x' \in \mathcal{X}} p_X(x') |\psi'_x\rangle\langle\psi'_x|\right)\right\} \\ &= \sum_{x, x' \in \mathcal{X}} p_X(x)p_X(x') \mathrm{Tr}\{|\psi_x\rangle\langle\psi_x| |\psi'_x\rangle\langle\psi'_x|\} \\ &= \sum_{x, x' \in \mathcal{X}} p_X(x)p_X(x') \mathrm{Tr}\{\delta_{xx'}\delta_{xx'}\} \\ &= \sum_{x \in \mathcal{X}} (p_X(x))^2 \leq 1, \end{aligned}$$

clearly the equality only holds when $p_X(x) = 1$ for exactly one x . This shows that purity is always smaller than one when the state is a mixed state. One can show that for the maximally mixed state in a orthogonal basis in Equation (2.4), the purity is $\mathrm{Tr}\{\rho^2\} = 1/|\mathcal{X}|$, and in this case when there are only two states it gives $\mathrm{Tr}\{\rho^2\} = 1/2$.

Now that the object of study is defined, one could ask how to tell two states apart. Luckily there are many ways to do so. If two states are pure, one could define the the following

Definition 2.1.4 (Pure state fidelity). *If two states are pure, then their pure state fidelity is given by the ket overlap $F(\phi, \psi) \equiv |\langle\phi|\psi\rangle|^2$.*

This would ensure us that, if the two states are orthogonal, then $F(\phi, \psi) = 0$, while also being true that $F(\phi, \psi) = 1$ if and only if both are the same state. Furthermore F is always bounded between $0 \leq F(\phi, \psi) \leq 1$. However, this definition, although a nice one for closed system quantum mechanics, is not sufficient for open systems, and is not defined for a large set of states. To solve this, the most common fidelity used is given by

Definition 2.1.5 (Ullmann Fidelity). *The Ullmann fidelity is given by*

$$F_U(\rho, \sigma) \equiv |\mathrm{Tr}\{\sqrt{\rho}\sqrt{\sigma^\dagger}\}|^2.$$

This fidelity has all of the properties above, while also being applicable to states that are not pure. The following definition is also quite common in paper in the field of Quantum Information

Definition 2.1.6. *The fidelity is given by $F(\rho, \sigma) \equiv \left(\text{Tr} \sqrt{\sqrt{\rho}\sigma\sqrt{\rho}} \right)^2$.*

One can show that this definition is mathematically equivalent to Ulmann's fidelity [57, p.250].

The following consideration is of utmost importance to this work. As the reader may remember, the definition of a function of an operator is given by

$$f(A) = f\left(\sum_a a |a\rangle\langle a|\right) = \sum_a f(a) |a\rangle\langle a|, \quad (2.7)$$

so that $\sqrt{\rho} = \sum_{x \in \mathcal{X}} \sqrt{p_X(x)} |x\rangle\langle x|$. This is well defined in theory, as probabilities are always real and positive. However, it is pragmatically problematic, for the following reason: in experimental situations one does not measure ρ directly, what is measured are expected values of observables and then the density matrix is reconstructed following an algorithmic procedure (called *Maximum Likelihood*, in NMR practice). In Quantum Mechanics, however, some observables are impossible to be simultaneously measured (formally it is said that these observables do not commute), this means that one has to repeat the experiment as many times as there are observables needed to be measured. In NMR this means that a single qubit requires at least two experimental runs [29, p.50] to characterize 4 observables. Due to experimental issues, stochastic noise, and uncertainty in measurement, it is possible that the observables are inconsistent in the sense that the reconstructed matrix has negative eigenvalues. It must be said however that the reconstructed matrix is neither of the two measured ones, but a combination of the two *as if* they were the same experiment run. There are many philosophical consequences to this fact: one could say that the theory is correct and the experiments are inaccurate, so that the tested matrices had, individually, positive eigenvalues, but produced an negative reconstructed one (i.e., reconstructed results are nonphysical. The platonist view); Or one could say that the formalism is incomplete and the experiments are paramount (i.e., matrices in such and such experimental conditions give negative eigenvalues, and the theory is lacking explanatory power, because it can't explain negative eigenvalued states. The empiricist view). We will leave such considerations for the readers intuition and (from an agnostic position) try to solve the pragmatical problem at hand: how can one deal with such negative eigenvalues?

Because the experimental negative eigenvalues are usually quite small, compared to the positive ones, they do not represent the results at large. However, simply removing

them could lead to inaccuracies. In the field of NMR Quantum Information, the solution taken, is to define a fidelity that is defined for negative eigenvalues [12, 23, p.12, p.7600], and that has very similar results to the Ulmann fidelity

Definition 2.1.7 (Fidelity). *In this work the following function is called (simply) Fidelity*

$$F(\rho, \sigma) = \frac{\text{Tr}\{\rho\sigma\}}{\sqrt{\text{Tr}\{\rho\rho^\dagger\}}\sqrt{\text{Tr}\{\sigma\sigma^\dagger\}}}$$

In the remainder of this text, we shall refer to this function, whenever the word *fidelity* is used.

2.2 Quantum Channels

Until now, all that was said about quantum states assumed that all was static and no evolution occurred. The reader may remember that in closed system quantum mechanics the evolution of a system is given by the temporal evolution operator.

$$U(t, t_0) = T_- \exp \left\{ -i \int_{t_0}^t \mathcal{H}(t') dt' \right\}, \quad (2.8)$$

where T_- is a chronological time-ordering operator which orders products of time-dependent operators, increasing in time from right to left [11, p.110]. The operator $U(t, t_0)$ is obtained by solving the famous Schrödinger Equation, and can be directly translated to the open quantum system formalism, restricted that the evolution is unitary, where the state in time t is

$$\rho(t) = U\rho(t_0)U^\dagger. \quad (2.9)$$

A more detailed discussion on open systems and how the dynamics occur could be given here by introducing the Liouville equations and the Lindblad master equations. The reader can refer to [11], for this treatment. In the following we will deal with the system evolution in an *input-output* setting, where we are interested in looking at the state (or their probabilities) before and after it has passed through an evolution (or a ‘channel’), this evolution can still be a continuous one, when input and output are considered close to one another, or when it is parameterized by a continuous variable. In other words, we will work with a formalism of maps of operators. But first let us be clear with some notations:

Definition 2.2.1. *We define $\mathcal{D}(\mathcal{H})$ as the space of density operators in \mathcal{H} , and let $\mathcal{L}(\mathcal{H}_B, \mathcal{H}_B)$ be the space of linear operators acting on \mathcal{H}_A and taking them to \mathcal{H}_B . Moreover we denote $\mathcal{L}(\mathcal{H})$ as the space of square linear operators on \mathcal{H} .*

This said we can now define rigorously what we mean with a Quantum Channel

Definition 2.2.2 (Quantum Channel/Operation). *A map $\mathcal{E} : \mathcal{L}(\mathcal{H}_A) \rightarrow \mathcal{L}(\mathcal{H}_B)$ is called a Quantum Channel when it is linear, completely positive, and trace-preserving.*

Let us clarify each one of these requisites, one by one. Linearity should be clear by now, the map should satisfy this if

$$\mathcal{E}(\alpha X + \beta Y) = \alpha\mathcal{E}(X) + \beta\mathcal{E}(Y), \quad (2.10)$$

where $X, Y \in \mathcal{L}(\mathcal{H}_A)$, and $\alpha, \beta \in \mathbb{C}$.

Definition 2.2.3 (Positive Map). *We say that a map $\mathcal{E} : \mathcal{L}(\mathcal{H}_A) \rightarrow \mathcal{L}(\mathcal{H}_B)$ is positive, if $\mathcal{E}(X)$ is positive semi-definite, whenever X is positive semi-definite.*

For $\mathcal{E}(\cdot)$ to be a positive map, it should be such that it takes positive semi-definite operators to positive semi-definite operators, this property is automatically satisfied if one restricts the domain of $\mathcal{E}(\cdot)$ and its image to the set of $\mathcal{D}(\mathcal{H}_A)$ and $\mathcal{D}(\mathcal{H}_B)$, respectively. In other words, we want $\mathcal{E}(\cdot)$ to take physical states to other physical states and conserve the sign of probability. This restriction can be relaxed, as taking a single state to a single state may be too demanding. For this, we will ask for the more structured property that \mathcal{E} is *convex linear* in the set $\mathcal{D}(\mathcal{H})$. This means that

$$\mathcal{E}(\lambda\rho + (1 - \lambda)\sigma) = \lambda\mathcal{E}(\rho) + (1 - \lambda)\mathcal{E}(\sigma), \quad (2.11)$$

for $\lambda \in [0, 1]$ and $\rho, \sigma \in \mathcal{D}(\mathcal{H})$. The reader may recognize this as the functional form of the (continuous) line between two density operators.

This property has an interesting interpretation that, not only a convex linear combination of states is itself a state (this can easily be checked by taking the trace), but that applying a map on the whole combination is the same as the convex combination of the result states after the map is applied. This means that if a mixture of two states are prepared under the same conditions, then the measured results are equivalent to preparing them first and then mixing. Clearly, if $\mathcal{E}(\cdot)$ is a positive map, then, being convex linear, it is still positive for all convex combinations [57, p.130].

The property of complete positivity we wish to define is more strict than mere positiveness, and has a nice interpretation in quantum systems. The formalism for open quantum systems should be such that the environment is always present in some sense. Suppose then, that $\mathcal{E} : \mathcal{L}(\mathcal{H}_A) \rightarrow \mathcal{L}(\mathcal{H}_B)$ acts on the subspace \mathcal{H}_A while this space is always in contact with the environment, i.e. formally: $\rho_{RA} = \rho_R \otimes \rho_A$. But since the

actor that is preparing a state does not control the ambient, but rather prepares only the subsystem in \mathcal{H}_A over which she has control, the map over the whole system should be given by

$$\mathbb{I}_R \otimes \mathcal{E}(\cdot) : \mathcal{L}(\mathcal{H}_R) \otimes \mathcal{L}(\mathcal{H}_A) \rightarrow \mathcal{L}(\mathcal{H}_R) \otimes \mathcal{L}(\mathcal{H}_B).$$

Where

$$\begin{aligned} (\mathbb{I}_R \otimes \mathcal{E})(\rho_{RA}) &= (\mathbb{I}_R \otimes \mathcal{E})(\rho_R \otimes \rho_A) \\ &= \mathbb{I}_R(\rho_R) \otimes \mathcal{E}(\rho_A) \\ &= \rho_R \otimes \mathcal{E}(\rho_A). \end{aligned}$$

So that this state remains being expressible as a tensor product. The restriction we ask for it to be a Quantum Channel is then that it is

Definition 2.2.4 (Complete Positive Map). *A linear map $\mathcal{E} : \mathcal{L}(\mathcal{H}_A) \rightarrow \mathcal{L}(\mathcal{H}_B)$ is said to be completely positive if the product map $\mathbb{I}_R \otimes \mathcal{E}(\cdot) : \mathcal{L}(\mathcal{H}_R) \otimes \mathcal{L}(\mathcal{H}_A) \rightarrow \mathcal{L}(\mathcal{H}_R) \otimes \mathcal{L}(\mathcal{H}_B)$ is a positive map, for a environment \mathcal{H}_R of arbitrary dimension.*

Now, because we demanded that $\mathcal{E}(\cdot)$ is restricted to the set of density operators, then clearly it preserves the trace, as $\text{Tr}\{\rho\} = \text{Tr}\{\mathcal{E}(\rho)\} = 1$. Because it is the case that the set of density operators $\mathcal{D}(\mathcal{H})$ has a basis for the whole set $\mathcal{L}(\mathcal{H})$ [57, p.132], then as a consequence of $\mathcal{E}(\cdot)$ being a linear map, it can also preserve the trace of any operator in $\mathcal{L}(\mathcal{H})$, by linearity. This is why it was permissible to write the whole set in Definition 2.2.2 instead of only the set of density operators.

An important theorem gives us simple criteria to evaluate if a map is actually a Quantum Channel:

Theorem 2.2.5 (Choi-Kraus). *A map $\mathcal{E} : \mathcal{L}(\mathcal{H}_A) \rightarrow \mathcal{L}(\mathcal{H}_B)$ is linear, completely positive, and trace-preserving if and only if it admits a Choi-Kraus decomposition as follows*

$$\mathcal{E}(X_A) = \sum_{l=1}^d K_l X_A K_l^\dagger, \quad (2.12)$$

where $K_l \in \mathcal{L}(\mathcal{H}_A, \mathcal{H}_B)$, $\forall l \in \{1, \dots, d\}$, and $d \leq \dim(\mathcal{H}_A) \dim(\mathcal{H}_B)$, and the condition

$$\sum_{l=1}^d K_l^\dagger K_l = \mathbb{I}_A, \quad (2.13)$$

holds.

Therefore, quantum channels have a special functional form, and we can then study quantum systems only by delving into maps of this type.

This simple formulation, given by a specific functional form may be making the undergraduate reader scratch his head over how can so few lines store all information of quantum mechanics. We will explore this in a very limited manner in the next sections.

2.3 Axioms of quantum mechanics via quantum channels

The reader may be asking himself how this formalism restores his undergraduate knowledge in Quantum Mechanics. Let us then quickly show, before continuing, how the axioms of closed quantum systems are a special case of this formulation. To do so, we will be writing them one by one and explaining how it is expressed in the Quantum Channels formalism. The postulates below are taken from Nielsen and Chuang's famous book in Quantum Information, and can be retrieved in one page referring to [15, p.102].

Postulate 1: A quantum system is completely described by a density operator $\rho \in \mathcal{H}$, where ρ is positive and with unit trace. If a statistical mixture of states, composed by the states ρ_i with probability p_i , then the density operator is given by $\sum_i p_i \rho_i$.

This postulate is very straightforward, as it is only the definition of state, but now described as a density operator, given in Equation (2.1). As a language abuse, the statistical mixture described by a density operator is often also called a state. It is also said that ρ describes our knowledge about the systems.

Postulate 2: The evolution of a quantum system is described by a unitary transformation, called the time evolution operator U , as in

$$\rho' = U\rho U^\dagger.$$

In this new formulation it can be checked that this is a special case of Equation 2.2.4, when $d = 1$, as then we have

$$\mathcal{E}(\rho) = K\rho K^\dagger.$$

Unitarity given by $\sum_{l=1}^d K_l^\dagger K_l = K_1^\dagger K_1 = \mathbb{I}$.

One may conclude that evolutions in quantum maps have much more possibilities that are not necessarily unitary, the only requisite for this to be true is that $d > 1$.

Postulate 3: Quantum measurements are described by a collection $\{M_m\}$ of *measurement operators*, the index m refers to the outcome that occurs with probability

$$p(m) = \text{Tr}\{M_m^\dagger M_m \rho\},$$

and the state of the system after the measurement becomes

$$\frac{M_m \rho M_m^\dagger}{\text{Tr}\{M_m^\dagger M_m \rho\}},$$

where the measurement operators satisfy the completeness relation

$$\sum_m M_m^\dagger M_m = \mathbb{I}.$$

We can identify $M_m = K_m$, and therefore give an interpretation of the measurements as quantum operations themselves. This is probably the most important aspect of the channels formalism: the measurement is not an *ad-hoc* addition to the theory, measurements *are* quantum processes. This means that projective measurements are the same as restricting $\mathcal{E}(.)$ to $l = m$, and writing $\mathcal{E}_m(\rho) = M_m \rho M_m^\dagger$. Making the following equations true:

$$p(m) = \text{Tr}\{\mathcal{E}_m(\rho)\} \quad (2.14)$$

$$\frac{\mathcal{E}_m(\rho)}{\text{Tr}\{\mathcal{E}(\rho)\}} = \frac{K_m \rho K_m^\dagger}{\text{Tr}\{K_m^\dagger K_m \rho\}}. \quad (2.15)$$

Of course, now the restriction to a single m can be lifted in Equation (2.15), and the resulting state can then be more than a defined state with a single probability (e.g. a superposition, or an entangled state).

Postulate 4: The state space of a composite physical system is the tensor product of the state spaces of the component physical systems. I.e., if we have systems numbered 1 through n , and each system numbered i is prepared in the state ρ_i , then the joint state of the total system is $\rho = \rho_1 \otimes \rho_2 \otimes \dots \otimes \rho_n$.

This last postulate remains unchanged.

The discussion above may give the impression that closed systems are always a special case of open systems, and this is partially true, as we have just shown that the general framework of Quantum channels can express all of closed system Quantum Mechanics. However, some care has to be taken, as there are some subtleties to this relation. The first one is given by the following result: noisy quantum systems can be viewed as a special case of larger noiseless quantum systems [57, p.164]. The same proposition can be stated in more precise wording

Theorem 2.3.1. *For every operator ρ_A on a system A there exists a purification of this operator,*

in the following sense:

Definition 2.3.2 (Purification). A purification of a density operator $\rho_A \in \mathcal{D}(\mathcal{H}_A)$ is a pure bipartite state $|\psi_{RA}\rangle\langle\psi_{RA}| \in \mathcal{D}(\mathcal{H}_R) \otimes \mathcal{D}(\mathcal{H}_A)$, with the property that

$$\rho_A = \text{Tr}_R\{|\psi_{RA}\rangle\langle\psi_{RA}|\}. \quad (2.16)$$

This is quite straightforward to show, as by taking the definition of state in Equation (2.1) and the following product state $|\psi_{RA}\rangle = \sum_x \sqrt{p_X(x)} |x\rangle_R |x\rangle_A$, where $\{|x\rangle_R\}$ is an orthonormal basis of \mathcal{H}_R , the partial trace of this state will output the desired state for the subsystem A . Not only this, but the quantum channel $\mathcal{E}(.)$ can also be retrieved from the larger space by tracing it out.

Suppose the larger system evolves under a unitary evolution $U\rho_{RA}U^\dagger$, and suppose $\{|e_l\rangle\}$ is a basis for \mathcal{H}_R . Also suppose that the environment is in a pure state $\rho_R = |e_1\rangle\langle e_1|$ (there is no loss of generality in doing so). Then

$$\begin{aligned} \text{Tr}_R\{U\rho_{RA}U^\dagger\} &= \sum_{l=1}^{N_R} \langle e_l | U\rho_R \otimes \rho_A U^\dagger | e_l \rangle \\ &= \sum_{l=1}^{N_R} \langle e_l | U | e_1 \rangle \rho_A \langle e_1 | U^\dagger | e_l \rangle \\ &= \sum_{l=1}^{N_R} K_l \rho_A K_l^\dagger \\ &= \mathcal{E}(\rho_A), \end{aligned}$$

where we defined the projection of U on the subspace spanned by $\{|e_l\rangle\langle e_1|\}$, as $\langle e_l | U | e_1 \rangle = K_l$.

This equation gives rise to many interpretations of what exactly is noise in Quantum Mechanics. One possible interpretation, is to say that noise is the loss of information that occurs by tracing out (i.e., ignoring) the interactions with the ambient R . One could then conclude that calling a system *open* or *closed* is a consequence of what states the observer is considering as ‘system’. Because the system may be open, but if more states from the environment are included in the system then eventually it can become a closed system, and the reverse is also true.

The last paragraph was a concluding remark on these terminologies. The more application oriented reader may now be more at ease by knowing that, in what follows (with the exception of Chapter 4), this text will be more problem oriented, and no more definitions and theorems will be given.

2.4 Types of Quantum Noise

In this section we will give some examples on what are some common types of noise in Quantum Information Processing. Much has been said in the beginning of this

chapter about decoherence, about the observed effect that some initially prepared pure states become mixed states over time. We will try to give a quick overview on some of these processes, in a purely informational fashion (as a more experimental one is given throughout the rest of this work).

A common type of noise in a quantum system is called the *bit-flip*. Suppose one has a pure state in a two level system, $\rho = |0\rangle\langle 0|$, a bit-flip is an operation that inverts the state to its orthogonal state, i.e., $\mathcal{E}(|0\rangle\langle 0|) = |1\rangle\langle 1|$. It is known that in a two level system, the Pauli matrices together with the identity operator, provide a basis for the space of operators ($SU(2)$) in this space. And one such operator has this exact property, the σ_x (also sometimes called the *NOT-gate* and denoted X).

$$\begin{aligned} X |0\rangle\langle 0| X^\dagger &= |1\rangle\langle 1|, \\ X |1\rangle\langle 1| X^\dagger &= |0\rangle\langle 0|. \end{aligned}$$

However, if one writes this as it stands, this would be the equation for a absolutely certain bit-flip. Whenever the bit-flip is produced probabilistically (as would be expected by a noisy process), the map should be one that rightly represents this. Which is the case with the following expression

$$\mathcal{E}_x(|\psi\rangle\langle\psi|) = p|\psi\rangle\langle\psi| + (1-p)X|\psi\rangle\langle\psi|X^\dagger. \quad (2.17)$$

So that it takes an arbitrary pure state $|\psi\rangle\langle\psi|$ and produces a state that has probability p of staying the same (by the identity operator), and $(1-p)$ of inverting basis.

As an example of the discussion the last section, we can see that a bit-flip is a partial tracing of the larger pure state

$$\sqrt{1-p}|\psi\rangle|0\rangle_R + \sqrt{p}X|\psi\rangle|1\rangle_R. \quad (2.18)$$

Let us check this explicitly

$$\begin{aligned} \text{Tr}_R\{(\sqrt{1-p}|\psi\rangle|0\rangle_R + \sqrt{p}X|\psi\rangle|1\rangle_R)(\sqrt{1-p}\langle\psi|\langle 0|_R + \sqrt{p}\langle\psi|X^\dagger\langle 1|_R)\} \\ = \sum_{i=0,1} \langle i|_R (\sqrt{1-p}|\psi\rangle|0\rangle_R + \sqrt{p}X|\psi\rangle|1\rangle_R)(\sqrt{1-p}\langle\psi|\langle 0|_R + \sqrt{p}\langle\psi|X^\dagger\langle 1|_R)|i\rangle_R \\ = \sum_{i=0,1} (\sqrt{1-p}|\psi\rangle\langle i|_R|0\rangle_R + \sqrt{p}X|\psi\rangle\langle i|_R|1\rangle_R)(\sqrt{1-p}\langle\psi|\langle 0|_R|i\rangle_R + \sqrt{p}\langle\psi|X^\dagger\langle 1|_R|i\rangle_R) \\ = \sum_{i=0,1} (\sqrt{1-p}|\psi\rangle\delta_{i0} + \sqrt{p}X|\psi\rangle\delta_{i1})(\sqrt{1-p}\langle\psi|\delta_{i0} + \sqrt{p}\langle\psi|X^\dagger\delta_{i1}) \\ = (1-p)|\psi\rangle\langle\psi| + pX|\psi\rangle\langle\psi|X^\dagger. \end{aligned}$$

Moreover, it is straightforward to check that the state is pure by calculating $\text{Tr}\{\rho^2\}$, which can be done using the following three facts: The cyclic property of the trace, $\text{Tr}\{ABC\} = \text{Tr}\{CAB\}$; that $XX^\dagger = \mathbb{I}$; and that the total trace is equal to the composed partial traces, as in $\text{Tr}_{AR}\{\rho\} = \text{Tr}_A\{\text{Tr}_R\{\rho\}\} = \text{Tr}_R\{\text{Tr}_A\{\rho\}\}$.

Note however, that the state $\mathcal{E}(|\psi\rangle\langle\psi|)$ itself (restricted to A) is not pure. As we can see by calculating

$$\begin{aligned}\text{Tr}\{\rho^2\} &= \text{Tr}\{(1-p)^2|\psi\rangle\langle\psi| + p(1-p)|\psi\rangle\langle\psi|X|\psi\rangle\langle\psi|X^\dagger \\ &\quad + p(1-p)X|\psi\rangle\langle\psi|X^\dagger|\psi\rangle\langle\psi| + p^2X|\psi\rangle\langle\psi|X^\dagger X|\psi\rangle\langle\psi|X^\dagger\} \\ &=((1-p)^2 + p^2)\text{Tr}\{|\psi\rangle\langle\psi|\} + 2p(1-p)|\langle\psi|X|\psi\rangle|^2 \\ &=(1-2p+2p^2) + 2p(1-p)|\langle\psi|X|\psi\rangle|^2.\end{aligned}$$

Clearly, this equation gives 1 whenever $p = 0$, or when $|\psi\rangle$ is an eigenket of X . So that the state remains pure whenever the probability of flipping is zero (the trivial case), or whenever the state has a certain symmetry (known to linear algebra students) that the operator does not change the direction of the state. This means that there are certain states that are, in a certain sense, immune to bit-flipping. Let us give a nice geometric view of this property.

Because the Pauli operators σ_i , together with the identity $\sigma_0 = \mathbb{I}$, form a basis to $SU(2)$, then, every qubit can be expressed as a linear combination of such operators. Imposing the restriction that the density operator must have unit trace, one can show that there is a general expression to a single qubit known as its *Bloch representation*

$$\rho = \frac{\mathbb{I}}{2} + \frac{\vec{v}_B \cdot \vec{\sigma}}{2}, \tag{2.19}$$

where, \vec{v}_B is known as the *Bloch vector* and its elements are given by $v_B^i = \text{Tr}\{\rho\sigma_i\}$. There is a straightforward generalization of this expression for N qubits ⁶ where one takes the tensor product $\sigma_i^j = \sigma_0^0 \otimes \dots \otimes \sigma_i^j \otimes \dots \otimes \sigma_0^N$, as in [15, p.390], the formula can be checked simply by taking two states ρ_A, ρ_B in the Bloch representation and then taking their product $\rho_A \otimes \rho_B$.

This representation has a nice visualization, because the identity is a fixed point (i.e., ρ is in an affine space around $\mathbb{I}/2$ of $SU(2)$), then only the other three operators change by changing the Bloch vector. This means that one can represent ρ in a 3-dimensional manifold. In this case, it is a sphere where the projection of the vector on the axis i is exactly $P_i(\rho) = \text{Tr}\{\rho\sigma_i\}$, see Figure 8.

⁶ an interesting discussion on this can be found on Lidar And Brun book “Quantum Error Correction”, and in the following forum discussion <https://physics.stackexchange.com/questions/424667/characterisation-of-the-generalised-bloch-space-in-spherical-coordinates?rq=1>

By taking a look at the purity expression above, and how it continuously changes depending on the overlap $|\langle \psi | x_{\pm} \rangle|$, where $|x_{\pm}\rangle$ are the eigenkets of X , then the state prior and after the bit-flip are represented in the Bloch Sphere as in Figure 2

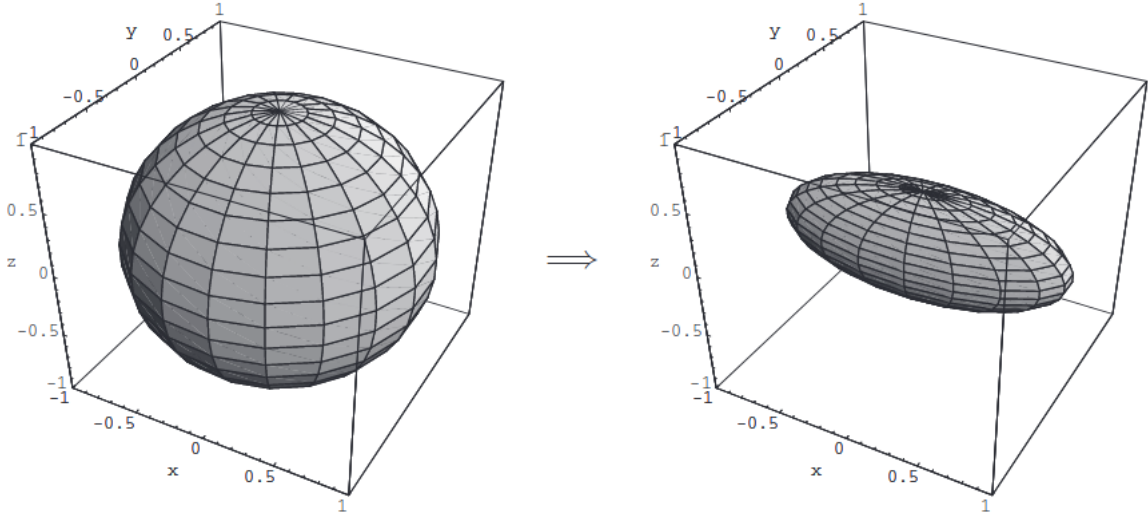


Figure 2 – The effect of the bit flip channel on the Bloch sphere, for $p = 0.3$. The sphere on the left represents the set of all pure states, and the deformed sphere on the right represents the states after going through the channel. Note that the states on the \hat{x} axis are left alone, while the $y - z$ plane is uniformly contracted by a factor of $1 - 2p$. Figure taken from [15], p.376]

It is quite straightforward to show that a pure single qubit state is pure whenever $\|\vec{v}_B\|_2 = 1$, so the interpretation of the deformation of the Bloch Sphere to an ellipsoid is that the state loses purity, which was expected by the discussion above.

Now that some of the effects of the bit-flip have been discussed, it is a natural thought to ask if there are Quantum Channels analogous to this one by simply substituting X by Y or Z . The answer to this question is a resounding yes, let us give some more details on that topic.

When the same channel is substituted by an Z gate, it receives the name of a *phase-flip*. This nomenclature is taken from the fact that the operations of Z on its basis is of adding a negative sign whenever the state has a $|1\rangle$ component. A negative sign can always be represented by Euler's formula $e^{-i\theta} = \cos \theta + i \sin \theta$, with $\theta = \pi$, and so one has

$$\begin{aligned}
 Z |\psi\rangle &= Z(\alpha_0 |0\rangle + \alpha_1 |1\rangle) \\
 &= \alpha_0 Z |0\rangle + \alpha_1 Z |1\rangle \\
 &= \alpha_0 |0\rangle - \alpha_1 |1\rangle \\
 &= \alpha_0 |0\rangle + e^{-i\pi} \alpha_1 |1\rangle \\
 &\neq |\psi\rangle,
 \end{aligned}$$

So the resulting state is not the same as the starting one, being different by the addition of a relative phase $e^{-i\pi}$ to the $|1\rangle$. When this happens with probability p_z the channel is given by

$$\mathcal{E}_z(\rho) = (1 - p)\rho + pZ\rho Z^\dagger. \quad (2.20)$$

Where we have written ρ as the state in both Equations (2.17) and (2.20) do not need to be pure states.

The effect of this channel on the Bloch Sphere representation is the same as in Figure 2, but aligned with the eigenkets of Z , shown now in Figure 3

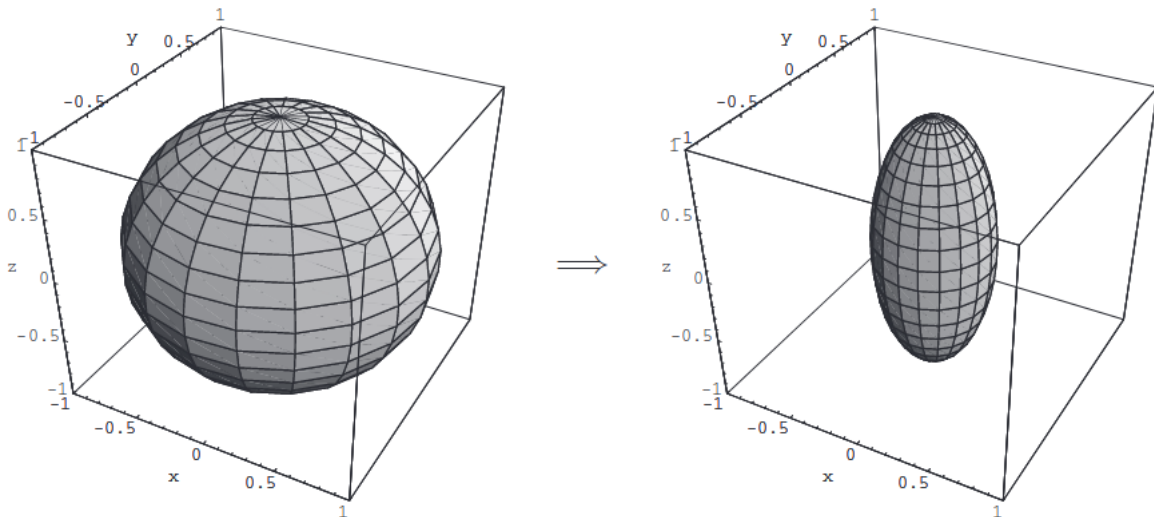


Figure 3 – The effect of the phase flip channel on the Bloch sphere, for $p = 0.3$. Note that the states on the z axis are left alone, while the $x - y$ plane is uniformly contracted by a factor of $1 - 2p$. Figure taken from [15, p.377]

The next noise channel is the one corresponding to Y . It follows the same reasoning, but with the eigenkets of Y , and to avoid redundancy is not shown here. However, for the sake of consistency, it suffices to say that it is named after the compound name of *bit-phase-flip*.

All three of these noise channels together have a special name, as they are all represented by Pauli operators, they receive the name of *Pauli Noise*. Of course the pauli noise is not restricted to occur in only one of these directions and can be a composition of all three noises as $\mathcal{E}_x(\mathcal{E}_y(\mathcal{E}_z(\rho)))$. Moreover, there is no special preference for the directions of X, Y, Z , and one could choose an arbitrary direction on the Bloch Sphere by taking the operators $\vec{n} \cdot \vec{\sigma}$.

An interesting property of the Pauli Noises, is that, if we write the state in the Bloch representation, the Identity and the direction of the noise are unchanged. Let us

show this for the bit-flip channel, but it can easily be generalized for any directional channel (i.e., Y, Z or any other combination).

$$\begin{aligned}
\mathcal{E}(\rho) &= \mathcal{E}\left(\frac{\mathbb{I}}{2} + \frac{\vec{v}_B \cdot \vec{\sigma}}{2}\right) \\
&= (1-p)\left(\frac{\mathbb{I}}{2} + \frac{\vec{v}_B \cdot \vec{\sigma}}{2}\right) + pX\left(\frac{\mathbb{I}}{2} + \frac{\vec{v}_B \cdot \vec{\sigma}}{2}\right)X^\dagger \\
&= (1-p)\left(\frac{\mathbb{I}}{2} + \frac{\vec{v}_B \cdot \vec{\sigma}}{2}\right) + p\left(\frac{X\mathbb{I}X^\dagger}{2} + \frac{\vec{v}_B \cdot X\vec{\sigma}X^\dagger}{2}\right) \\
&= (1-p)\left(\frac{\mathbb{I}}{2} + \frac{\vec{v}_B \cdot \vec{\sigma}}{2}\right) + p\left(\frac{\mathbb{I}}{2} + \frac{\vec{v}_B \cdot X\vec{\sigma}X^\dagger}{2}\right) \\
&= \frac{\mathbb{I}}{2} + \frac{\vec{v}_B}{2} \cdot \left((1-p)\vec{\sigma} + pX\vec{\sigma}X^\dagger\right) \\
&= \frac{\mathbb{I}}{2} + \frac{1}{2}v_B^{(1)}\sigma_1 + \left(\frac{1}{2} - p\right)\sum_{i=2}^3 v_B^{(i)}\sigma_i \\
&= \rho'.
\end{aligned}$$

So that,

$$\rho - \rho' = \left(\frac{1}{2} - p\right)\sum_{i=2}^3 v_B^{(i)}\sigma_i. \quad (2.21)$$

Where we have used the fact that $XXX^\dagger = X$ and that $XYX^\dagger = -Y$, $XZX^\dagger = -Z$, and the directions in the Bloch Sphere that are orthogonal to the flip gate have been deformed by $(1/2 - p)$. The identity, however, remains unchanged, as is still on the origin of the Bloch Sphere. For this symmetry the channel receives the name *flip*.

One can show that any such channel takes the Bloch vector to another as in

$$\vec{v}_B \rightarrow \vec{w}_B = M\vec{v}_B + c, \quad (2.22)$$

where the matrix M and the vector c are functions of the Kraus Operators, as in Theorem (2.12). In other words, the Bloch vector suffers a affine map, and the identity is unaffected. The exact expression for M and c can be found in [7, p. 338].

A last type of Quantum Noise is the *Amplitude Damping* channel. This channel has a special interpretation, as it is used to represent the *leakage of energy* in the system, e.g. a model of spontaneous emission, where there is the possibility that an excited atom (qubit) decays and the photon (also a qubit, and still undetected) leaves the system, changing it in an undetermined way. As the probability of a (having already occurred) decay increases, we expect the systems probability to be out of the excited state to grow, making it increasingly improbable to still be excited. Such a channel is described by the following Kraus operators

$$\mathcal{E}_A(\rho) = K_0 \rho K_0^\dagger + K_1 \rho K_1^\dagger = \rho', \quad (2.23)$$

where

$$K_0 = \begin{pmatrix} 1 & 0 \\ 0 & \sqrt{1-\gamma} \end{pmatrix}, \quad K_1 = \begin{pmatrix} 0 & \sqrt{\gamma} \\ 0 & 0 \end{pmatrix}. \quad (2.24)$$

When $\gamma = 0$, we regain the identity, but when it is not, the resulting state is

$$\rho' = \begin{pmatrix} \rho_{00} + \gamma \rho_{11} & \sqrt{1-\gamma} \rho_{01} \\ \sqrt{1-\gamma} \rho_{10} & (1-\gamma) \rho_{11} \end{pmatrix}. \quad (2.25)$$

One can show [7, p. 347] that the Bloch vector of this state is transformed as

$$\vec{v}_B = (v_x, v_y, v_z) \rightarrow \vec{w}_B = (\sqrt{1-\gamma} v_x, \sqrt{1-\gamma} v_y, \gamma + (1-\gamma) v_z).$$

Taking the case where $\gamma \rightarrow 1$, the state converges to $(0, 0, 1)$, i.e., $|0\rangle$ the ground state. If γ is seen as the probability of a decay occurring given a certain time, then this limit is the concatenation of the same amplitude damping channel over and over again. If this is done, then the probability of finding the qubit in the excited state at the n_{th} time step is given by

$$\rho^{(n)} = (1-p)^n \rho^{(0)} = e^{n \ln 1-p} \rho^{(0)}.$$

This means that the probability of finding the atom in the excited state drops exponentially. The resulting state in the Bloch sphere is then given by the Figure 4.

Of course there is nothing special about a decaying channel, we could make a model of an exciting channel (in the sense of excitation of the system), where the Kraus operators are modified to be

$$K_2 = \begin{pmatrix} \sqrt{1-\gamma} & 0 \\ 0 & 1 \end{pmatrix}, \quad K_3 = \begin{pmatrix} 0 & 0 \\ \sqrt{\gamma} & 0 \end{pmatrix}. \quad (2.26)$$

And by defining a probability of each one occurring, as $E_0 = \sqrt{p} K_0, E_1 = \sqrt{p} K_1, E_2 = \sqrt{1-p} K_2, E_3 = \sqrt{1-p} K_3$, we can then define the channel called *Generalized amplitude damping*, given by

$$\mathcal{E}_{GAD}(\rho) = \sum_{l=0}^3 E_l \rho E_l^\dagger, \quad (2.27)$$

where the stationary state is not the ground state anymore, but the state

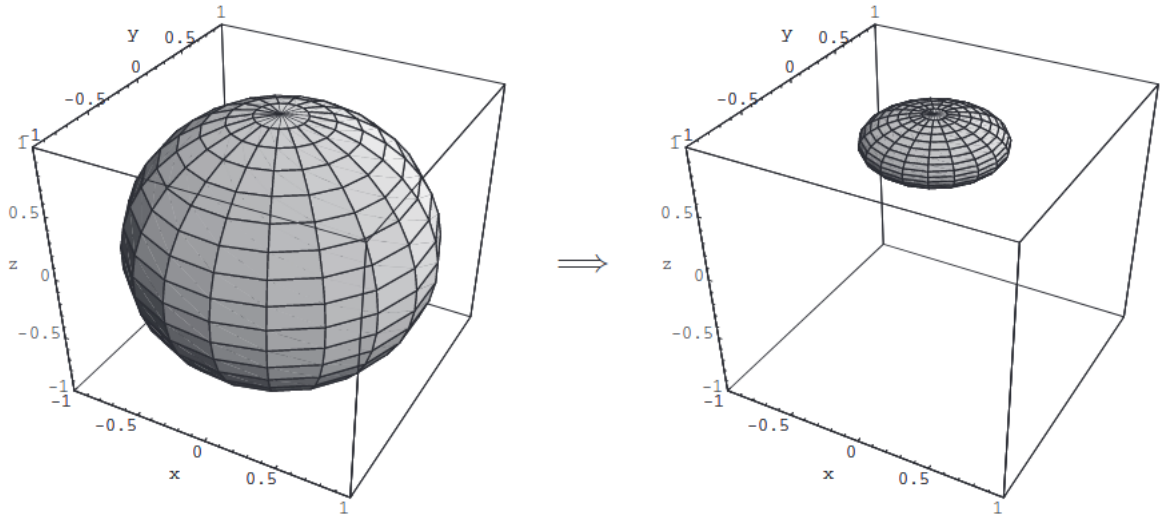


Figure 4 – The effect of the amplitude damping channel on the Bloch sphere, for $p = 0.8$. Note how the entire sphere shrinks towards the north pole, the $|0\rangle$ state. Figure taken from [15], p.383]

$$\rho_\infty = \begin{pmatrix} p & 0 \\ 0 & 1-p \end{pmatrix}. \quad (2.28)$$

This state ρ_∞ is a very special one in Physics, as when $p = e^{-E/k_b T}/\mathcal{Z}$, it is called the *Boltzmann state*, or *thermal state*, and is the usual state whenever a system relaxes when in contact with a thermal reservoir. Moreover, as in the case of Amplitude damping, there is an exponential path to the stationary state, and the time it takes for the damping to be such that $1/e$ of the sample is in the stationary state, is the T_1 time discussed in the introduction and given for the NMR case in Table 1.

One may have noted that differently from the Pauli Noises, the center of the possible states (i.e., the identity when $\vec{v}_B = \vec{0}$) is displaced from the origin. This is a defining feature that characterizes the amplitude damping as a somewhat different noise source than the Pauli Noises. So this also means that taking the three parameters from the Pauli Noise (p_x, p_y, p_z) with the two parameters for the generalized amplitude damping (p, γ), which we shall refer as (p, q) later on, we have a parametrization that gives us all of possible subspheres located inside a pure state Bloch sphere. We will study this in more details and show it experimentally in later chapters.

2.5 Quantum Process Tomography

Now that a formal description of quantum noise was shown, we may naturally ask how one retrieves a process given that what is measured in the laboratory are the eigenvalues (probabilities) associated to an observable and not the channel operators.

As noted in the section about Quantum Channels, it is an input to output approach to an observed system. So that the process description is not associated with what happens in times in between. Of course an infinitesimal approach can be made, but for the remaining of this work, whenever multiple of such steps are taken, it will be in a finite sectioning of the time interval.

To find out what are the operators in our channel, i.e., what is the actually dynamics of the system, we need to measure states before and after the channel. Because the space of operators of a d dimensional system has d^2 dimensions, we need to prepare a set of projectors that measures such basis, $\{|\psi_1\rangle\langle\psi_1|, \dots, |\psi_{d^2}\rangle\langle\psi_{d^2}|\}$, and then reconstruct the channel by observing the values of $\text{Tr}\{\rho|\psi_i\rangle\langle\psi_i|\}$, and $\text{Tr}\{\mathcal{E}(\rho)|\psi_i\rangle\langle\psi_i|\}$, for $i \in \{1, \dots, d^2\}$. This is already enough to characterize the channel, and is what is called the *Quantum Process Tomography* (QPT) of a system.

Although the description above is correct, in general terms, there are important details that have to be discussed in order to better understand the technique of QPT. First, that the choice of basis is arbitrary for the QPT, by the following theorem in [15, p.372]

Theorem 2.5.1 (Unitary freedom in the operator sum representation). *Suppose $\{E_1, \dots, E_m\}$ and $\{F_1, \dots, F_n\}$ are two operator sets that produce the channels \mathcal{E} and \mathcal{F} , respectively. By appending zeros to the shortest list, so that $m = n$, then $\mathcal{E} = \mathcal{F}$ if and only if there exists an unitary matrix u_{ij} such that $E_i = \sum_j u_{ij}F_j$.*

This means that, fixed a operator basis $\{\Gamma_m\}$, we can represent a quantum channel with the following general expression, called *chi-matrix representation*,

$$\mathcal{E}(\rho) = \sum_{m,n}^{d^2} \chi_{mn} \Gamma_m \rho \Gamma_n^\dagger, \quad (2.29)$$

where $\chi_{mn} \equiv \sum_i e_{im} e_{in}$ are the elements of the *chi matrix*, χ , and e_{im} are complex numbers. By definition χ is positive and hermitian⁷, and so, in terms of real parameters, one needs to determine $d^4 - d^2$ real numbers. And once χ is known, the dynamic map $\mathcal{E}(.)$ is entirely determined.

So now, the task is to measure the ρ before and after the map is applied. Because \mathcal{E} is linear, one can reconstruct it by proper inversion, by a linear system. By the theorem above and the choi matrix representation, even by choosing an operator basis such as

⁷ Truth be said, this is not always the case, according to our definition of Quantum Channels, we have demanded that $\sum K_l^\dagger K_l = \mathbb{I}$, but in a more general sense, it is possible that $\sum K_l^\dagger K_l \leq \mathbb{I}$, and then d^4 elements have to be determined [36]. However, in this case, the channels are not trace preserving. Although this leads to many interesting additions to the discussion, we will retain ourselves to the trace-preserving case.

$\{\rho_k|\rho_k = |m\rangle\langle n|\}_{k=1}^{d^2}$, where $\{|m\rangle\}_{m=1}^d$ is an orthonormal basis of the system, the measured outcomes can be traced back to the choi-matrix. Let us write it in terms of ρ_k .

Because $\{\rho_k\}$ is a basis of operator space, we can always write

$$\mathcal{E}(\rho_l) = \sum_{k=1}^{d^2} \lambda_{lk} \rho_k, \quad (2.30)$$

where the coefficients are determined by measurements

$$\lambda_{lk} = \text{Tr}\{\rho_k \mathcal{E}(\rho_l)\}. \quad (2.31)$$

Because any of the operators in the desired choi-basis can be determined by acting on the $\{\rho_k\}$ basis, we also have

$$\Gamma_m \rho_l \Gamma_n^\dagger = \sum_k^{d^2} \beta_{lk}^{mn} \rho_k, \quad (2.32)$$

so that the elements β_{lk}^{mn} are found by taking the dot product with a basis element $\rho_{l'}$ on both sides.

Then quantum channel action on a element of the basis $\{\rho_k\}$ written in the same basis, is given by

$$\mathcal{E}(\rho_l) = \sum_{mn}^{d^2} \sum_k^{d^2} \chi_{mn} \beta_{lk}^{mn} \rho_k. \quad (2.33)$$

Equating (2.30) and (2.33), and taking advantage of orthogonality, we have

$$\sum_{mn}^{d^2} \chi_{mn} \beta_{lk}^{mn} = \lambda_{lk}. \quad (2.34)$$

Because the sum is only on m, n this same equation can be rearranged in a linear system where χ and λ are flattened to d^4 vectors and β is a $d^4 \times d^4$ matrix. Resulting in

$$\mathbf{B}\vec{\chi} = \vec{\lambda}. \quad (2.35)$$

In this equation, $\mathbf{B}\vec{\chi}$ is entirely determined by the choice of basis $\{\rho_k\}$ and operators $\{\Gamma_m\}$, while $\vec{\lambda}$ is entirely determined by measurements in the system [37].

2.5.1 QPT in Action

In this last subsection we will give a step by step application of a QPT. There are multiple ways of conducting QPT experimentally. Suppose one has a system of interest

ρ , and a map applied to this system $\mathcal{E}(\rho)$ which we wish to characterize. One such way of doing QPT on the set $\{\rho, \mathcal{E}(\rho)\}$, is the *joint separable measurements ancilla-assisted process tomography* [37], that utilizes the *Choi-Jamiolkowski isomorphism*, which states that all Quantum Channels can be represented as quantum states of the form

$$\rho_{\mathcal{E}} \equiv (\mathcal{E} \otimes \mathbb{I})(|\Phi^+\rangle\langle\Phi^+|), \quad (2.36)$$

and then the channel is given by tracing out the ancilla

$$\mathcal{E}(\rho) = \text{Tr}_B\{(\mathbb{I}_A \otimes \rho^T)\rho_{\mathcal{E}}\}, \quad (2.37)$$

where $|\Phi^+\rangle = \frac{1}{\sqrt{d}} \sum_{i=1}^d |i\rangle_A \otimes |i\rangle_B$ is the Bell basis entangling the system with an ancilla of the same size, and ρ^T denotes the transposed density matrix of the desired input system [53, p.2]. Then, by considering the channel as a quantum state, the problem of QPT is reduced to the problem of a State Tomography (on a larger state).

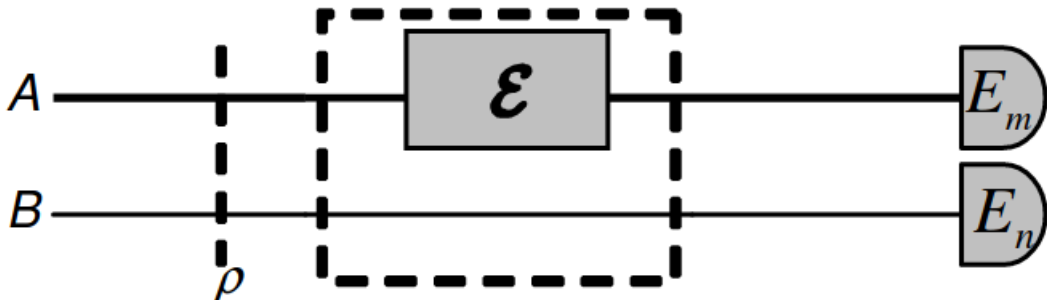


Figure 5 – Schematic diagram of separable Ancilla-assisted QPT. An ensemble of systems is prepared in the same quantum state ρ . Next, they are subjected to the map $\mathcal{E} \otimes \mathbb{I}$. Finally the operators $\{E_j\}$ are measured on both the system and the ancilla, which results in the required joint probability distributions or expectation values [37].

This method has the advantage of being simpler to implement computationally, and cleaner analytically, as by choosing the Kraus operators as $\{\Gamma_m\} = \{|i\rangle\langle j|\}$ results in $\frac{1}{d}\chi = \rho_{\mathcal{E}}$ [37, p.3]. For this reason, many of the papers in QPT actually use this method, and computational solutions have shown promising results. It has been shown by [53] that a machine learning algorithm can reconstruct the dynamics of a noisy system of up to 10 qubits and depth of 5 arbitrary gates, reaching 0.99 fidelity, using only a small fraction (about 10^5) of the total preparation and measurements taken (which would be, given $d = 2^N$, equal to $2^{40} - 2^{20}$ in an informationally complete setting).

This method however relies on the assumption that maximally entangled states⁸ are easily available experimentally. Which may not be the case, specially in a NMR quantum

⁸ for a table with many different methods of QPT and their computational/measurement complexity, see [37]

device. For this reason we will follow a different method, called *mutually unbiased bases measurement*. As this method can avoid highly entangled states, but requires tomographies before and after the quantum process.

Definition 2.5.2 (Mutually unbiased basis). *Given two different basis sets $\{|a_i\rangle\}_{i=1}^d$ and $\{|b_i\rangle\}_{i=1}^d$ for a d -dimensional Hilbert space \mathcal{H} . If*

$$|\langle a_i | b_j \rangle|^2 = \frac{1}{d}, \quad \forall i, j, \quad (2.38)$$

then they are called a Mutually Unbiased Basis (MUB).

Naturally, the eigenkets of $X, Y, Z : \{|0\rangle, |1\rangle\}, \{|x_{\pm}\rangle\}, \{|y_{\pm}\rangle\}$, provide pairwise MUBs.

One can show that, for a d -dimensional system, there exists at most $d + 1$ MUBs, and if d is the power of a prime, the number of MUBs is exactly $d + 1$ [37, p.5]. MUBs are particularly useful, as they provide optimal information, as the measuring of a channel via MUBs requires the minimal number of noncommuting observables.

Recall that a density matrix has $d^2 - 1$ independent real parameters to be determined. Measuring one observable with non-degenerate spectrum $\Omega = \sum_i \omega_i \Pi_i$, gives $d - 1$ independent data points, each given by the probability $\text{Tr}\{\rho \Pi_i\} = p(\omega_i)$. This means that at least $d^2 - 1/(d - 1) = d + 1$ measures outcomes of eigenvalues from noncommuting observables are needed to fully determine ρ . One may remember the one qubit example which needs 3 measurements, this is a direct consequence from the Bloch representation, as \vec{v}_B has three components for $d = 2$ (a qubit).

For the QPT problem, we are interested in reconstructing the process matrix χ rather than the density operator. So the same reasoning above applies, but this time for the $d^4 - d^2$ elements of the Choi matrix. So that we need $d^2(d^2 - 1)/(d - 1) = d^2(d + 1)$ noncommuting observables eigenvalue outcomes. For a single qubit this is equal to 12. Focusing on the single qubit case: given 4 states of a MUB, and given that, for each one of these states, 3 observables are tomographed, we can reconstruct the $12 = 4 \cdot 3$ independent elements of χ . One such choice is $\{|0\rangle, |1\rangle\}$ and $\{|x_{\pm}\rangle\}$, and the states

$$\mathcal{E}(|0\rangle\langle 0|), \quad \mathcal{E}(|1\rangle\langle 1|), \quad \mathcal{E}(|x_+\rangle\langle x_+|), \quad \mathcal{E}(|x_-\rangle\langle x_-|)$$

are tomographed, i.e., we measure for each one of the $\text{Tr}\{\mathcal{E}(\rho)X\}, \text{Tr}\{\mathcal{E}(\rho)Z\}, \text{Tr}\{\mathcal{E}(\rho)Y\}$. Once this is done, we can use the linear system in Equation (2.35) to solve for χ .

Two last commentaries are needed here. First, there is no restriction to which states are chosen except the fact that they are in the union of the MUB sets. In the tests ran in Chapter 7.4, we have chosen for the single qubit QPT the states $\{|0\rangle, |1\rangle, |x_-\rangle, |y_-\rangle\}$. So

that the first two elements are form an orthogonal basis, but last two do not, they are each from a different MUB, i.e., $|\langle x_+|y_- \rangle|^2 = 1/d$. This is not a problem, as this set is still maximally informative. The main reason for this choice of tomography states is that: In what follows, we will fix the operator basis as $\{i\mathbb{I}, X, Y, Z\}$, so that the matrix in the linear system in Equation (2.35) has the special property that any unital process (i.e. $\mathcal{E}(\mathbb{I}) = \mathbb{I}$), has a χ matrix that with only real components [43, p.7]. Which allows us to use all usual tools of linear algebra in \mathbb{R}^n , and solve the linear system by off the shelf methods. Then, the choice of using $|y_- \rangle$ instead of $|x_- \rangle$, is that, given that we have measured the other three states, the Y eigenket gives us a special information on the phase of the system, and therefore has interesting properties of its own.

In the following we will run a step by step example of QPT.

2.5.1.1 QPT Example

Suppose we have a channel composed of two channels \mathcal{E}_U , a rotation of $\pi/2$ around the y axis $U = \text{Rot}_y(\pi/2) = e^{-i\frac{\pi}{4}\sigma_y}$ and \mathcal{E}_{p_y} , a Pauli bit-phase-flip. Composing both channels to obtain a noisy rotation gate, one gets

$$\begin{aligned}\mathcal{E}(\rho) &= \mathcal{E}_{p_y}(\mathcal{E}_U(\rho)) \\ &= \mathcal{E}_{p_y}(U\rho U^\dagger) \\ &= (1 - p_y)U\rho U^\dagger + (p_y)YU\rho U^\dagger Y^\dagger.\end{aligned}$$

Suppose $p_y = 0.1$, i.e., a 10% chance of flipping.

Given the input states $\{|0\rangle\langle 0|, |1\rangle\langle 1|, |x_+\rangle\langle x_+|, |y_-\rangle\langle y_-|\} = \{\rho^{(i)}\}_{i=1}^4$, the output states are

$$\begin{aligned}\mathcal{E}(\rho^{(1)}) &= \begin{pmatrix} 0.5 & 0.45 \\ 0.45 & 0.5 \end{pmatrix}, \\ \mathcal{E}(\rho^{(2)}) &= \begin{pmatrix} 0.5 & -0.45 \\ -0.45 & 0.5 \end{pmatrix}, \\ \mathcal{E}(\rho^{(3)}) &= \begin{pmatrix} 0.05 & 0 \\ 0 & 0.95 \end{pmatrix}, \\ \mathcal{E}(\rho^{(4)}) &= \begin{pmatrix} 0.5 & i0.5 \\ -i0.5 & 0.5 \end{pmatrix},\end{aligned}$$

as expected, $\rho^{(4)} = |y_-\rangle\langle y_-|$, by being an eigenket of both U and the bit-phase-flip, is unaffected by the channel. The vector $\vec{\lambda}$ in Equation (2.35) is then given by flattening these outputs:

$$\vec{\lambda} = \begin{bmatrix} 0.5 \\ 0.45 \\ 0.45 \\ 0.5 \\ 0.5 \\ -0.45 \\ -0.45 \\ 0.5 \\ 0.05 \\ 0 \\ 0 \\ 0.95 \\ 0.5 \\ 0.5i \\ -0.5i \\ 0.5 \end{bmatrix}$$

The 16x16 matrix \mathbf{B} for the chosen operator basis $\{i\mathbb{I}, X, Y, Z\}$ and basis for density matrix space $\{|n\rangle\langle m|\}$ is then $\mathbf{B} =$

$$\mathbf{B} = \frac{1}{2} \begin{pmatrix} 2 & 0 & 0 & 2i & 0 & 0 & 0 & 0 & 0 & 0 & 0 & 0 & -2i & 0 & 0 & 0 & 2 \\ 0 & 2i & 2 & 0 & 0 & 0 & 0 & 0 & 0 & 0 & 0 & 0 & 0 & 2 & -2i & 0 \\ 0 & 0 & 0 & 0 & -2i & 0 & 0 & 0 & 0 & 2 & 2 & 0 & 0 & 0 & 0 & 0 & 2i \\ 0 & 0 & 0 & 0 & 0 & 2 & 0 & 0 & -2i & 0 & 0 & 2i & 2 & 0 & 0 & 0 & 0 \\ 0 & 0 & 0 & 0 & 0 & 0 & 2 & 0 & 0 & 2i & 0 & -2i & 2 & 0 & 0 & 0 & 0 \\ 0 & 0 & 0 & 0 & -2i & 0 & 0 & 0 & 0 & -2 & -2 & 0 & 0 & 0 & 0 & 0 & 2i \\ 0 & 2i & -2 & 0 & 0 & 0 & 0 & 0 & 0 & 0 & 0 & 0 & -2 & 0 & -2i & 0 \\ 2 & 0 & 0 & -2i & 0 & 0 & 0 & 0 & 0 & 0 & 0 & 0 & 2i & 0 & 0 & 0 & 2 \\ 1 & i & -1 & i & -i & 1 & i & -i & -i & 1 & -1 & -i & -i & 1 & i & 1 & 1 \\ 1 & i & 1 & -i & -i & 1 & -i & -i & -i & -1 & -1 & i & -i & 1 & i & -1 & -1 \\ 1 & i & -1 & i & -i & 1 & i & i & i & 1 & 1 & i & i & i & -1 & i & -1 \\ 1 & i & 1 & -i & -i & 1 & -i & i & i & -1 & 1 & i & i & i & -1 & i & 1 \\ 1 & -i & -i & i & -i & 1 & i & -i & -1 & 1 & i & -i & -1 & 1 & -i & 1 & 1 \\ i & i & 1 & 1 & -i & -i & -1 & -1 & -1 & -1 & i & i & 1 & 1 & -1 & -1 & -i \\ -i & i & -1 & 1 & -i & i & -1 & 1 & 1 & -1 & -i & i & 1 & -1 & -1 & -1 & i \\ 1 & 1 & -1 & -i & 1 & 1 & -i & -i & i & i & 1 & 1 & i & i & 1 & 1 & 1 \end{pmatrix}$$

Then, one solves the linear system $\vec{\chi} = \mathbf{B}^{-1}\vec{\lambda}$. And obtains

$$\vec{\chi} = \begin{bmatrix} 0.5 \\ 0 \\ 0.45 \\ 0 \\ 0 \\ 0 \\ 0 \\ 0 \\ 0.45 \\ 0 \\ 0.5 \\ 0 \\ 0 \\ 0 \\ 0 \\ 0 \\ 0 \\ 0 \\ 0 \end{bmatrix}.$$

Rewriting this as a matrix for the process matrix χ we have

$$\begin{array}{ccccc} & i\mathbb{I} & X & Y & Z \\ i\mathbb{I} & \begin{pmatrix} 0.5 & 0 & 0.45 & 0 \end{pmatrix} \\ X & \begin{pmatrix} 0 & 0 & 0 & 0 \end{pmatrix} \\ Y & \begin{pmatrix} 0.45 & 0 & 0.5 & 0 \end{pmatrix} \\ Z & \begin{pmatrix} 0 & 0 & 0 & 0 \end{pmatrix} \end{array} = \chi.$$

This means that the quantum channel is written in this operator basis as

$$\mathcal{E}(\rho) = \frac{1}{2}(Y\rho Y^\dagger - \rho) + 0.45i(Y\rho\mathbb{I} + \mathbb{I}\rho Y^\dagger). \quad (2.39)$$

This example is to showcase that, even if we did not know the functional form of the channel, we can obtain it in the desired basis.

We will return to this topic only in the end of this dissertation, as not only experimental tests of QPT have been performed, but also an algorithm that finds the Pauli noises and amplitude damping by having the Choi matrix as input is also presented. We will be detecting the typical noise types in our NMR-based RF control system via this algorithm. But first, let us delve in a bit of Quantum Information in a NMR setting in the next Chapter.

Chapter 3

The NMR Setting

Nuclear Magnetic Resonance (NMR) is a technique primarily known for its applications in chemistry and biology to study the magnetic properties of atomic nuclei. However, in the realm of Quantum Information, NMR offers an interesting platform for the test of principles with spin qubits.

In this section we will briefly discuss the physical implementation of NMR Quantum Information in the laboratory and how one characterizes qubits in NMR. In subsection 3.1 we will discuss the effective hamiltonian in our system in a general way, which is discussed separately in three parts that, summed, compose the full hamiltonian: the Zeeman hamiltonian, the interaction hamiltonian, and the Radio Frequency (RF) (also called control) hamiltonian. In the following subsections 3.2 and 3.3, we will discuss how these hamiltonians change when in homonuclear systems and heteronuclear systems, respectively, and discuss the application and use-cases of a standard approximation called the rotating wave approximation. Finally in subsection 3.4 an example is given in the case of a mixed system, i.e., when the system has both homonuclear and heteronuclear subsystems. The reader that is interested in more details may refer to the books and thesis [6, 15, 29, 34, 40, 52].

To construct a qubit it is necessary to have a two level system in quantum mechanics. There are many possible implementations of such systems, such as neutral atoms, nitrogen vacancies in diamonds, photonics, superconducting qubits, trapped ions, and so on [27]. But in our case the two level system of choice is the spin of the nucleus of certain atoms. This configures as a natural choice, as systems with spin 1/2 are the standard example of two level systems in Quantum Mechanics [40]. Higher spins such as 3/2 can also be used, and are quite common to solid state NMR [6], these configure as “qudits”. We will however restrict the discussion to the liquid states case and spin 1/2.

To prepare a NMR sample it is necessary to choose a molecule that has atoms with an odd number of spins in their nucleus. See Figure 6 where the example of Chloroform is shown: in this case the two qubits are the hydrogen and a carbon 13 (as the carbon 12 has

an even set of spins). More examples are shown in Figure 7. A sample is prepared where the molecule is diluted, the solution has to have a neutral spin (even number) so that it becomes insensitive to the magnetic field in the NMR, usually one may use deuterium or certain types of acetone, depending on the solubility of the desired molecule [6].

Once the sample is prepared we have on our hands Avogadro numbers of qubits, but because the two level energy splitting is too small to be measured we are in need of a machine that can enhance it to the resolution of current electronic devices. This is where the major part of the spectrometer comes in hand: the sample is placed in the center of a superconducting solenoid capable of generating a strong magnetic field in the \hat{z} direction (between 11 and 12 Teslas). It is known, in a undergraduate Physics level, that such a field produces the Zeeman effect, and when this field is sufficiently strong (i.e., above the Paschen-Back limit) one can effectively ignore the spin-orbit coupling and produce a time independent hamiltonian as in Equation (3.5), called the Zeeman hamiltonian, see Sakurai's book [47]. This effect is known to enlarge the two-level system energy splitting. And the Larmor frequency (as will be discussed latter).

Because the superconductors display their characteristic property only in low temperatures, the solenoid must be placed in a liquid helium refrigeration, which by itself has its temperature controled by a liquid nitrogen bath. The sample, however, is not refrigerated, as the drawing in Figure 6 may induce the reader to think. In fact, the sample usually has a slightly higher temperature than the ambient, controlled by a thermostat, this procedure is made to secure the temperature stability of the sample while the Quantum Information Processing occurs. In fact, the field is so strong that the state (when in thermal equilibrium) can be described as [6, p.104]

$$\rho_{\text{eq}} = \frac{1}{Z} \exp\left(\frac{-1}{k_B T} \mathcal{H}\right) \approx \frac{1}{Z} \mathbb{I} + \frac{\beta}{Z} \mathcal{H}, \quad (3.1)$$

This occurs, because, in a 10 T field, the magnetic energy will be $E \approx 3.15 \times 10^{-7}$ eV, while the thermal energy will be $k_B T \approx 2.5 \times 10^{-2}$, so that the fraction $E/k_B T \approx 10^{-5}$, which justifies the expansion of the exponential [48]. So that typical stationary states in NMR are actually what are called the *shift states*

$$\Delta\rho_{\text{shift}} = \frac{10^{-5}}{Z} \mathcal{H}, \quad (3.2)$$

and therefore have a property of mirroring the hamiltonian. When multiple qubits are present, a interaction hamiltonian is also present, as will be discussed in the next section. This hamiltonian is however less intense, and the state above still provides a good approximation.

Once the system is in equilibrium, an radio-frequency (RF) coil around the sample

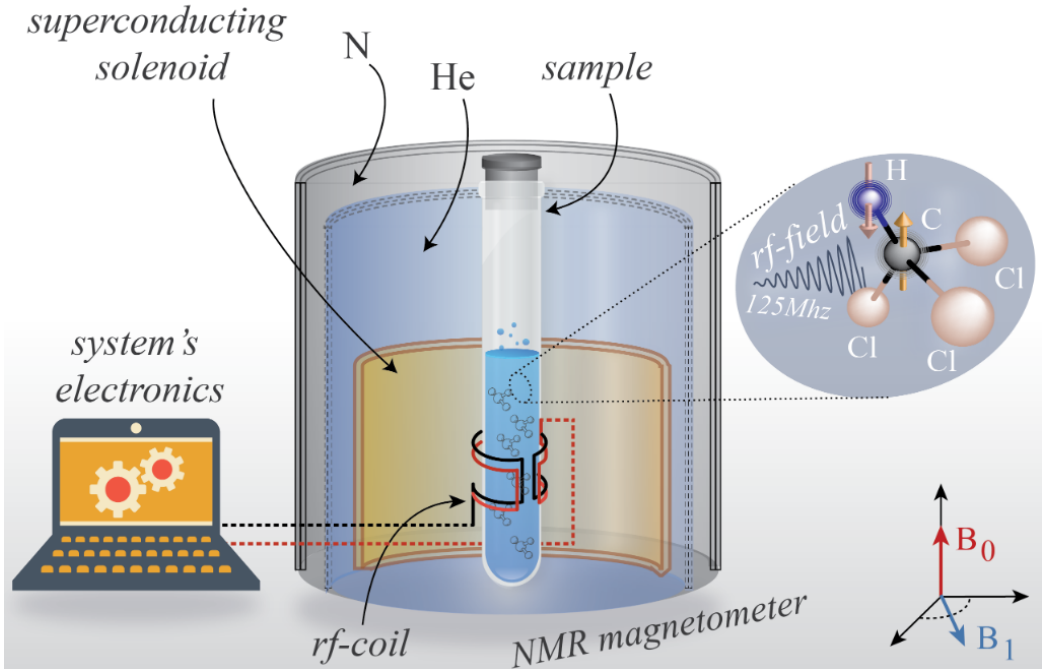


Figure 6 – Picture taken from [6] shows a pictorial representation of the NMR spectrometer. The sample is sealed in a test tube, and is positioned in the center of a superconducting solenoid (refrigerated by liquid helium), where a stron \vec{B}_0 magnetic field in the \hat{z} direction is produced by the currents in the solenoid. A weaker radiofrequency field \vec{B}_1 in the XY plane (to produce perturbations) is applied via a coil wrapped around the tube, also called the control field. A Chloroform molecule (2 qubit system) is shown in details on the right. The system is controlled externally by an electronics casing and application specific software.

is capable of producing weaker fields that provide control to the qubits, this field acts only in the \hat{x} and \hat{y} direction and is depicted as B_1 in Figure 6. One should note that because the field is weaker, its effect on the spins is calculated mostly in a perturbative way, as there are multiple effects due to neighboring electrons to the nuclei and the sample solution that provide non-trivial electronic shielding to the nuclei. However, an effective field is felt by the spins, given sufficient power, and is capable of producing rotations on the qubit state. To measure this state an antenna is positioned near the sample, and when the state relaxes from its rotated state to the equilibrium, it produces an alternated current in this antenna, whose characteristic frequency determines the state prior to relaxation.

As one may have noted, because a great number of nuclei/qubits are present in the sample, what is actually measured in NMR is not the individual states, but rather a spatial and temporal average of the whole sample. This means that with a single measurement one can find the average of two non-commuting operators such as σ_x and σ_y . This is a well known perk to NMR [40]. On the other hand, a drawback of NMR quantum devices is that, the states have a \mathcal{Z} factor dividing it, and so the strength of the felt signal by the antenna diminishes with the number of qubits. This gives a practical limit to Quantum

Computation in NMR to 12 qubits [6], the technique has a scalability upper bound that is hardly surpassable.

A hamiltonian treatment of the state evolution will now be given, however, some definitions must be given now. Above we gave the example of the chloroform molecule, however, many other molecules are available for NMR Quantum devices, as the only restriction is to have nuclei with spare spins. We will follow [29] and name two distinct classes : We call a system *homonuclear* when the qubits are encoded in the same isotope, and *heteronuclear* when the qubits are encoded in different isotopes, examples are given in Figure 7.

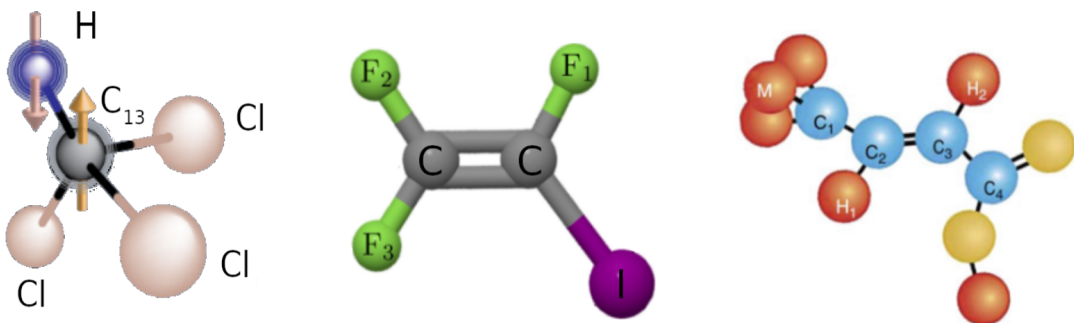


Figure 7 – From left to right: examples of heteronuclear (Chloroform, 2 qubits), homonuclear (Iodotrifluoroethylene C_2F_3I , a.k.a. Trifluorine – edited from [8] – , 3 qubits) molecules and mixed systems (trans-crotonic acid [46], up to 7 qubits encoded in C_1, C_2, C_3, C_4 and H_1, H_2, M , where all carbons are Carbon 13 and M is three different hydrogens that have a degenerate frequency and therefore act as a single qubit.), respectively.

3.1 Hamiltonians in NMR

We will discuss some properties of the hamiltonian of interest in liquid state NMR, without going through explicitly on how to obtain this functional, as our focus here is directed to pragmatic matters, i.e., qubit control. A more detailed text on how to obtain this hamiltonian from the physical system can be found in [6, 29, 34, 40]. The relevant terms of the hamiltonian of interest to describe our liquid state NMR sample of molecules encoding N (spin 1/2) qubits in the Schrödinger picture is given by

$$\mathcal{H}(t) = -\frac{\hbar}{2} \sum_{i=1}^N f_i \sigma_z^{(i)} + \frac{\hbar}{4} \sum_{i \neq k}^N J_{ik} \sigma_z^{(i)} \sigma_z^{(k)} + \frac{1}{2} \hbar \gamma \sum_{i=1}^N (1 + \delta_i) (B_x(t) \sigma_x^{(i)} + B_y(t) \sigma_y^{(i)}), \quad (3.3)$$

which can be written as

$$\mathcal{H}(t) = \mathcal{H}_{\text{Zeeman}} + \mathcal{H}_{\text{int}} + \mathcal{H}_{\text{RF}}(t), \quad (3.4)$$

where $\mathcal{H}_{\text{Zeeman}}$ is the Zeeman part, \mathcal{H}_{int} the interaction Hamiltonian, and $\mathcal{H}_{\text{RF}}(t)$ the RF external field perturbative hamiltonian. In the following we discuss each one of them separately.

It is important to accentuate that the expression $\mathcal{H}_{\text{int}} = \frac{\hbar}{4} \sum_{i \neq k}^N J_{ik} \sigma_z^{(i)} \sigma_z^{(k)}$ is not always a good approximation. As the interaction in molecules may have a very complex form in most cases, where the term J_{ik} , called *the scalar coupling* may be instead a tensor, exhibiting quadrupolar interaction (in the case of solid state NMR), Heisenberg couplings (i.e., terms like $\sigma_x^{(i)} \otimes \sigma_x^{(k)}$, $\sigma_y^{(i)} \otimes \sigma_y^{(k)}$, etc.), and more [34, p.217]. However, in heteronuclear samples and in some homonuclear samples (as is the case with the Trifluorine), an approximation called the *secular approximation*, that states that when the qubit resonance frequency $\{f_j\}$ differences are such that $|J| \ll |f_j - f_k|$, (in the heteronuclear case) or when $|\pi J| \ll |\gamma B_0(\delta_j - \delta_k)|$ (homonuclear case¹), then the expression for \mathcal{H}_{int} is the sole coupling. A detailed treatment of this approximation is found in [52, p.198].

3.1.1 Zeeman Hamiltonian ($\mathcal{H}_{\text{Zeeman}}$)

To exemplify the terms of the hamiltonian in Equation (3.4) consider a molecule with three nuclei of the same isotope (e.g., a molecule with three fluorine nuclei such as Iodotrifluoroethylene, which we shall refer as *Trifluorine*, see Figure 9), when a strong $\mathbf{B}_0 = B_0 \hat{z}$ field is applied, the Zeeman Hamiltonian for each nucleus in the molecule is given by $\mathcal{H}_{\text{Zeeman}}^{\text{nucleus}} = -\boldsymbol{\mu} \cdot \mathbf{B}_0 = -\mu_z B_0$, where $\boldsymbol{\mu}$ is the magnetic moment of each nucleus. When dealing with spin-1/2 systems, we can write $\mu_z = \gamma I_z = \gamma \hbar \sigma_z / 2$. Then, the Zeeman Hamiltonian will be

$$\mathcal{H}_{\text{Zeeman}} = -\frac{1}{2} \hbar \gamma_{F_1} B_0 \sigma_z^{(1)} - \frac{1}{2} \hbar \gamma_{F_2} B_0 \sigma_z^{(2)} - \frac{1}{2} \hbar \gamma_{F_3} B_0 \sigma_z^{(3)}. \quad (3.5)$$

Despite having $\gamma_{F_1} = \gamma_{F_2} = \gamma_{F_3} = \gamma$, as all three nuclei are of the same atomic number, the effect of the magnetic field on each one may differ due to the distinct electronic clouds surrounding each one of them. Moreover, if the molecule has an asymmetric geometry, the effective field will be slightly different on each one. This interaction causes a chemical shift so that $\gamma B_0 \rightarrow \gamma B_0(1 + \delta_i)$ [34, p.197]. Thus we have

$$\mathcal{H}_{\text{Zeeman}} = -\frac{1}{2} h f_1 \sigma_z^{(1)} - \frac{1}{2} h f_2 \sigma_z^{(2)} - \frac{1}{2} h f_3 \sigma_z^{(3)}, \quad (3.6)$$

where $f_i = B_0(1 + \delta_i)\gamma/2\pi$ is the *chemically shifted Larmor frequency* for the i 'th nucleus, and δ_i denotes the chemical shift. Note that the Larmor frequency is a linear frequency, distinct from the angular frequency $\omega_j = 2\pi f_j$.

For a molecule with N isotopes we have

¹ here δ_j are the chemical shifts, explained in Subsection 3.2

$$\mathcal{H}_{Zee}(t) = -\frac{\hbar}{2} \sum_{i=1}^N f_i \sigma_z^{(i)}. \quad (3.7)$$

3.1.2 RF Hamiltonian (\mathcal{H}_{RF})

Applying a second external field $\mathbf{B}_1(t) = B_x(t)\hat{x} + B_y(t)\hat{y}$. The RF Hamiltonian for a single nucleus would give us

$$\begin{aligned} \mathcal{H}_{RF}^{nucleus} &= \boldsymbol{\mu} \cdot \mathbf{B}_1(t) \\ &= \frac{1}{2}\hbar\gamma[B_x(t)\sigma_x + B_y(t)\sigma_y], \end{aligned} \quad (3.8)$$

where the components from the nuclear magnetic dipole moment are given by $\mu_m = \gamma I_m = \gamma\hbar\sigma_m/2$ is the m th-component, ($m \in \{x, y, z\}$), for the magnetic moment of the nucleus.

Remember that the state can be written in the Bloch Sphere notation as in Equation (3.1) restated here for clarity

$$\rho = \frac{\mathbb{I}}{2} + \frac{\vec{n} \cdot \vec{\sigma}}{2}.$$

Due to the \mathbf{B}_0 field, the spin of the nuclei are precessing in the z direction with the Larmor frequency.

In other words, in the referential of the laboratory the σ_x and σ_y components of our state ρ , have a time-dependence, so they are actually measured as $\sigma_x^{(k)} \cos(\omega_k t)$ and $\sigma_y^{(k)} \sin(\omega_k t)$, where $\omega_k = 2\pi f_k$ (the Larmor frequency). Such time-dependence is not present in the z direction since projection on σ_z is constant during the rotation². If left unperturbed by the RF Hamiltonian, this can be stated for each qubit as

$$\rho_k = \frac{\mathbb{I}}{2} + \frac{1}{2} \left(n_x \sigma_x \cos(\omega_k t) + n_y \sigma_y \sin(\omega_k t) + n_z \sigma_z \right). \quad (3.9)$$

This means that the transversal field $\mathbf{B}_1(t)$ has to oscillate in the same frequency to be resonant with the state. In homonuclear systems the resonance Larmor frequency of each qubit will differ by $\delta_i \approx 10$ kHz, while in heteronuclear systems this may be in the order of $|f_j - f_k| \approx 100$ MHz.

Moreover, in the homonuclear case, for N isotopes, the same reasoning in the previous section regarding the chemical shift on the B_0 field applies, and so the amplitude of the effective field shifts at each nucleus as $\gamma \mathbf{B}_1(t) \rightarrow \gamma(1 + \delta_i) \mathbf{B}_1(t)$, each with a time

² To be precise, there is an angle θ between the state vector $|\psi(t)\rangle$ and the z direction, and the decomposition of the state in the basis of $SU(2)$ actually has the cosines and sines of this angle multiplying the z, x, y directions. A thorough analysis shows, however, that such angle has no effect, and the field acts as if it were non-existent. For more details please refer to [34, p.177]

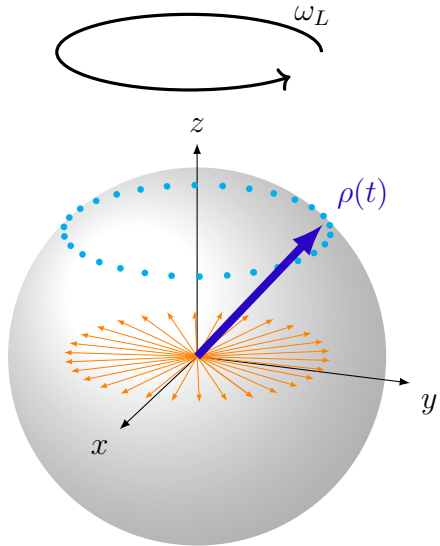


Figure 8 – Whenever in the laboratory frame of reference, the state, under the influence of a $\vec{B}_0 = B_0\hat{z}$ magnetic field, precesses around the \hat{z} direction with a Larmor Frequency ω_L , due to the Zeeman effect. The blue arrow from the origin represents the state in the Bloch sphere representation at time t , while cyan dots represent the state position in other time steps in this precessing stationary state, the projection of the cyan dots to the \hat{z} is constant in this time evolution. Orange arrows represent the projection of the cyan states onto the XY plane, a pictorial representation of the meaning of the sine and cosine terms in Equation (3.9).

dependence according to its Larmor frequency. This means that the felt amplitude will differ for each one of the qubits.

The effective RF Hamiltonian for N nuclei of a given isotope, would then be

$$\mathcal{H}_{RF} = \frac{1}{2}\hbar\gamma \sum_{k=1}^N (1 + \delta_k) (B_x(t)\sigma_x^{(k)} + B_y(t)\sigma_y^{(k)}). \quad (3.10)$$

To the cases studied in this thesis, the magnitude of δ_i due to the chemical shift is very small compared to the frequency of a stand-alone nucleus [34, p.202]. Experimentally it is expected that the frequency $f = B_0\gamma/2\pi$ is of the order of 100 MHz, while the shift given by the product $f\delta_i$ is of the order of 10 kHz (around .01% of f), and is, therefore, mostly negligible for some use cases of the NMR technique. However, its presence cannot be ignored when dealing with fine control of qubits, where coupling terms that depend on δ_i are essential for multi-qubit gates, especially in homonuclear systems.

Even though the chemical shift δ_i has to be taken into account for \mathcal{H}_{Zee} , the same is not true for the RF Hamiltonian. It should be noted that, while $f_i\delta_i$ is of the order of 10 kHz, the transversal field $\mathbf{B}_1(t)$ is about 10^{-4} times smaller than the constant field in the \hat{z} direction, B_0 . The product $\delta_i|\mathbf{B}_1|\gamma/2\pi \approx f_i\delta_i 10^{-4}$, which gives a frequency of around 1 Hz. Such slow frequencies are very near to the precision limit of our equipment, and,

even if interfering in the evolution of the system, may not be measurable in a significant fashion.

Neglecting the δ_k in the RF Hamiltonian, the resulting expression for N nuclei is then given by

$$\mathcal{H}_{RF} = \frac{1}{2}\hbar\gamma \sum_{k=1}^N (B_x(t)\sigma_x^{(k)} + B_y(t)\sigma_y^{(k)}) \quad (3.11)$$

where γ is the gyromagnetic factor of the target isotope.

3.2 Homonuclear Systems

For the sake of clarity, we will be working with a Hamiltonian such as the one for the Trifluorine molecule in this section (see Figure 9), i.e., reducing the case to one type of isotope (homonuclear) but having three of them, $N = 3$, as the generalization is quite straightforward for larger N . The heteronuclear case will be discussed later.

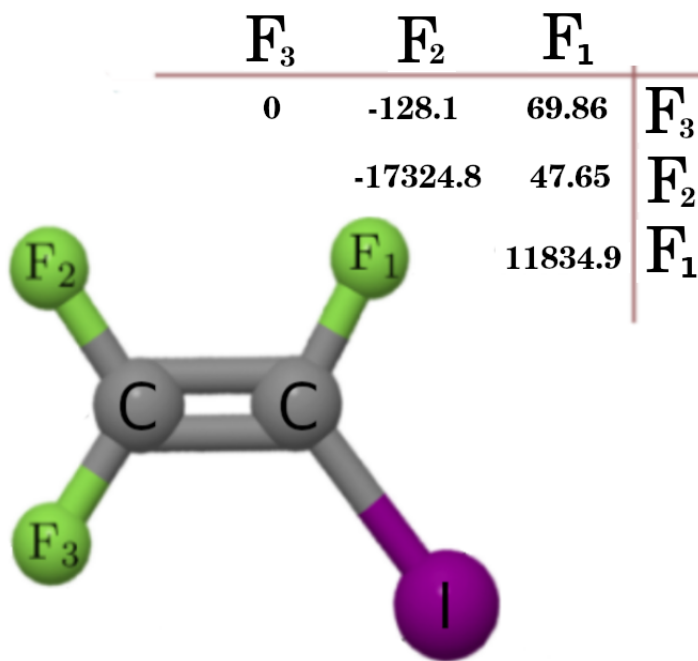


Figure 9 – Iodotrifluoroethylene (Trifluorine) molecule (the same as in Figure 7), see Reference [42, p.3], the F_i are fluorines F_{19} and the remaining atoms are a C_{12} and I_{53} . If the iodine was substituted by another fluorine, then the molecule would be symmetric and the chemical shifts would be zero. The table shows the chemical shifts related to the F_3 nucleus.

3.2.1 Rotating Frame

The description in the rotating frame of the $j - th$ qubit will be given by

$$\mathcal{H}^{(f_j)}(t) = e^{i\mathcal{H}_0^{(f_j)} t/\hbar} (\mathcal{H}_{Zeeman} + \mathcal{H}_{RF} + \mathcal{H}_{int}) e^{-i\mathcal{H}_0^{(f_j)} t/\hbar} - \mathcal{H}_0^{(f_j)}, \quad (3.12)$$

where $\mathcal{H}_0^{(f_j)} = -\frac{1}{2}hf_j(\sigma_z^{(1)} + \sigma_z^{(2)} + \sigma_z^{(3)})$.

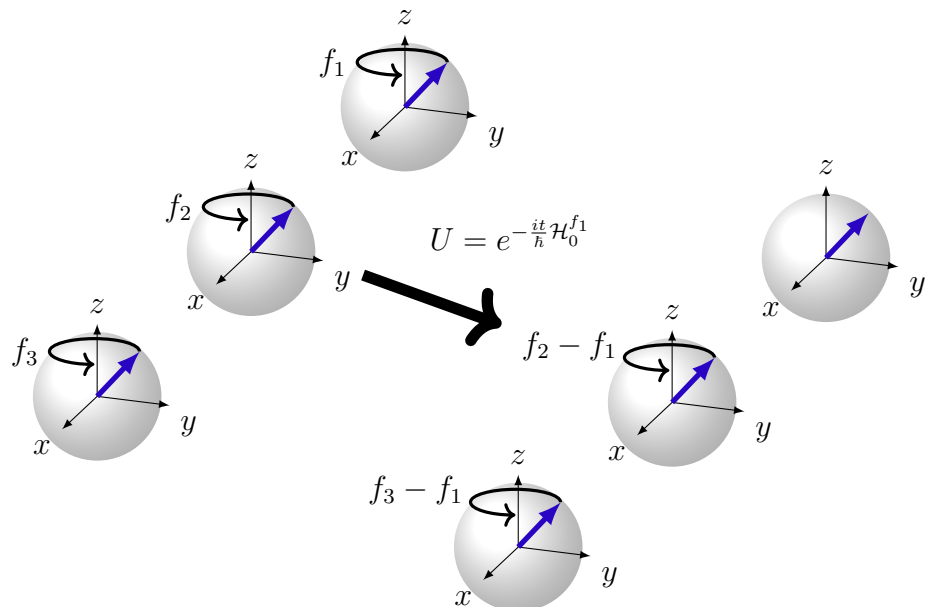


Figure 10 – State vectors Bloch's sphere representation in the laboratory frame oscillate each with its characteristic Larmor frequency f_k , in the interaction picture, the speed of oscillation changes. A three qubit system is represented in the figure, here the change of reference frame is represented by the $U = e^{i\mathcal{H}_0^{(f_j)} t/\hbar}$ term over the big black arrow indicating the direction of the new frame of reference. In the new frame (where the resonance frequency f_1 was chosen, the first spin does not precess, while the others precess in the difference of the frequencies $f_k - f_1$.

Here we have written the expression without the interaction Hamiltonian. It is straightforward to show that $\mathcal{H}_{int}(t)$ commutes with $U = e^{i\mathcal{H}_0^{(f_j)} t/\hbar}$, when it is a function only of $\sigma_z^k \sigma_z^i$, we will therefore not write it on the following calculus, adding it only in Equation (3.19). Then

$$\begin{aligned}
\mathcal{H}^{(f_j)}(t) &= e^{-i\pi f_j t(\sigma_z^{(1)} + \sigma_z^{(2)} + \sigma_z^{(3)})} (\mathcal{H}_{Zeeman} + \mathcal{H}_{RF}) e^{i\pi f_j t(\sigma_z^{(1)} + \sigma_z^{(2)} + \sigma_z^{(3)})} \\
&\quad - \left[-\frac{1}{2} h f_j (\sigma_z^{(1)} + \sigma_z^{(2)} + \sigma_z^{(3)}) \right], \\
\mathcal{H}^{(f_j)}(t) &= + \frac{1}{2} h (f_j - f_1) \sigma_z^{(1)} + \frac{1}{2} h (f_j - f_2) \sigma_z^{(2)} + \frac{1}{2} h (f_j - f_3) \sigma_z^{(3)} \\
&\quad + \frac{1}{2} \hbar \gamma \left[B_x(t) \left(e^{-i\pi f_j t \sigma_z^{(1)}} \sigma_x^{(1)} e^{i\pi f_j t \sigma_z^{(1)}} + e^{-i\pi f_j t \sigma_z^{(2)}} \sigma_x^{(2)} e^{i\pi f_j t \sigma_z^{(2)}} + e^{-i\pi f_j t \sigma_z^{(3)}} \sigma_x^{(3)} e^{i\pi f_j t \sigma_z^{(3)}} \right) \right. \\
&\quad \left. + B_y(t) \left(e^{-i\pi f_j t \sigma_z^{(1)}} \sigma_y^{(1)} e^{i\pi f_j t \sigma_z^{(1)}} + e^{-i\pi f_j t \sigma_z^{(2)}} \sigma_y^{(2)} e^{i\pi f_j t \sigma_z^{(2)}} + e^{-i\pi f_j t \sigma_z^{(3)}} \sigma_y^{(3)} e^{i\pi f_j t \sigma_z^{(3)}} \right) \right], \\
&= \frac{h}{2} \sum_{k=1}^3 (f_j - f_k) \sigma_z^{(k)} + \frac{\gamma \hbar}{4} \sum_{k=1}^3 \left[B_x(t) e^{-i\pi f_j t \sigma_z^{(k)}} \sigma_x^{(k)} e^{i\pi f_j t \sigma_z^{(k)}} + B_y(t) e^{-i\pi f_j t \sigma_z^{(k)}} \sigma_y^{(k)} e^{i\pi f_j t \sigma_z^{(k)}} \right] \\
&= + \frac{h}{2} \sum_{k=1}^3 (f_j - f_k) \sigma_z^{(k)} + \frac{\gamma \hbar}{4} \sum_{k=1}^3 \left[(B_x(t) - iB_y(t)) e^{-i\pi f_j t \sigma_z^{(k)}} \sigma_+^{(k)} e^{i\pi f_j t \sigma_z^{(k)}} + \right. \\
&\quad \left. + (B_x(t) + iB_y(t)) e^{-i\pi f_j t \sigma_z^{(k)}} \sigma_-^{(k)} e^{i\pi f_j t \sigma_z^{(k)}} \right], \\
\mathcal{H}^{(f_j)}(t) &= \frac{h}{2} \sum_{k=1}^3 (f_j - f_k) \sigma_z^{(k)} + \frac{\gamma \hbar}{4} \sum_{k=1}^3 \left[(B_x(t) - iB_y(t)) \sigma_+^{(k)} e^{-i2\pi f_j t} + (B_x(t) + iB_y(t)) \sigma_-^{(k)} e^{2i\pi f_j t} \right], \tag{3.13}
\end{aligned}$$

where we have used the relation $\sigma_{\pm} = \sigma_x \pm i\sigma_y$, and the following result

$$e^{s\sigma_z} \sigma_{\pm} e^{-s\sigma_z} = \sigma_{\pm} e^{\pm 2s}, \tag{3.14}$$

Writing $B_x(t) \pm iB_y(t) = \Omega(t) e^{\pm i\varphi(t)}$, where $\Omega(t), \varphi(t) \in \mathbb{R}$, our equation becomes

$$\mathcal{H}^{(f_j)}(t) = \frac{h}{2} \sum_{k=1}^3 (f_j - f_k) \sigma_z^{(k)} + \frac{\gamma \hbar}{4} \Omega(t) \sum_{k=1}^3 \left[\sigma_+^{(k)} e^{-i2\pi f_j t - \varphi(t)} + \sigma_-^{(k)} e^{2i\pi f_j t + \varphi(t)} \right].$$

Now, remembering that $2\pi f_j = \omega_j$, and the Pauli matrices relations, we can rewrite the final part of the equation as a function of σ_x and σ_y

$$\begin{aligned}
&\sum_{k=1}^3 (\sigma_x^{(k)} + i\sigma_y^{(k)}) e^{-i\omega_j t - \varphi(t)} + (\sigma_x^{(k)} - i\sigma_y^{(k)}) e^{i\omega_j t + \varphi(t)} \\
&= 2 \sum_{k=1}^3 \sigma_x^{(k)} \cos [\omega_j t + \varphi(t)] + \sigma_y^{(k)} \sin [\omega_j t + \varphi(t)],
\end{aligned}$$

the final expression for the Hamiltonian is then given by

$$\mathcal{H}^{(f_j)}(t) = \frac{\hbar}{2} \sum_{k=1}^3 (\omega_j - \omega_k) \sigma_z^{(k)} + \frac{\hbar \gamma}{2} \Omega(t) \sum_{k=1}^3 \left[\sigma_x^{(k)} \cos (\omega_j t + \varphi(t)) + \sigma_y^{(k)} \sin (\omega_j t + \varphi(t)) \right]. \tag{3.15}$$

Given that all the above considerations are still valid for N nuclei of the same isotope, one concludes the following expression

$$\mathcal{H}^{(f_j)}(t) = \frac{\hbar}{2} \sum_{k=1}^N (\omega_j - \omega_k) \sigma_z^{(k)} + \frac{\hbar\gamma}{2} \Omega(t) \sum_{k=1}^N [\sigma_x^{(k)} \cos(\omega_j t + \varphi(t)) + \sigma_y^{(k)} \sin(\omega_j t + \varphi(t))]. \quad (3.16)$$

One could wish to make the role of the chemical shifts δ_k clearer, and so write f_i in terms of the corresponding shifts. Making this adjustment and adding the interaction Hamiltonian, one gets

$$\mathcal{H}^{(f_j)}(t) = \frac{\hbar\gamma}{2} B_0 \sum_{k=1}^N (\delta_j - \delta_k) \sigma_z^{(k)} + \frac{\hbar}{4} \sum_{\substack{k=1, \\ i \neq k}}^N J_{ik} \sigma_z^{(i)} \sigma_z^{(k)} + \quad (3.17)$$

$$+ \frac{\hbar\gamma}{2} \Omega(t) \sum_{k=1}^N [\sigma_x^{(k)} \cos(\omega_j t + \varphi(t)) + \sigma_y^{(k)} \sin(\omega_j t + \varphi(t))]. \quad (3.18)$$

which represents our final expression.

Experimentally, one can choose $k = j \in \{1, \dots, N\}$, so that the Zeeman terms $(\delta_j - \delta_k)$ in the chosen j are zero, and the RF Hamiltonian oscillates according to the chosen qubit. Naturally, one can also choose a frequency ω_j such that a detuning occurs.

So choosing the frequency of the RF field tuned with the interaction picture frequency $\varphi(t) = -\omega_j t + \phi(t)$, the Hamiltonian for a homonuclear system in the interaction picture of the f_j rotating frame may be written as

$$\mathcal{H}^{(f_j)}(t) = \frac{\hbar\gamma}{2} B_0 \sum_{k \neq j}^N (\delta_j - \delta_k) \sigma_z^{(k)} + \frac{\hbar}{4} \sum_{\substack{k=1, \\ i \neq k}}^N J_{ik} \sigma_z^{(i)} \sigma_z^{(k)} + \frac{\hbar\gamma}{2} \Omega(t) \sum_{k=1}^N [\sigma_x^{(k)} \cos(\phi(t)) + \sigma_y^{(k)} \sin(\phi(t))]. \quad (3.19)$$

3.3 Heteronuclear systems

Remember that in Equation (3.12) we reduced the complexity of our argument by restricting the analysis to an equation with one type of isotope and $N = 3$. For the heteronuclear case however, we will discuss the converse conditions, i.e., two different isotopes and 1 for each one of the isotope types. For example, take the Chloroform molecule with two qubits: and Hydrogen and a Carbon 13. In this case, we will be using a unitary transformation to the system usually called the *bi-rotating frame picture*, given by the unitary transformation $U = e^{i\mathcal{H}_0^{(f_1, f_2)} t/\hbar}$, where the exponent is $\mathcal{H}_0^{(f_1, f_2)} = -\frac{1}{2}\hbar(f_1\sigma_z^{(1)} + f_2\sigma_z^{(2)})$. Then, Equation (3.12) is written as

$$\mathcal{H}^{(f_1, f_2)}(t) = e^{i\mathcal{H}_0^{f_1, f_2}t/\hbar}(\mathcal{H}_{Zeeman} + \mathcal{H}_{RF} + \mathcal{H}_{int})e^{-i\mathcal{H}_0^{f_1, f_2}t/\hbar} - \mathcal{H}_0^{(f_1, f_2)}. \quad (3.20)$$

Once again, \mathcal{H}_{Zeeman} and \mathcal{H}_{int} commute with $\sigma_z^{(k)}$ one can write

$$\mathcal{H}^{(f_1, f_2)}(t) = \mathcal{H}_{Zeeman} + e^{i\mathcal{H}_0^{(f_1, f_2)}t/\hbar}\mathcal{H}_{RF}e^{-i\mathcal{H}_0^{(f_1, f_2)}t/\hbar} + \mathcal{H}_{int} - [-\frac{1}{2}h(f_1\sigma_z^{(1)} + f_2\sigma_z^{(2)})], \quad (3.21)$$

but remember that $\mathcal{H}_{Zeeman} = -\frac{1}{2}h(f_1\sigma_z^{(1)} + f_2\sigma_z^{(2)})$, in the case with one of each of two different isotopes, so these terms cancel out and what is left is only the RF and interaction term. By Equation (3.11), and commuting operators with different k , we obtain a similar expression to the RF term.

$$\mathcal{H}_{RF} = \frac{\gamma\hbar}{4} \sum_{k=1}^2 \left[B_x(t)e^{-i\pi f_k t \sigma_z^{(k)}} \sigma_x^{(k)} e^{i\pi f_k t \sigma_z^{(k)}} + B_y(t)e^{-i\pi f_k t \sigma_z^{(k)}} \sigma_y^{(k)} e^{i\pi f_k t \sigma_z^{(k)}} \right].$$

This time, however, we will suppose that the RF field has two contributions, which we will write as $\mathbf{B}_1(t) = \mathbf{B}_{obs}(t) + \mathbf{B}_{dec}(t)$, so that $B_{x_i}(t) = B_{x_i, obs}(t) + B_{x_i, dec}(t)$. This is justified, since one can set as many different sources of RF field as one wishes, each one with different amplitude and phase. However, it should be noted that there are experimental (and financial) limitations to such practice and numbers of sources are usually limited to 4 (in our case 2), one for each given isotope type in the sample. The subscripts are written as “obs” and “dec” for *observer* and *decoupler*, which are terms that are specific to NMR research and precede the use of NMR as a quantum computing practice [34, 54].

Following the same reasoning given for the homonuclear system, where the magnetic field is

$$B_{x, obs}(t) \pm iB_{y, obs}(t) = \Omega_{obs}(t)e^{\pm i\varphi_{obs}(t)}, \text{ for the observer, and} \quad (3.22)$$

$$B_{x, dec}(t) \pm iB_{y, dec}(t) = \Omega_{dec}(t)e^{\pm i\varphi_{dec}(t)}, \text{ for the decoupler,} \quad (3.23)$$

and using again the relation $\sigma_{\pm} = \sigma_x \pm i\sigma_y$, one ends up with

$$\begin{aligned} \mathcal{H}_{RF}(t) &= \frac{\gamma\hbar}{4} \Omega_{obs}(t) \sum_{s=1}^2 \left[\sigma_+^{(s)} e^{-i2\pi f_s t - \varphi_{obs}(t)} + \sigma_-^{(s)} e^{2i\pi f_s t + \varphi_{obs}(t)} \right] \\ &\quad + \frac{\gamma\hbar}{4} \Omega_{dec}(t) \sum_{s=1}^2 \left[\sigma_+^{(s)} e^{-i2\pi f_s t - \varphi_{dec}(t)} + \sigma_-^{(s)} e^{2i\pi f_s t + \varphi_{dec}(t)} \right], \end{aligned}$$

now choosing $\varphi_{obs}(t) = -2\pi(f_1 - \Delta\omega_{obs})t + \phi_{obs}$ for the observer and for the decoupler $\varphi_{dec}(t) = -2\pi(f_2 - \Delta\omega_{dec})t + \phi_{dec}$, the terms with exponentials become (for the obs):

$$\sigma_+^{(1)} e^{-(\Delta\omega_{obs}t + \phi_{obs})} + \sigma_-^{(1)} e^{(\Delta\omega_{obs}t + \phi_{obs})} + \\ \sigma_+^{(2)} e^{-i2\pi(f_2 - f_1 + \Delta\omega_{dec})t - \phi_{obs}} + \sigma_-^{(2)} e^{2i\pi(f_2 - f_1 + \Delta\omega_{dec})t + \phi_{obs}},$$

one obtains the expression for the *dec* changing $1 \longleftrightarrow 2$.

An approximation is needed here: note that one can choose $\Delta\omega$ (the *detuning*) to be of the order of kHz (or even Hz), while, since f_1 and f_2 are from nuclei of different atomic number, their difference is then of the order of MHz. Therefore, the exponential terms with the $(f_1 - f_2)t$ in the argument are oscillating with much greater speed than the ones without it, and can be set to zero, since their temporal average will not contribute to the measurements. This approximation is called *rotating wave approximation* (RWA) [50, p.152]. This reduces the complexity of the RF hamiltonian and one can rewrite it as

$$\mathcal{H}_{RF}(t) = \frac{\gamma\hbar}{4}\Omega_{obs}(t)\left[\sigma_+^{(1)} e^{-(\Delta\omega_{obs}t + \phi_{obs})} + \sigma_-^{(1)} e^{(\Delta\omega_{obs}t + \phi_{obs})}\right] \\ + \frac{\gamma\hbar}{4}\Omega_{dec}(t)\left[\sigma_+^{(2)} e^{-(\Delta\omega_{dec}t + \phi_{dec})} + \sigma_-^{(2)} e^{(\Delta\omega_{obs}t + \phi_{dec})}\right],$$

writing it in terms of σ_x and σ_y , as done in the homonuclear case, and adding the interaction hamiltonian, one finally obtains the total hamiltonian in the bi-rotating frame

$$\mathcal{H}^{(f_1, f_2)}(t) = \frac{\hbar}{4}J_{12}\sigma_z^{(1)}\sigma_z^{(2)} + \frac{\hbar\gamma}{2}\Omega_{obs}(t)\left[\sigma_x^{(1)} \cos(\Delta\omega_{obs}t + \phi_{obs}) + \sigma_y^{(1)} \sin(\Delta\omega_{obs}t + \phi_{obs})\right] \\ + \frac{\hbar\gamma}{2}\Omega_{dec}(t)\left[\sigma_x^{(2)} \cos(\Delta\omega_{dec}t + \phi_{dec}) + \sigma_y^{(2)} \sin(\Delta\omega_{dec}t + \phi_{dec})\right].$$

By writing this expression in the bi-rotating frame, we have managed to eliminate the Zeeman hamiltonian while also reducing the complexity by use of the RWA approximation. This equation is remarkable for making explicit that, in a heteronuclear 2 qubit system, one can control each spin independently, since all dec terms are associated with the second qubit and all obs with the first. Precision is greatly enhanced by avoiding crossed terms, this is quite a experimental advantage in comparison with the homonuclear case discussed earlier, and will be shown to be quite sufficient for tight control in small systems in the following sections.

3.4 Example: Mixed systems

As can be seen from the Figure 11, some systems may have subsets that are homonuclear or heteronuclear systems. For illustration purposes, we will write the hamiltonian for a system such as this one, were there are two isotope types $\{C, H\}$, and each has $N_C = 7$ and $N_H = 5$, and two RF probes are available, it has the form:

C_1	-30 020.09											
C_2	57.58 -8780.39											
C_3	-2.00 32.67 -6245.45											
C_4	0.02 0.30 0.00 -10 333.53											
C_5	1.43 2.62 -1.10 33.16 -15 745.40											
C_6	5.54 -1.66 0.00 -3.53 33.16 -34 381.71											
C_7	-1.43 37.43 0.94 29.02 21.75 34.57 -11 928.71											
H_1	0.04 1.47 2.03 166.6 4.06 5.39 8.61 -3307.85 -2464.15 -12.41 -2155.59											
H_2	4.41 1.47 146.6 2.37 0.00 0.00 0.00 0.00 0.18 -12.41 -2155.59											
H_3	1.86 2.44 146.6 0.04 0.00 0.00 0.00 0.00 0.18 -12.41 -2155.59											
H_4	-10.10 133.60 -6.97 6.23 0.00 5.39 3.80 -0.68 1.28 6.00 -2687.69											
H_5	7.10 -4.86 3.14 8.14 2.36 8.52 148.5 8.46 -1.0 -0.36 1.30 -3645.08											
	C_1	C_2	C_3	C_4	C_5	C_6	C_7	H_1	H_2	H_3	H_4	H_5

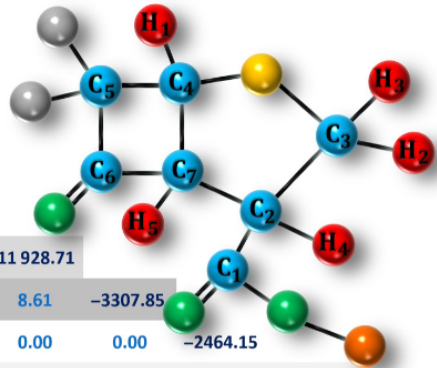


Figure 11 – a 12-qubit molecule from [44] : per-13C-labeled (1S,4S,5S)-7,7-dichloro-6-oxo-2-thiabicyclo[3.2.0]heptane-4-carboxylic acid. The diagonal elements are given by the chemical shift of each nuclei, while the non-diagonal elements give the J_{ij} coupling between two nuclei. This molecule holds the record for largest number of qubits in a NMR system

$$\mathcal{H}(t) = \frac{\hbar}{2} \sum_{k_C=1}^{N_C} (\omega_{dec} - \omega_{k_C}) \sigma_z^{(k_C)} + \frac{\hbar\gamma}{2} \Omega_{dec}(t) \sum_{k_C=1}^{N_C} [\sigma_x^{(k_C)} \cos(\phi(t)) + \sigma_y^{(k_C)} \sin(\phi(t))] \quad (3.24)$$

$$+ \frac{\hbar}{2} \sum_{k_H=1}^{N_H} (\omega_{obs} - \omega_{k_H}) \sigma_z^{(k_H)} + \frac{\hbar\gamma}{2} \Omega_{obs}(t) \sum_{k_H=1}^{N_H} [\sigma_x^{(k_H)} \cos(\phi(t)) + \sigma_y^{(k_H)} \sin(\phi(t))] \quad (3.25)$$

$$+ \frac{\hbar}{4} \sum_{\substack{k=1, \\ i \neq k}}^{N_C+N_H} J_{ik} \sigma_z^{(i)} \sigma_z^{(k)}, \quad (3.26)$$

where $1 \leq k_H \leq N_H$, and $1 \leq k_C \leq N_C$. Note that we have chosen the RF frequencies so that there is no detuning $\Delta\omega$. Some care has to be taken here, as the justifications for the secular approximation, that lets us use J_{ik} as a scalar coupling instead of a tensor, may not be permissible here. Equation (3.24) should then be taken with care, as it may be a bad approximation of the actual dynamics of such a complicated molecule.

Part II

Quantum Optimal Control

Chapter 4

A few elements of Quantum Optimal Control Theory

In this Chapter we will discuss some of the definitions and theories in the field of Quantum Optimal Control Theory (QOCT). The area of research that retains the name of *Optimal Control* is not bounded by any major area of research that one finds in the university departments, in fact it uses multiple resources from other subjects such as Physics, applied Mathematics, and Engineering [31, p.1].

The main objective of optimal control is to manipulate a dynamical process in order to realize a specific task. To achieve this, however, physical limits and constraints imposed by the devices at hand have to be ingeniously managed in order to maximize automation and control. This is a major concern in quantum systems as these have to be majorly isolated from the ambient and avoid sources of decoherence, while also being highly operable.

A caveat is to be regarded in order to proceed. Quantum systems cannot be measured during the evolution without losing the main character of interest of quantum mechanics. Therefore, the most common resources in classical systems of control, such as *closed-loop control* are not an option depending on the desired goals. By closed-loop control it is meant a control method that relies in a action-measurement-feedback loop, also called ‘online’ method [31, p.19]. This method is commonly used in the field of robotics, where a robot may have a camera, or a laser, attached and has a fast frame-rate of new data (measurements) for every action the robot took [31, p.18]. So for every step, new measurements are taken, which in their turn algorithmically decide on new control parameters in order to take a new action.

It should be clear that QOCT must take a radically different approach, and has to reformulate of many of the major developments in the field of classical control theory. Because every measurement radically changes the system evolution, and no inference can be made on the system prior state (in a general sense) after a single measurement. So the

approach we will use here is called the *open-loop/offline* approach.

Notwithstanding, it is possible to still use measurements in QOCT, although not in the same way as in the classical protocols. One could use measurements in ancilla qubits to improve the system's control, by producing non-linear ancilla assisted interactions. Not only this but many of informational techniques usually attributed to Quantum Thermodynamics (see References [9, 19, 55] for more details), such as shortcut to adiabaticity and quantum feedback, are importable to the field of QOCT and provide complementary strategies with peculiar advantages and limitations [31].

A showcase of the accuracy of quantum systems enhanced by QOCT can be found in [21]. In this experiment the authors loaded a BEC of ultra-cold Rubidium atoms in a one-dimensional optical lattice formed by two counter propagating laser beams with the same wavelength but different phase. With the use of highly controllable phase, and a gradient-based algorithm to optimize the desired way to “shake” the optical lattice back and forth, by tuning the lasers optimally, the authors could bring the system to the desired state of a superposition of speeds for the Rb atoms. Then reading the positions of the momentum-state populations, by ballistic expansion (a well established technique in the field of BEC), the BEC could then be used to “print” letters column by column, producing the image in Figure 12.



Figure 12 – Illustration of an experimental BEC dot printer. Each dot in a column represents a absorption from a ballistic expansion of a momentum state population of the optical lattice. Further details can be obtained in Reference [21].

it should be clear that the use cases of such fine tuning are above and beyond the use in atomic printers, and can be extended to the fields of quantum simulation and metrology.

4.1 Controllability in Quantum systems

In this section we wish to provide a set of definitions in order to make clearer what is meant by the words “control” and other terms that are ubiquitous in this work. In the following we will closely follow the review in [31].

When dealing with quantum devices, multiple questions arise on how much can be done with them. One could be asking about which states (or gates) can be prepared, how robust to noise is your system, or even what are the main sources of noise in the implementation. Those are valid questions, especially when in times as of today where

quantum devices are especially noisy. The quest for quantum computers that are robust to noise is a well known issue in the field. This has been so much the topic of discussion that the term *noise intermediate-scale quantum* (NISQ) era [45], coined to refer to the current state of affairs in quantum devices, has become familiar to the research field, and is regarded by many as a token of the possibilities of applications in the future midterm.

Moreover, one should differentiate between the terms QOCT and Quantum Error Correction. The first is focused mostly in how to parameterize the system in terms of experimental inputs in order to achieve higher state access, while Error Correction is mostly interested in the case where error has already occurred, and then how to retrieve the original information. One can think pedagogically in terms of the following example: the first (QOCT) is needed to avoid an unwanted bit-flip gate, while the second (Error Correction) is design to recover the state that has suffered a bit-flip *after* the flip [57, p.657].

A qubit that is noiseless is sometimes called a *logical qubit* (in opposition to the *physical qubits*), this is achieved by introducing multiple physical qubit that compose it by cleverly designed algorithms and information redundancy. Until the year of 2023, it was estimated that it would be needed around the order of 1000 physical qubits for a single logical qubit to exist [27, p.60], however a recent paper by QuERA has experimentally demonstrated that in a atom array hardware it is possible to achieve 48 logical qubits with only 280 physical qubits [10], by using multiple techniques in QOCT and Quantum Error Correction. This novelty is a showcase of how the area of research in Quantum Computing is rapidly changing due to the introduction of new hardware, theory, and experimental practices.

Naturally, in the NISQ era, the use of Quantum Error Correction is of utmost importance in Quantum Information Processing. We will however avoid this topic in this discussion, for the sake of succinctness. The reader may refer to specific texts as [10, 57]. That said, the use of control methods is of utmost importance when noise and decoherence are still in lack of a definitive solution. Let us then proceed to what is meant by this.

Definition 4.1.1. *A control system is formally described by an equation of motion of a physical system, e.g. an ODE or PDE involving “parameters” to be adjusted. These parameters are called controls.*

For example, the harmonic oscillator equation

$$\ddot{x} = -kx \tag{4.1}$$

has k as a time-independent control. These can become more complicated and the number of controls can escalate quickly. A more complicated example is given by the famous

Lotka-Volterra equations [38, p.79]

$$\frac{dx}{dt} = \alpha x - \beta xy, \quad (4.2)$$

$$\frac{dy}{dt} = \delta xy - \gamma y. \quad (4.3)$$

These equations have as controls the terms $\alpha, \beta, \delta, \gamma$, and are a standard example of how a small perturbation in the parameters may change the systems evolution.

The controls in a system may be parameterized by the time variable t , and therefore be time-dependent. As the reader may have realized, this is the case with Equation (3.19), where $\Omega(t), \phi(t)$ are the controls, and are used to “steer” the system by changing its equation of motion. Most of this dissertation is dedicated to what is the best way to define these functions, but I digress, this will be the topic of all the following chapters. For now, let us continue with our definitions.

Definition 4.1.2. *A system is said to be Controllable if any initial state can be transformed into any desired target state.*

This means that a controllable system can take any ρ_0 and map it to a different $\mathcal{E}(\rho_0) = \rho_f$ by only changing the controls and respecting the functional form of the equation of motion. Given a specific ρ_0 the set of all possible $\mathcal{E}(\rho_0)$ is called the *reachable set* for this state. This means that if the reachable set of all initial states is equal to the entire space, then the system is controllable.

The reader may think that this a very nonfactual state of affairs, since, experimentally, it is quite challenging to reach a perfect overlap of a certain state, and usually we are only interested in approximate states. For example, when running a quantum annealing, the algorithm does not need to reach the ground state exactly to have satisfactory results [58]. This motivates the following definition: If not all states are reachable, e.g. some states are limit points out of the reachable set, but the reachable set contains all interior points of the space, then the system is called *accessible*.

The class of all control systems is a field of study of its own, and has many nontrivial properties. A well known and more well behaved subclass of control systems that is called *Linear Time Invariant* (LTI) systems. Moreover, when both the states and the control are linear, in this case, these are called *Bilinear control systems*.

By LTI, we mean that if one applies a linear combination of controls to an equation of motion, then the separation by linearity of these controls is also a valid equation of motion to the system [41]. This means that, taking Equation (4.1) and control $\mathcal{C}(\alpha(t))$, one has

$$\begin{aligned}
\mathcal{C}(c_1\alpha_1(t) + c_2\alpha_2(t))[\ddot{x} + kx] &= 0 \\
\ddot{x} + k(c_1\alpha_1(t) + c_2\alpha_2(t))x &= 0 \\
\ddot{x} + kc_1\alpha_1(t)x + c_2\alpha_2(t)x &= 0 \\
\ddot{x} + c_1\mathcal{C}(\alpha_1(t))[kx] + c_2\mathcal{C}(\alpha_2(t))[kx] &= 0 \\
c_1\mathcal{C}(\alpha_1(t))[\ddot{x} + kx] + c_2\mathcal{C}(\alpha_2(t))[\ddot{x} + kx] &= 0
\end{aligned}$$

and by *time-invariance* we mean that it does not matter when the input was applied. The intuition behind this is that the system is usually in some state of equilibrium before the control is applied, so that applying it at time t or $t + t_0$ is equivalent, i.e., results in the same final state. We will see that if t_0 is sufficiently small we can consider the system as time-invariant in NMR quantum computing. To avoid any misunderstanding a clarification is needed: The term “time-invariant” used in this context may be somewhat confusing to physicists, who understand that time invariance means that the system is symmetric under variations in (any) time, while in the context of signal processing, this term means time-invariant only in the initial time where the control is turned on.

LTI systems are particularly manageable, as they possess the property that a control in time $\alpha(t)$ can be decomposed in a linear combination of a set of more basic controls. For example: a very complex signal as a continuous oscillating function can be decomposed in Fourier series, by the LTI property, the output will also be decomposable in a linear sum. Furthermore, because Fourier transforms (discussed in Chapter 5) are linear transformations, and are a standard method to solve differential equations, wherever they can be used many properties from LTI are inherited from the input to the output. And as will be seen in Section 6.4, many properties can be inferred from the Fourier transform of the control input.

In a more formal note, an interesting theorem results from the following

Theorem 4.1.3 (Lie algebra rank condition). *Given a bilinear control of a finite dimension (N) quantum system. If the linear span generated by all iterated commutators among the system and the control Hamiltonians amounts to the Lie algebra $\mathfrak{su}(N)$, then the system is fully controllable (also called universal).*

This theorem does not discriminates if the states are mixed or pure. If one restricts the reachable set to the span of pure states, then it suffices to the Lie algebra being the one of unitary symplectic matrices of dimension N . This theorem, however, is unknown to be true for infinite dimensions [31], and the results for open systems are more complicated.

4.1.1 A note on controllability in open quantum systems

The case of open quantum systems is surely more convoluted. It should be clear by the definitions above that open quantum systems, that no open system is controllable (in the sense discussed above), as the irreversible time evolution of the system removes some possible states through noise. However, they are still accessible, when control is present. Some special properties can be derived for unital maps, in the like of the theorem above:

Theorem 4.1.4. *If the system Lie algebra is isomorphic to $\mathfrak{gl}_{N^2-1}(\mathbb{R})$, i.e., the the Lie algebra of all real square matrices of dimension $(N^2 - 1)$, then the system is accessible.*

The two theorems above are very similar, but the fact that the first implies controllability and the second accessibility, is a consequence of the fact that the Lie groups $SU(N)$ and $GL_{N^2-1}(\mathbb{R})$ have different compactness properties, where the former can rightly express the property of time reversal while the second cannot (as it is for dissipative systems).

When the controls have limited bandwidth, time, and power, the number of required controls upper bound, defined above as $N^2 - 1$, cannot be addressed analytically anymore. In real quantum systems, however the controls are a small subset of all possible controls. This means that the real number of required controls is not an easy claim make, as these should scale up with the system dimension, while the control apparatus surely does not scale so fast [5]. To produce realistic control solutions it is then necessary to focus on the main sources of noise and what else is available at hand. This will be the topic of the next section on the application of QOCT to NMR.

A final consideration on QOCT and Thermodynamics: Open systems can be characterized by many mathematical models, and are usually simplified by assuming that are Markovian, or that these obey the Lindblad Equations. Both of these mathematical formulations are ubiquitous in Quantum Thermodynamics and thinking about uniting both fields should be a natural consequence, when one realizes that [31, p.36]

1. Certain control tasks require a change of entropy (due to irreversibility), such as reset of thermalization, or actively cooling.
2. QOCT may be used to optimize the cycles in quantum heat engines
3. Experimental realizations of both areas of research use very similar platforms
4. Quantum Thermodynamics may supply a resource theory very much needed to address the cost of control.

These claims should encourage future students to take on the endeavor of further relating both areas of research, as this connection (in terms of control and signal systems) is widely under explored in the literature.

Chapter 5

Signal Processing and Qubit Control

Now that we have a grasp of the physical model of our sample, given in Chapter 3, and the definitions of QOCT are clear, in this section we will discuss how to produce and control signals for quantum information processing in NMR.

Remember that in Equation (3.12) for the homonuclear case, we moved to a rotating frame by transforming the observables to the interaction picture with frequency f_j . This frequency is in the order of MHz for each nucleus. By choosing the frequency to be equal to one of the qubits resonance frequency, the remaining nuclei have a difference of rotation in the order of kHz due to the Zeeman part of the hamiltonian, as exemplified in Figure 10. This is an effect of changing reference frames, since now the rotation of the other qubits has an effective Larmor frequency $f_j - f_k \approx 10 \text{ kHz}$.

In a frequency plot, centered in the first qubit, we should expect the other frequencies to be tens of kHz apart. To address such frequencies individually can become quite challenging, in this section we will deal with these issues through signal processing theory.

5.1 Time and Frequency domain

Fourier transforms are familiar mathematical objects in all areas of Science and Engineering. As one may remember from undergraduate Physics courses, it is an integral transform that takes functions $f : t \in \mathbb{R} \rightarrow f(t) \in \mathbb{R}$ to a function $F : \omega \in \mathbb{R} \rightarrow F(\omega) \in \mathbb{R}$. The Fourier transform $\mathcal{F}(f(t)) = F(\omega)$ of a periodic function of time $f(t)$, with period T is given by [4, p.969]

$$F(\omega) = \frac{1}{T} \int_{T/2}^{T/2} f(t) e^{-i \frac{2\pi j}{T} \omega t} dt,$$

when dealing with an infinite period the expression becomes

$$F(\omega) = \frac{1}{\sqrt{2\pi}} \int_{-\infty}^{\infty} f(t) e^{-i\omega t} dt.$$

A famous example of such transforms is the delta function, with

$$\delta(t) = \begin{cases} \infty & \text{if } t = 0, \\ 0 & \text{otherwise} \end{cases} \quad (5.1)$$

$$F(\omega) = \frac{1}{\sqrt{2\pi}} \int_{-\infty}^{\infty} \delta(t) e^{-i\omega t} dt = \frac{1}{\sqrt{2\pi}}, \quad (5.2)$$

This means that the Fourier transform of an infinite spike is a constant function on all frequencies.

Now let us give some context of applications of this transform to the problem of qubit control. Remember that in our system, one could experimentally control the RF field $\mathbf{B}_1(t)$ by tweaking its amplitude $\Omega(t)$ and its phase $\phi(t)$. By looking at the Equation (3.19) one sees that, by changing the phase, one controls the direction of rotation in the Bloch sphere, i.e., which Pauli operator acts on the system, and by controlling the amplitude $\Omega(t)$ one changes the intensity of the field. By taking the Fourier transform $\mathcal{F}(\Omega(t)) = \tilde{\Omega}(\omega)$ one obtains a function of the frequencies that act on the qubits. Having qubits that are kHz apart in the frequency domain, makes it difficult to act on a single one. Ideally, one could build a function to target a single frequency, i.e., $\mathcal{F}(\Omega(t)) = \delta(\omega)$. How to proceed in building such strongly narrow functions in frequency will be the subject of the next section.

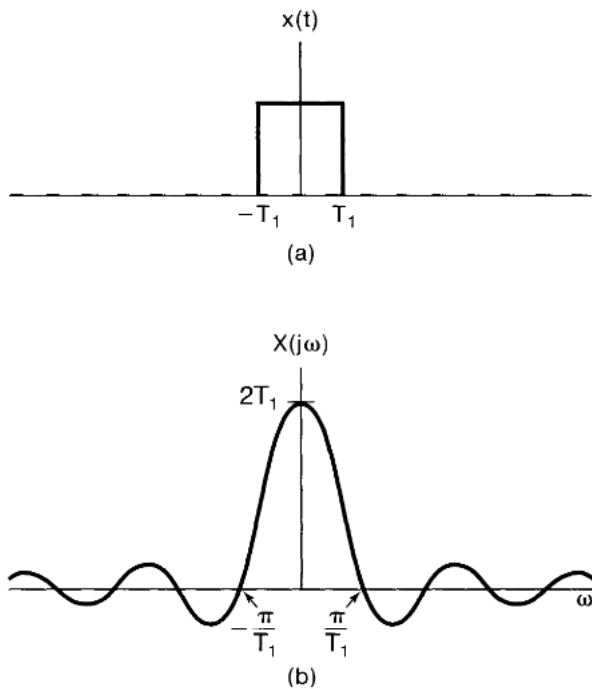


Figure 13 – Square pulse (above) and its Fourier transform (below), the sinc(.) function [41, p. 293]

In our usual practice in the RMN laboratory, we commonly use squared pulses (of around 12 µs). Remember that one could write a square function as the difference between Heavyside step functions $\Theta(t - T_1)$, and so their Fourier transform has the form

$$\mathcal{F}\{\Theta(t + T_1) - \Theta(t - T_1)\} = \frac{1}{\sqrt{2\pi}} \int_{-T_1}^{T_1} e^{-i\omega t} dt = \sqrt{\frac{2}{\pi}} \frac{\sin(\omega T_1)}{\omega},$$

of the $\text{sinc}(\omega) = \sin(\omega)/\omega$. In the frequency domain such pulses have the format as shown in Figure 13.

The sinc function has infinite oscillations, both to the right and to the left. It then acts on the other qubits to a lesser extent, but its effect is still present, the closer the frequencies of the qubits are, the stronger the undesired effect of the pulse is on the other ones, see Figure 14.

This is, once again, an issue that does not occur in heteronuclear systems, as the frequencies are sufficiently far apart and the amplitude of oscillations of the *sinc* function are already very small farther along the ω axis, for this reason squared pulses are good controls in this case.

5.2 Modulating pulses in time

The Fourier transform has many important properties. Being defined by an integral, it then inherits many desired characteristics: It is a linear transformation; By integrating

continuous functions, we guarantee that the result is continuous, and may sometimes give continuous functions as a result when dealing with non-continuous functions in its domain. Another key property of the Fourier transform is known as its *duality*: if the function $f(t)$ has the Fourier transform $F(\omega)$, then, given a function of ω with the same functional form of F , i.e., $F(t)$, its Fourier transform has the functional form of $f(\omega)$.

A straightforward conclusion would be to use the duality property and invert the case discussed in the last section, to pulse a constant pulse and obtain a dirac delta on the frequency, i.e. $f(t) = \frac{1}{\sqrt{2\pi}} \rightarrow F(\omega) = \delta(\omega - \omega_k)$. By looking at Figure 14, one may quickly realize that infinitely long pulses are impractical. Given that NMR systems have a T2 decoherence time of around 2 to 4 seconds, experiments would apply a short number of pulses before the system loses its quantum properties.

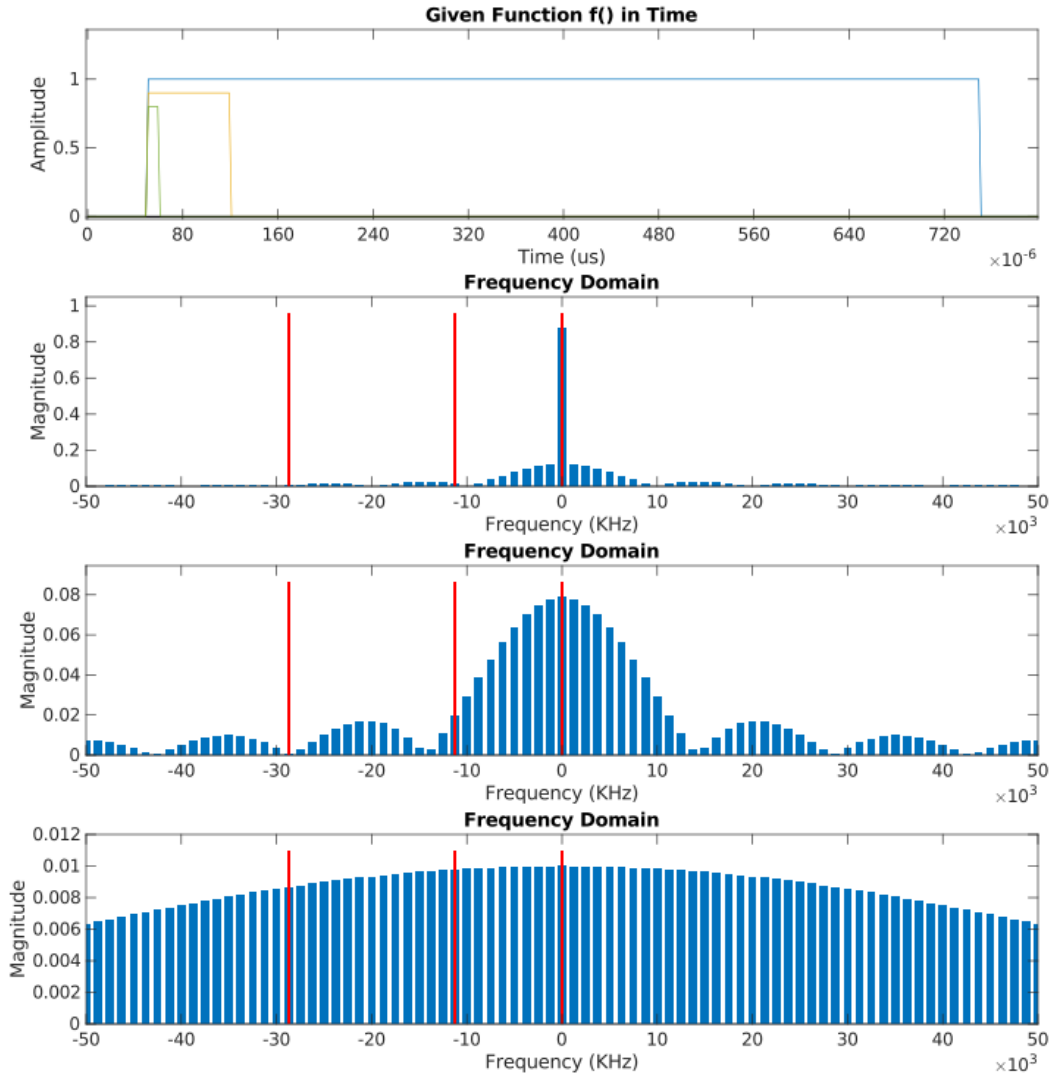


Figure 14 – Three different square pulses and their Fourier transforms plotted below. The first pulse has a time of 700 μ s, the second 70 μ s, and the last 10 μ s. By restricting the time, the frequency width gets larger. The values for the frequencies of the 3 qubits in a Trifluorine molecule are also plotted in red, the frequency plot is centered at the rightmost qubit resonance frequency.

However, due to the duality property of the Fourier transform, by pulsing a conveniently tailor made $\text{sinc}(t)$ function, one could obtain an approximate square function $\Theta(\omega)$ that contains in its non-zero image only one spectrum. See the Figure 15 panel (a) for the example of duality, and (b) where the pulse was truncated (respecting the limitation of finite times) and lifted to guarantee a positive amplitude. How to find such pulse modulations is the subject of the next section.

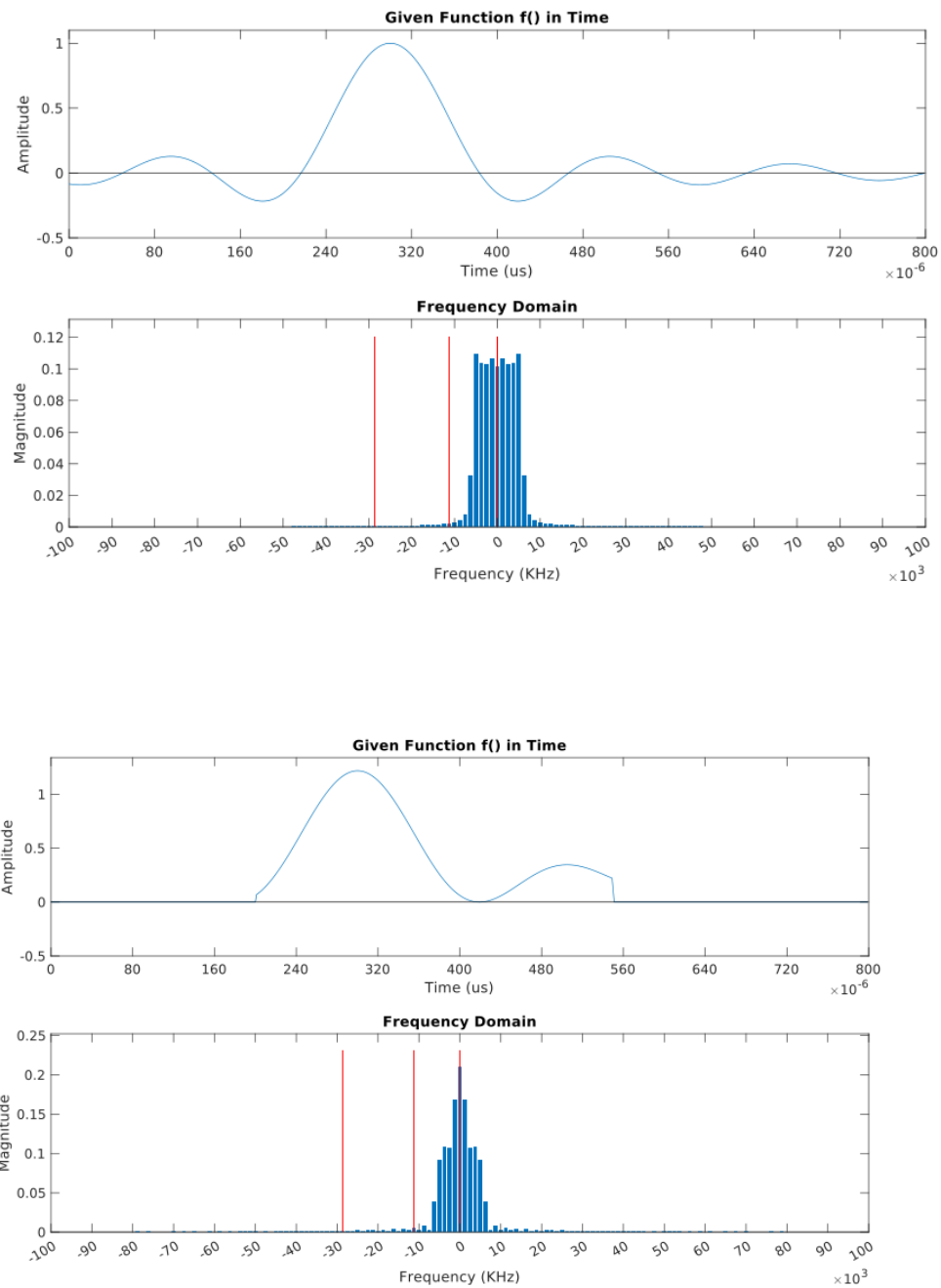


Figure 15 – In (a), the $\text{sinc}(t)$ function (with time $800 \mu\text{s}$), and its Fourier Transform below. In (b) the truncated $\text{sinc}(t)$ function (now $400 \mu\text{s}$), with limited time, the function was also lifted to avoid negative amplitudes. Red lines indicate the resonance frequencies of Qubits in the Trifluorine molecule, with the resonance in zero being the rightmost qubit, also labeled F1 in Figure 9. It is clear that its frequencies are mostly centered around the target frequency.

5.3 A mathematical detour on uncertainty and Fourier transforms

As the reader may have already noticed by examining Figure 14, when the function has long duration (large time-width) its Fourier Transform is narrow, and, thanks to

the duality property, when the transform has large frequency-width, the time function is narrow. This effect is known as the *Dilation Property*. Consider the following function

$$f_s(t) = \frac{1}{\sqrt{s}} f\left(\frac{t}{s}\right), \quad (5.3)$$

where $s \in \mathbb{R}^+$ controls the time-width of the function. Calculating its Fourier transform we have, using the variable change $u = x/s$

$$F_s(\omega) = \frac{1}{\sqrt{s}} \int_{-\infty}^{\infty} f\left(\frac{t}{s}\right) e^{-i\omega t} dt \quad (5.4)$$

$$= \frac{1}{\sqrt{s}} \int_{-\infty}^{\infty} f(u) e^{-i(\omega s)u} s du \quad (5.5)$$

$$= \sqrt{s} F(s\omega), \quad (5.6)$$

then

$$f_s(t) \cdot F_s(\omega) = f\left(\frac{t}{s}\right) \cdot F(s\omega). \quad (5.7)$$

Therefore, if f_s had $1/s$ in its argument, its Fourier transform F_s has s , so that when the width is constrained in one of the domains, in the other it is dilated.

The formal definitions for the Fourier Transform is of course more complicated than what was shown here. To be precise, the Fourier Transform can be stated as $\mathcal{F} : \mathcal{L}^1(\mathbb{R}) \rightarrow \mathcal{L}^1(\mathbb{R})$, i.e., its domain is the \mathcal{L}^1 space, the space of Lebesgue measurable functions under the $\|.\|_1$ norm. However, as $\mathcal{L}^1(\mathbb{R}) \cap \mathcal{L}^2(\mathbb{R})$ is dense in $\mathcal{L}^2(\mathbb{R})$, one can build a Cauchy sequence in $\mathcal{L}^1(\mathbb{R})$ that converges pointwise to any function in $\mathcal{L}^2(\mathbb{R})$, and then define a Fourier Transform to a function in $\mathcal{L}^2(\mathbb{R})$ as its nearest Fourier in the subset of the intersection. For further details, see Reference [20, p. 8].

That said, one can then use the $\|.\|^2$ norm to derive a particularly well known property, namely: the *uncertainty relation* of a function and its Fourier transform

$$\left(\int_{-\infty}^{\infty} t^2 |f(t)|^2 dt \right) \cdot \left(\int_{-\infty}^{\infty} \omega^2 |F(\omega)|^2 d\omega \right) \geq \frac{1}{16\pi^2}. \quad (5.8)$$

This expression can be generalized to complex Hilbert Spaces, and therefore to probability waves, leading to the famous *Heisenberg uncertainty relations* [20, p.10]

$$\Delta x \Delta p \geq \hbar/2, \quad \Delta E \Delta t \geq \hbar/2 \quad (5.9)$$

The discussion above is only a showcase to the fact that, when dealing with signals that have wave behavior, some limits to control are essential to the object at hand, and

not an artifact of experimental practice. Of course the RF signal discussed in the previous sections was presented as a classical (electromagnetic) wave, as opposed to the nuclear spin system whose wave behavior is very much quantum. Nonetheless it has insuperable uncertainties, as shown by the uncertainty relations. This mathematical detour is only a reminder of these properties and shall not be discussed further, as explaining such relations in a rigorous manner would require an introduction to the field of *functional analysis*, which is very much out of the scope of this work. The interested reader may refer to [17].

5.4 Modulating RF pulses through the GRAPE algorithm

In the context of qubit control within NMR systems, the significance of the GRAPE algorithm as a primary tool cannot be overstated. The name GRAPE stands for *Gradient Ascent Pulse Engineering* [30], a straightforward name, as it makes heavy use of the gradient ascent/descent algorithms that are ubiquitous to optimization problems in a broader sense. In this section I will try to make clear how it works and its assumptions.

One should remember that a quantum system, in the absence of relaxation, obeys the Liouville-von Neumann equation

$$\dot{\rho}(t) = -\frac{i}{\hbar} [\mathcal{H}(t), \rho(t)]. \quad (5.10)$$

Looking at Equation (3.4) one sees that the time dependence of the NMR Hamiltonian is separable in $\mathcal{H}_0 + \mathcal{H}_{RF}(t)$, where \mathcal{H}_0 is the time-independent free evolution part. A further hypothesis can be formulated: assume that the RF control part can be written in a sum of amplitudes $u_k(t)$ weighted by m Hamiltonians that are constant in time \mathcal{H}_k , so that

$$\mathcal{H}(t) = \mathcal{H}_0 + \sum_{k=1}^m u_k(t) \mathcal{H}_k \quad (5.11)$$

where $u(t) = (u_1(t), \dots, u_m(t))$ is called the *control fields vector*. One can state the problem as to find the best control fields vector as to maximize the loss function

$$\mathcal{L}(u_1, \dots, u_m) = \langle \sigma_c | \rho(T) \rangle = \text{tr}\{\sigma_c^\dagger \rho(T)\}, \quad (5.12)$$

where σ_c is the goal state, and T is the final time of the pulse application. As the overlap has an upper bound of 1, best amplitudes $\{u_k\}$ should give $\langle \sigma_c | \rho(T) \rangle \approx 1$.

Now, by discretizing time in N parts, i.e., $T/N = \Delta t$, as much as needed so that $u_k(t) \approx u_k(t_j)$ is constant for $t_j \in (t - \Delta t/2, t + \Delta t/2)$, then, time evolution will be given by

$$\begin{aligned} U_j(\Delta t) &= \exp \left[-i\Delta t \left(\mathcal{H}_0 + \sum_{k=1}^m u_k(t_j) \mathcal{H}_k \right) \right], \quad \text{and} \\ \rho(T) &= U_N \dots U_1 \rho_0 U_1^\dagger \dots U_N^\dagger. \end{aligned}$$

Now, by the cyclical property of the trace, the loss function can be written as

$$\langle \sigma_c | \rho(T) \rangle = \underbrace{\left\langle U_{j+1}^\dagger \dots U_N^\dagger \rho_c U_N \dots U_{j+1} \right|}_{\sigma_{c,N-j}} \underbrace{\left| U_j \dots U_1 \rho_0 U_1^\dagger \dots U_j^\dagger \right\rangle}_{\rho_j}$$

where, ρ_j is the state at time t_j and $\sigma_{c,N-j}$ is the backpropagated target state at the same time. One can show that the variation of δU_j relative to a variation $\delta u_k(j)$ is given by $\delta U_j = -i\delta u_k(j)\Delta t \tilde{\mathcal{H}}_k U_j$, where $\Delta t \tilde{\mathcal{H}}_k = \int_0^{\Delta t} U_j(\tau) H_k U_j(-\tau) d\tau$. Now, if Δt is sufficiently small, then $\tilde{\mathcal{H}}_k \approx H_k$, then one obtains the following expression

$$\frac{\delta \mathcal{L}(u_1, \dots, u_k)}{\delta u_k(j)} = -\langle \sigma_{c,N-j} | i\Delta t [\mathcal{H}_k, \rho_j] \rangle \quad (5.13)$$

which can be easily calculated for all k .

Now that we have an expression for the gradient of the loss function, we can adjust the $u_k(j)$ parameters by means of the gradient ascent rule

$$u_k(j) \rightarrow u_k(j) + r \frac{\delta \mathcal{L}(u_1, \dots, u_k)}{\delta u_k(j)} \quad (5.14)$$

where, r is called the *learning rate*. The bulge in the direction of the difference in $\delta \mathcal{L}(\vec{u})$ moves the k -th pulse amplitude in the direction that maximizes the loss function (the overlap), as shown by the arrows in the Figure 16.

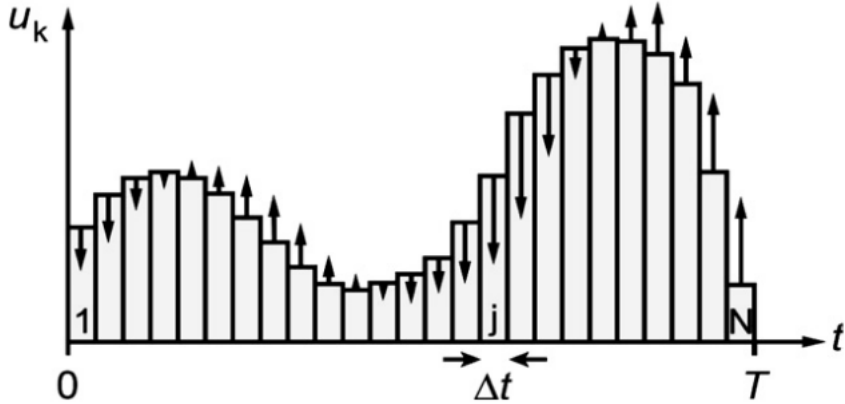


Figure 16 – Effect of one step of gradient ascent on the k -th amplitude element in the GRAPE algorithm. The amplitudes are described by blocks in a time partition. After each choice of parameters for the amplitudes $u_k(t)$ in the hamiltonian in Equation (5.11) and time partition, the height of each one of the blocks is adjusted following the Equation (5.14)

Since $\mathcal{L}(\vec{u})$ is differentiable, and assuming that its locally convex (which is a reasonable assumption near its global maximum $\mathcal{L}(\vec{u}) = 1$), then this algorithm is guaranteed to find a local maximum. However, as the domain of the loss function can become quite large, when the dimension of the control fields vector is large, the maximization of this function becomes a challenging task.

Moreover, even though the optimization is surely computationally feasible and finds a good set of amplitudes, it has some weaknesses. First, its loss function is state oriented, which means that for a different state a new pulse is needed (for both initial and final), and therefore a new optimization as well. This is, of course, a minor problem, since one may derive a similar algorithm where the loss function is measured by the unitary (i.e. the operation) instead of the state, but maintaining the rest of the algorithm unaltered. Secondly, it suffers from a subtle problem of pulse optimization: when the discretization is fine grained (i.e., large N), then it tends to optimize to pulses that have strong oscillations and are therefore experimentally unrealistic. This effect occurs as nothing is prohibitive of having $u_k(j)$ large, and then, for a small i , $u_k(j+i) \approx 0$. One must bear in mind that RFs have operational limitations to their modulations, i.e., maximum coarse graining is around 0.05 μ s in [28, p.234]. On the other hand, when the discretization is coarse grained (small N), the pulse becomes a stair function of large blocks, these are known as *strongly modulated pulses* (SMPs).

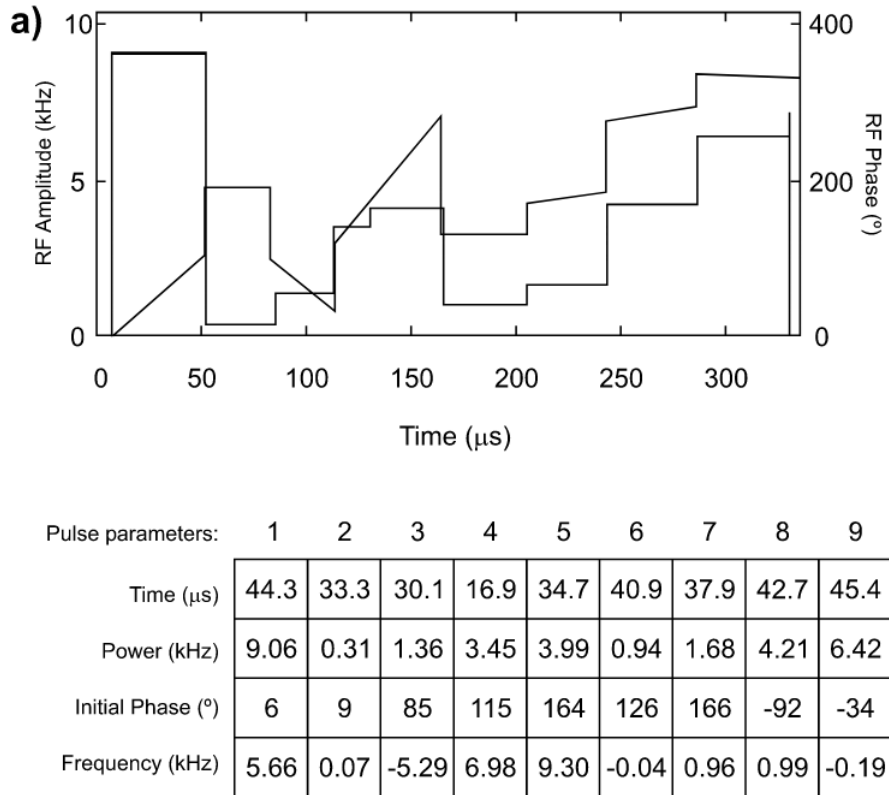


Figure 17 – GRAPE can result in strong modulated pulses. Strongly modulated pulses present sharp edges and long duration, figure from Reference [40], p. 152]. Both the amplitude and phase are plotted, and the table below shows their specific values in each of the 9 timesteps. This can cause discontinuities that are hard to be reproduced experimentally.

As one may notice from the observations in Figure 14, that squared pulses require long times to be really selective on frequencies, at least for homonuclear systems. This approach is also hampered by operational limitations, because the sharp edges from one block to the other are too challenging for usual equipment.

Chapter 6

Modulating RF pulses by Fourier Series

From the discussion of the last section, I hope to have made clear that an important problem of the GRAPE algorithm approach is that the resulting RF pulse has sharp edges and/or strong discontinuities. This is a common issue to the conversion of digital to analog signals. In our case, the analog signal is an oscillation in a RF probe, i.e., an oscillating electric current, while the digital signal given, is discrete by nature. So when a signal as a square is given as an input, its output will not be, strictly speaking, a square, it will actually be an oscillatory (a.k.a. a Fourier Series) approximation to a square function. This is an instance of the famous *Gibbs Phenomenon*, which will be further explored below.

6.1 Fourier Series and discontinuous functions

The *Fourier Series* of a function $f : \mathbb{C} \rightarrow \mathbb{C}$ is given by

$$S(z) = \sum_{n=-\infty}^{+\infty} c_n e^{\frac{2\pi i n z}{T}}, \quad \text{where } T \text{ is the period of } f \text{ and} \quad (6.1)$$

$$c_n = \frac{1}{T} \int_{-T/2}^{T/2} f(z) e^{-\frac{2\pi i n z}{T}} dz \quad \forall n \in \mathbb{Z}. \quad (6.2)$$

In sight of the previous section, one may notice that c_n is the Fourier transform of $f(z)$ calculated at the point $\omega = 2\pi n/T$. In the case of this work, we will work with Fourier series that are strictly on the real line, and can therefore take the real part of the series to obtain an expression in terms of the cosines and a phase φ_n . By projection on the domain on \mathbb{R} we have the Fourier series for $f : \mathbb{R} \rightarrow \mathbb{R}$ as

$$S(t) = \sum_{n=0}^{\infty} A_n \cos\left(2\pi \frac{n}{T} t + \varphi_n\right), \quad \text{where } T \text{ is the period of } f \text{ and} \quad (6.3)$$

$$A_n = \frac{2}{T} \int_{-T/2}^{T/2} f(t) \cos\left(2\pi \frac{n}{T} t + \varphi_n\right) dt \quad \forall n \in \mathbb{N}. \quad (6.4)$$

The study of Fourier series is part of undergraduate Physics all around the world, therefore we will not explore all the details of these series here, but some properties ought to be reminded before proceeding.

Fourier series are very commonly used to approximate continuous periodic functions. In mathematical terminology one says that if a function $f \in \mathcal{C}^1([-T/2, T/2])$ (the space of continuous functions in this interval of \mathbb{R}), then its Fourier series S converges uniformly to f , i.e., $\forall \varepsilon > 0$ there exists a large $N \in \mathbb{N}$ such that, if $m > N$, then $\forall t \in [-T/2, T/2]$ we have $|f(t) - S_m(t)| < \varepsilon$. Where S_m is the truncated sum of S . Uniform convergence is an expected property of Fourier Series, as these make a complete basis of $\mathcal{C}^1(\mathbb{R})$. This property is, however, lost for discontinuous functions.

Lets us study the square function as a counter example. Suppose a square function $f(t) = \Theta(t + T_1) - \Theta(t - T_1)$ as in Figure 13, non-zero between $-T_1$ and T_1 , with height 1. In this case, given its Fourier Series $S(t)$, for all $t \in (-T_1, T_1)$ the convergence is uniform, as the function is continuous in this interval. However, exactly at $t = \pm T_1$ we have $f(\pm T_1) = 1$ and $S(\pm T_1) = 1/2$, as the value at discontinuities of a Fourier series is

$$S(\pm T_1) = \lim_{\varepsilon \rightarrow 0} \frac{f(\pm T_1 + \varepsilon) + f(\pm T_1 - \varepsilon)}{2} = \frac{1}{2}, \quad (6.5)$$

i.e., the average of the neighboring points. This is, arguably, an unexpected property, since the function converges in the $\|.\|_1$ norm. That is,

$$\int_{-T}^T |f(t) - S(t)| dt = 0.$$

a consequence of the known property of Riemann integrals that the value of the integral is unchanged if a finite number of points are removed.

This means that a digital signal of a discontinuous function will be experimentally produced as a continuous approximation of this signal, and may give residual effects that are only sensible when dealing with the limits of our experimental set up. This is the case in NMR control, as the pulses have maximal precision of 0.05 μs [28, p.234], and therefore the apparatus may not be able to reliably produce signals that have strong modulations in a interval that is smaller than this. One should bear in mind that the instrument will produce a signal, but probably not the (intended) signal. Other limitations of this approach will be explored below.

6.1.1 The Gibbs Phenomenon

Another known effect of the digital to analog signal conversion occurs when the input function is not oscillatory, but the output is. As discussed above, in the infinite series case, the convergence is uniform outside of the discontinuity, and even there it is the average of the neighboring points. However, true signals are not a series of infinite terms, as digital information is stored in a finite number of bits.

Let us dwell some more on the square function example. In the case of the finite Fourier series, there are not enough summing terms to completely eliminate the oscillations of the output function, and as more terms are added with higher frequencies the oscillations become stronger at the discontinuities, see Figure 18, this produces an overshoot near $t = \pm T_1$. However, this overshoot is bounded, and it can be shown that it is around 9% of the length of the discontinuity¹ [41, p.200] (in this case equal to 1). This 9% difference is always present for finite series sum, and it is a constant. The value is independent of the cutoff of the partial sum N , as it can always be calculated as (see also Appendix A)

$$\left|1 - S_N\left(T_1 + \frac{2T_1}{N}\right)\right| = 0.089489872236\dots, \quad \forall \text{ finite } N \in \mathbb{N}. \quad (6.6)$$

One can check this value numerically by calculating for the case of the square function by using the expression for its partial sum in Equation (A.1). This value is called the *Wilbraham-Gibbs Constant*. As seen on items (c) and (d) of Figure 18, the overshoot is not eliminated when more terms are added, it is only squeezed in the direction of the discontinuity. Nevertheless, when the sum has infinitely many terms the series must converge to the value $S(T_1) = 1/2$, and $S(T_1^+) = 1$ and $S(T_1^-) = 0$, this means that the overshoot is eliminated only when infinite terms are added, as the length $2T_1/N \rightarrow 0$ when $N \rightarrow \infty$.

As the electronic used in NMR systems is digital, the conversion will naturally suffer from this effect (sometimes referred as *ringing* of the signal).

As a historical note [13, 26, p.420, p.147], this effect is commonly credited to the Nobel laureate Albert Michelson, famously known for his work with interferometers. Michelson also built mechanical machines to produce trigonometric series up to 80 terms around 1898, however the machine was not accurate enough to show the Gibbs phenomenon. A paper by Michelson was the original cause of interest for Gibbs, who wrote

¹ To the best of my knowledge, the consulted texts on signal processing do not show the calculations for this overshoot. And as I have not found an example in the literature that did not make use of a somewhat cumbersome (but not wrong) approximation of the integral of the sinc() function, I calculated for the square function example the exact point where the series maximum is found, and one can check that, at this point, it is given by the Wilbraham-Gibbs Constant. However, writing it in the corpus of the text would not add much to the point. I left it therefore as an Appendix, as it may be of the interest of future students.

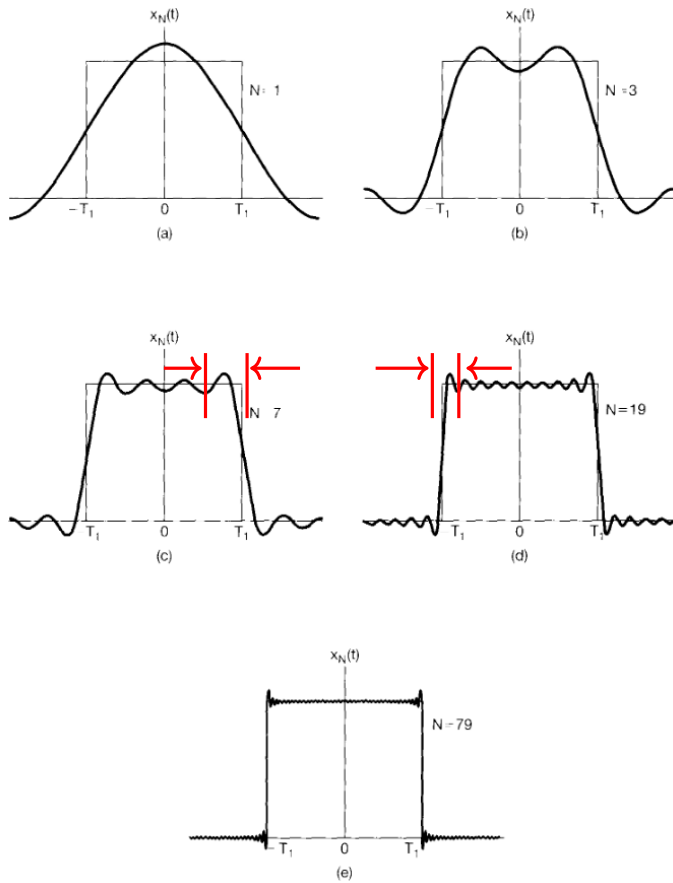


Figure 18 – Gibbs Phenomenon plotted for each N terms of the finite series [41, p.201].

Whenever one represents a discontinuous function by a finite term Fourier series, it is inevitable that the approximation overshoots the target function value at the discontinuities. The squeezing of the overshoot is shown in red in items (c) and (d). However, this effect does not occur when there are infinite terms to the series, as the squeezing of the overshoot converges to zero length.

a letter to the Nature journal on the matter, but gave no formal proof². The thorough treatment of this matter would only be made by Böcher seven years later, who coined the term “Gibbs Phenomenon”.

6.2 Bypassing digital to analog conversion

Prior to this section, we have mostly discussed the limitations of control methods when applied to the laboratory practice. Although the GRAPE method is very much reliable, analytically, I hope to have made sufficiently clear that some of its problems

² Many important historical names took part in the comings and goings in the discussion of whether the effect was real or only technical. In the midst of all the letters and erratas, there is a humbling piece of text of a wrongly calculated integral of the sinc() function by the great mathematician Henri Poincaré in the Nature discussion. This nugget of history is a healthy reminder that *quandoque bonus dormitat Homero.*

are hard to manage in true experimental setups. Now that our main problem is properly contextualized, we will discuss the main proposal of this work through this section.

Since most issues arise with discontinuities, and as the RF output pulse must be an oscillating function, a natural conclusion would be to bypass some of the digital to analog conversion by optimizing Fourier Series directly. This is the proposal of Reference [44], on which this section is strongly based.

In the following we will work only in the case of the homonuclear system. The heteronuclear and mixed case are similar, but because the effects we wish to analyze are separable by the RWA approximation when more RF signals are available, as shown in Section 3.3, we will not discuss them thoroughly. Remember the RF Hamiltonian in Equation (3.19), prior to choosing the frequency, i.e., with $\Delta\omega_{j,RF} = \omega_j - \omega_{RF}$, where ω_j and ω_{RF} are the rotating frame and RF frequency respectively, has the form

$$\mathcal{H}_{RF}(t) = \frac{\hbar\gamma}{2}\Omega(t)\sum_{k=1}^N \left[\sigma_x^{(k)} \cos(\Delta\omega_{j,RF} \cdot t + \phi(t)) + \sigma_y^{(k)} \sin(\Delta\omega_{j,RF} \cdot t + \phi(t)) \right]. \quad (6.7)$$

In this expression, the amplitude $\Omega(t)$ and phase $\phi(t)$ are experimentally controllable, and can be expressed as Fourier Series

$$\begin{aligned} \Omega(t) &= \sum_{m=1}^{s_A} a_m \sin(b_m t + c_m) \\ \phi(t) &= \sum_{m'=1}^{s_P} d_{m'} \sin(f_{m'} t + g_{m'}), \end{aligned}$$

we are interested in optimizing the coefficients $\{a_m, b_m, c_m, d_{m'}, f_{m'}, g_{m'}\} \subseteq \mathbb{R}$, such that control is maximized. In the same fashion of the GRAPE algorithm, we need to build a loss function to measure the evolution of the optimization. In the Reference [44, p.2] the authors suggest the use of

$$\mathcal{F} = 1 - \frac{|tr(U_t^\dagger U_g)|}{N}, \quad (6.8)$$

as a loss function, where t stands for ‘target’, and g for ‘generated’ unitary, while N is the number of qubits in the system. However we chose a different loss function, but with similar properties, given by

$$\chi^2(U_t, U_g) = \sum_{i,j=1}^{2^N} Re([U_t]_{i,j} - [U_g]_{i,j}) + Im([U_t]_{i,j} - [U_g]_{i,j}) + \theta([U_t - U_g]_{1,1}), \quad (6.9)$$

i.e., the sum of all the elements of the real and imaginary difference between the target and generated unitaries. The $\theta()$ function here is an optional element, it takes angular

difference between the $U_{1,1}$ element of each matrix, to guarantee that there will not be a global phase between the optimized and target unitary. Nevertheless, this restriction can be lifted, and will be ignored for the rest of this work, setting $\theta = 0$ in the loss function. The choice of a different loss function is due to the fact that both \mathcal{F} and χ^2 are both good measures of how good the approximation is, but as far as our simulations went, it always returned values

$$\mathcal{F}(U_t, U_g) \approx \chi^2(U_t, U_g) \cdot 10^{-2}.$$

We chose χ^2 because it gave larger values, and therefore made the bad approximations more obvious.

Also the authors of [44] made use of a well known derivative-less optimization method called *Nelder-Mead*. As both this optimizer and the gradient descent (used in GRAPE) were easily available in Matlab, through the use of the ‘*fmincon*’ and ‘*fminsearch*’ built-in functions, and we saw no significant difference in the local minima that each one regularly found, nor the computational time spent, we decided to use the *fmincon* for most of our optimizations for comparison purposes.

Another restriction has to be made to set the amplitude to zero in the pulse times $t = 0$ and $t = \tau_f$, as the pulse has to start at amplitude zero, because the RF probe is always at rest. To assure this, the amplitude is bounded near the initial and final values by

$$\Omega(t) \rightarrow -\tanh\left(\frac{\zeta_1 t}{\tau_f}\right) \tanh\left(\frac{\zeta_2(t - \tau_f)}{\tau_f}\right) \Omega(t) \quad (6.10)$$

where $\zeta_1, \zeta_2 = 2$ are chosen ad. hoc., as these worked well experimentally but should be chosen according to each experimental setup and the specific time response of the RF generator. Moreover, $\Omega(t)$ must be bounded by the maximum amplitude of the RF, which is determined by using the squared pulse as standard during usual calibration. That is, before a battery of experiments, as conditions may differ ³, it is a necessary experimental practice to calibrate the power and pulse time of a π rotation pulse. When this is done, one can set this specific power as the numerical standard and optimize with this bound, making the experimental preparations for the modulated pulses the same as the usual for quantum information processing in NMR. These two restrictions, bounded amplitude and bounded derivative near the time boundaries, are not necessary for the phase modulation, because the initial time of the phase $\phi(t = 0)$ is equal to the relative phase between the RF oscillation and the nuclear spin oscillation (in its Larmor frequency), it can therefore be any value in $\phi(0) \in [0, 2\pi]$.

Now the problem can be stated as: Given a target unitary U_t an initial set of coefficients for amplitude, phase and frequency of a Fourier series, $\{a_m, b_m, c_m\} = C_A$,

³ These may be given by: the level of liquid Nitrogen in the NMR machine; the molecule sample quality; the shimming of to constant fields B_0 ; etc

$\{d_{m'}, f_{m'}, g_{m'}\} = C_P \subseteq \mathbb{R}$, where $m \in \{1, \dots, s_A\}$ and $m' \in \{1, \dots, s_P\}$, where $s_A, s_P \in \mathbb{N}$ are the partial sum bound of the Fourier Series for the amplitude $\Omega(t)$ and phase $\phi(t)$ of the RF Hamiltonian given by Equation (6.7), find the best coefficients set such that,

$$\min_{\substack{\{a_m, b_m, c_m\} \in C_A, \\ \{d_{m'}, f_{m'}, g_{m'}\} \in C_P}} \left\{ \chi^2(U_t, U_g) \right\}, \quad \text{where} \quad (6.11)$$

$$U_g = \mathcal{T} \left\{ \exp \left[-\frac{it}{\hbar} \mathcal{H}_0 - \frac{it}{\hbar} \int_{t_0}^{\tau_f} \mathcal{H}_{RF}(t) dt \right] \right\}, \quad (6.12)$$

and where \mathcal{T} is the time-ordering operator and $\mathcal{H}_0 = \mathcal{H}_{Zee} + \mathcal{H}_{int}$.

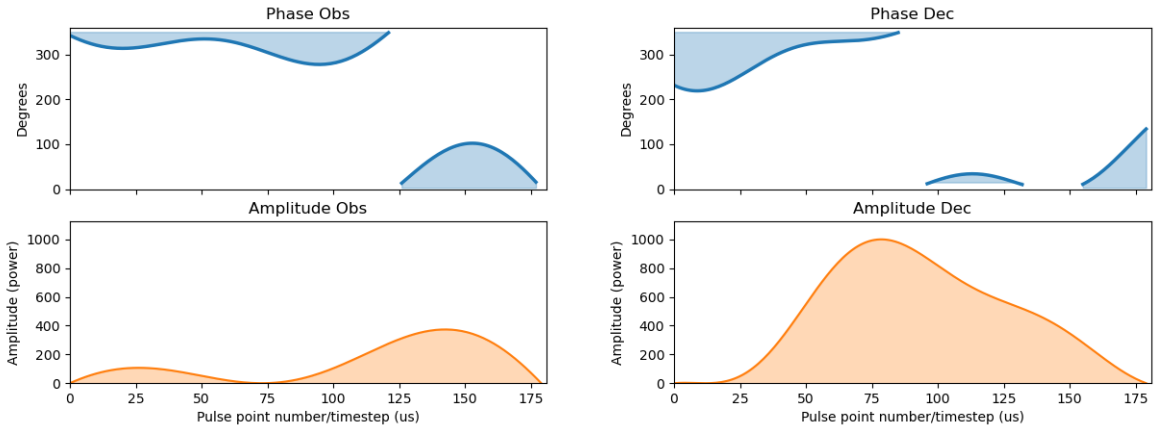


Figure 19 – Example of a optimized pulse in the observer and decoupler channel for a $Rot_x(\pi) \otimes Rot_x(\pi)$ gate. Upper graph is the phase plotted as $\phi(t) \bmod 360$ as the phase is the same under a 360 rotation, the lower plot is the amplitude (up to 1024, a digit representing 100% of the RF power). The x axis reads in number of points given to the rf generator, the actual machine precision limit is a 1 to 1 ration for point to us, in this figure the timestep is $dt = 190/180$, i.e. 180 points for 190 μ s.

Once the best unitary U_g is found, and by the expression of χ^2 it is element by element near U_t , it should be a straightforward consequence that

$$\rho(\tau_f) = U_g \rho_0 U_g^\dagger = U_t \rho_0 U_t^\dagger,$$

i.e., by finding the best unitary it should give the same final state. This is fundamentally different from the GRAPE as described above, by optimizing on the unitary, the present method is more general and not state-dependent. Furthermore, the GRAPE method is known to have many parameters $u_k(t)$ [44, p.3] that vary in time, while in the Fourier based method we found that s_A between 1 and 7 and $s_P = 14$ gave satisfactory results, and, since there are 3 coefficients for each, we have between 45 and 63 parameters that are independent of pulse time length, for each RF channel. For this reason the smooth

Fourier series based method optimization is faster than GRAPE, as the dimension of the parameter space is greatly reduced.

6.3 Numerical Results

6.3.1 Initial value dependency

Some nuances have to be discussed prior to showing the obtained results. Optimization methods in positive semi-definite programming, are very much sensitive to initial conditions. When many parameters are considered, and local minima abound, it is very much probable that the optimization will find a minimum and stop near it without exploring more of the parameter landscape, as the optimization step may not be large enough to overstep high differences in function evaluations.

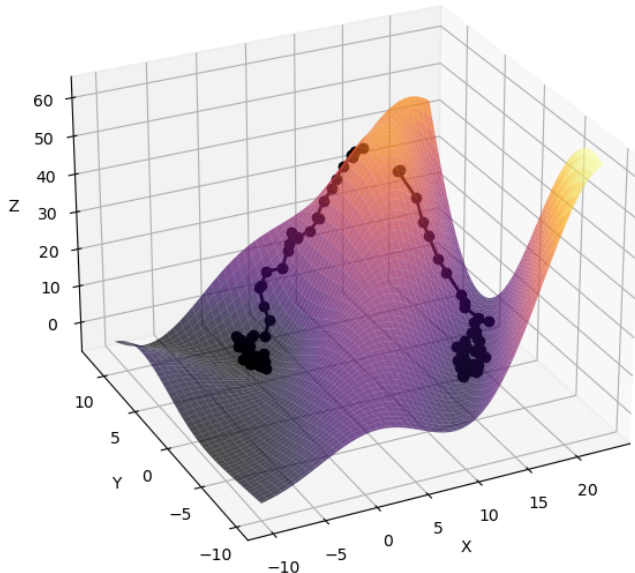


Figure 20 – Example of Stochastic Gradient Descent with two different initial values, this image is merely pictorial, as the actual optimization utilizes 63 parameters and not 2. Z represents the loss function value, and X, Y two possible parameters. In black is the optimization path. The image shows that two different choices of initial values may lead to final optimizations minima that are substantially different. One optimization path may lead to a lower minimum than the other, and the optimization may be stuck in large minima as the optimization steps may not be large enough to escape the loss function parameter valley.

There are many ways to deal with these issues, some are specific to the optimization

method at hand, and others are more general, but either way it demands to have some prior knowledge of your system and then restrict the possible approaches accordingly.

As one of the properties we wish to have in our pulses is that they are sufficiently smooth as to avoid surpassing the experimental electronic signal processing limitations of our equipment, we have chosen to set the initial values of the parameters near Fourier coefficients that have small frequencies (i.e., small $\{b_m\}$ and $\{f_{m'}\}$), because we observed that, when initial values are totally random, the optimization may be stuck in a region of the parameter space that oscillates too rapidly. This happens because, in theory, rapid oscillations may find very low values for the loss function χ^2 , and approximate very well the target unitary, but as stated in the previous section, these are not good pulses, experimentally. Moreover, as Fourier Series usually have dominating frequencies, the optimization usually gave a large value for one of the m or m' amplitudes ($\{a_m\}, \{d_{m'}\}$), and fast diminishing values for the other series amplitude parameters. To diminish the amount of runs, we chose to give the amplitudes values weighted by $1/\sqrt{m}$. The phase coefficients ($\{c_m\}, \{g_{m'}\}$) are chosen randomly between $[0, 360)$ degrees, but no further restrictions were made, as these only control the initial value of the sine curves. The following pseudocode explicits the initial value decision, but many other choices are available

Algorithm 1 Fourier series coefficients initialization

```

1: Input values  $s_A, s_P$ 
2: for  $m \in \{1, \dots, s_A\}$  do
3:    $a_m = (1/8 + 7/8 \cdot \text{rand}(1)) \cdot 10^2 / \sqrt{m}$ 
4:    $b_m = (1/8 + 7/8 \cdot \text{rand}(1)) \cdot 10^{-1}$ 
5:    $c_m = \text{rand}(1) \cdot 360$ 
6: end for
7: for  $m' \in \{1, \dots, s_P\}$  do
8:    $d_{m'} = (1/8 + 7/8 \cdot \text{rand}(1)) \cdot 10^2 / \sqrt{m'}$ 
9:    $f_{m'} = (1/8 + 7/8 \cdot \text{rand}(1)) \cdot 10^{-1}$ 
10:   $g_{m'} = \text{rand}(1) \cdot 360$ 
11: end for

```

where $\text{rand}(1) \in [0, 1)$ is a random number given by a normal distribution, we also chose the coefficient values to avoid being zero, as this can lead to unstable optimizations. By giving educated guesses as initial conditions the amount of independent times the optimization is run is reduced.

Now, two main initial value techniques were used. The first was to select a random initialization, as described by the pseudocode above, each time the optimization is run. The second technique is to use the Matlab built-in function *Multistart()*, in this case the randomly selected initial values are given as a upper bound (and their mirror image around zero as lowerbound, whenever possible), to the optimization, and the built-in

function creates a point grid of P values in parameter space between the two bounds. This means that, for each run of the pseudocode above, the optimization is run P times. On the other hand in the first method each initial value is randomly drafted (lets say P times for comparison purposes) and then run.

By setting $P = 200$ we noted that the methods are equivalent in the homonuclear case, but the results differ in the heteronuclear case, as shown in Figure 21. In this case, it was even worse to optimize the pulse than to not optimize (see panel (a) in the Figure 21), as the black line in the graph represents the usual not optimized pulse as a comparison, and the optimized pulses are about 10 times worse. Of course the comparison in heteronuclear molecules is not a good one, as the results in the previous section we have shown that the use of RWA approximations make the qubits independently controllable, and therefore non optimized gates are already very much reliable. Nonetheless, when running the first technique, results had an increase of one order of magnitude as seen in panel (b) in Figure 21.

Surely for the final optimization one should choose the optimization that gives the best fidelity. As the first technique covers a larger span of the parameter value, it is expected that it will be the one to find the best minimum, as the second method may be too restrictive on the search bounds. Why the effect does not occur in homonuclear systems is unclear, I suspect that these have less (or shallower) local minima, because changing the parameters just a little may change the final unitary by a large amount, as the pulse affects all qubits simultaneously (but not resonantly), and therefore the optimizer walks around the parameter space without being trapped by a bad (i.e. not global) minimum. This effect may play in favor of the optimization in homonuclear systems, showing that more complex systems may have unexpected desirable properties.

Regardless of the final values, as both methods are fully parallelizable, since the code may be written as to give each CPU a different initial value and then run independently, they are equivalent in matters of computational time. As stated, homonuclear system data (such as the Trifluorine molecule data) gave indistinguishable results, in this case the choice of technique is only restricted by convenience.

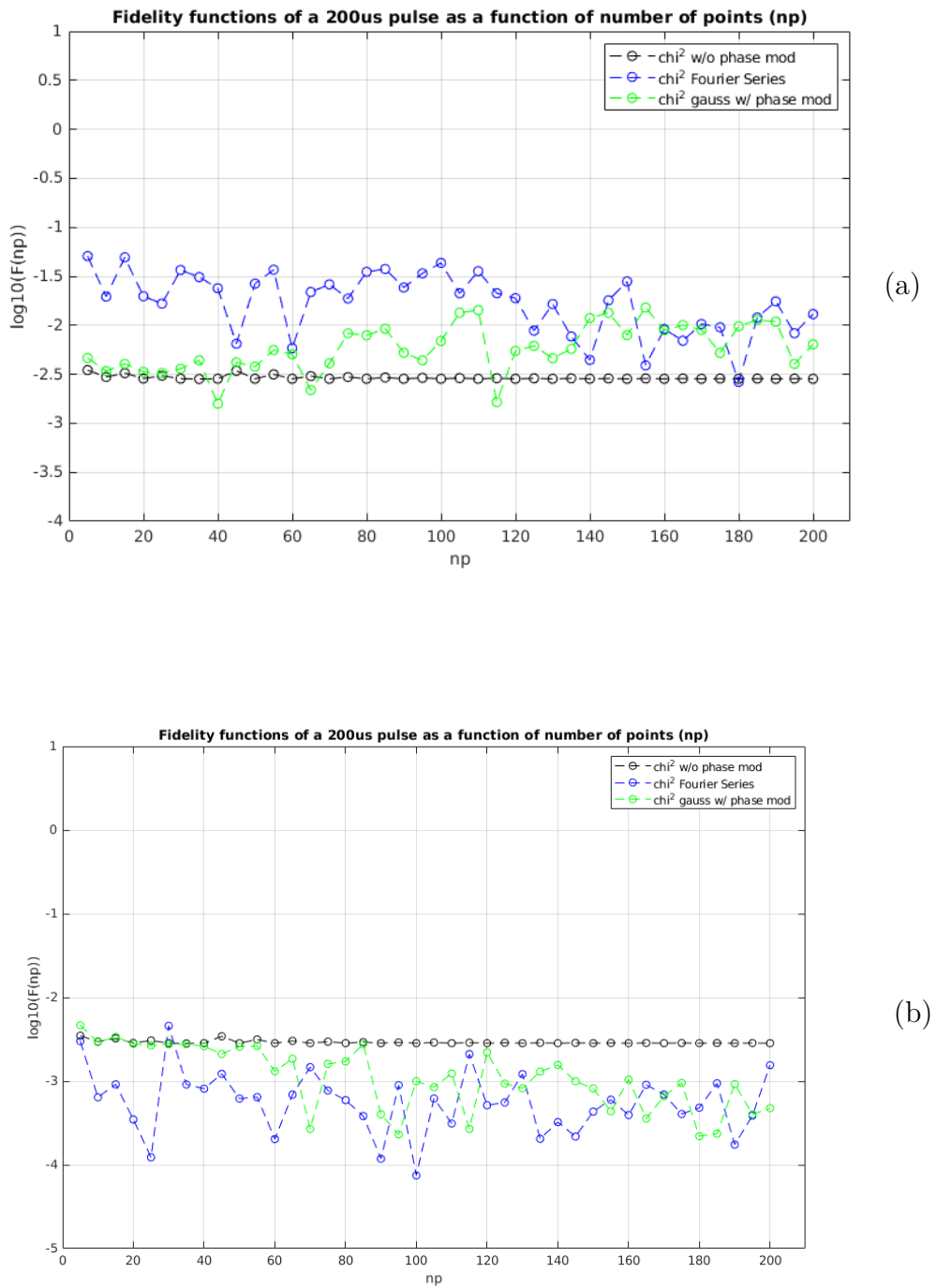


Figure 21 – Three modulations of a $\mathbb{I} \otimes Rot_x(\pi)$ gate are tested with the data of a Sodium Formate molecule (heteronuclear), and their χ^2 value is plotted in the y direction in a $\log(10)$ scale. The number of points np is given on the x axis. The maximum value of np is the time of the pulse 200 in units of μs . In black the amplitude is given by a gaussian modulation with a fixed phase (i.e. a non-optimalizable reference pulse), in green the amplitude is still a gaussian modulation but phase is given by a Fourier series, and in blue both amplitude and phase are Fourier series, more on the pulse types in Figure 22. As stated in the text, the graph in (a) gives the optimization using the MatLab built-in `MultiStart()` function, giving bad results, while in (b) the “one run, one initial value” is shown to give better optimizations.

6.3.2 Modulation comparisons: the effect of \mathcal{H}_{int} in homonuclear systems

In the following we will compare three tests: 1) A control test, i.e., a Gaussian amplitude modulation with a fixed phase. 2) a Gaussian as the amplitude and the phase described by a Fourier series. 3) A pulse fully modulated by Fourier series. The choice of the Gaussian is a common choice for control in homonuclear systems, given that the Fourier transform is also a Gaussian which can be easily localized by controlling the width and pulse time, being therefore a selective pulse.

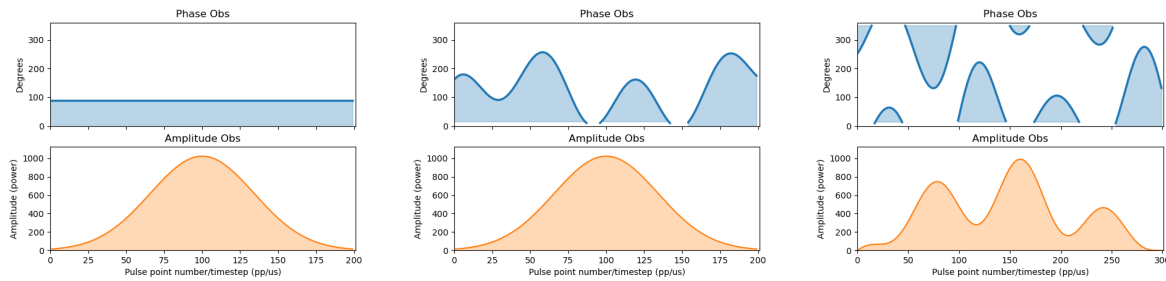


Figure 22 – Three type of pulses (Amplitude plotted in orange and phase in blue): 1) Gaussian modulation with fixed phase; 2) Gaussian with Fourier series phase; 3) full Fourier series modulation.

Once again we compared the loss functions χ^2 for the three pulses, as done in Figure 21, but this time with the data of homonuclear 3 qubit system (in our case we have used the Trifluorine data, i.e., the molecule in Figure 9), generating one 200 μs pulse that produces a $\mathbb{I} \otimes \text{Rot}_x(\pi) \otimes \mathbb{I}$ gate. This means that a single pulse is felt by the three qubits, but is in resonance with the middle one, in frequency terms. As stated before, the other two qubits are still affected by the pulse but in an off-resonance manner, however the optimization corrects for this effect. We measured the value of 200 initializations for each value of np sample points and plotted the best result of each batch in Figure 23.

Comparing the black dots in the plot of Figure 23 with Figure 21, one sees that the Gaussian pulses have a performance about 100 times worse in homonuclear systems. This worsening is an example of how homonuclear systems are harder to control and more nuanced than the heteronuclear ones. On the other hand, from 100 points onward, the modulated pulses are about two orders of magnitude better than the simple Gaussian. It is expected that pulses with a small number of sample points, np , will perform badly, as this number determines the number of data points given to the RF generator at each $dt = 200 \mu\text{s}/np$, and therefore become very irregular. Of course, this number has a higher bound given by the NMR machine precision of $dt = 0.05 \mu\text{s}$, i.e., 20 points for each microsecond [28, p.234]. But when $np \geq 140$ both modulations stabilize near $\log_{10}(\chi^2) = -1.5$, indicating that the optimization has reached a limit, and gives no enhancement by adding more sample points. As adding more points expands the optimization time, it may be desirable to keep it at a value of 3/4 of the total time when

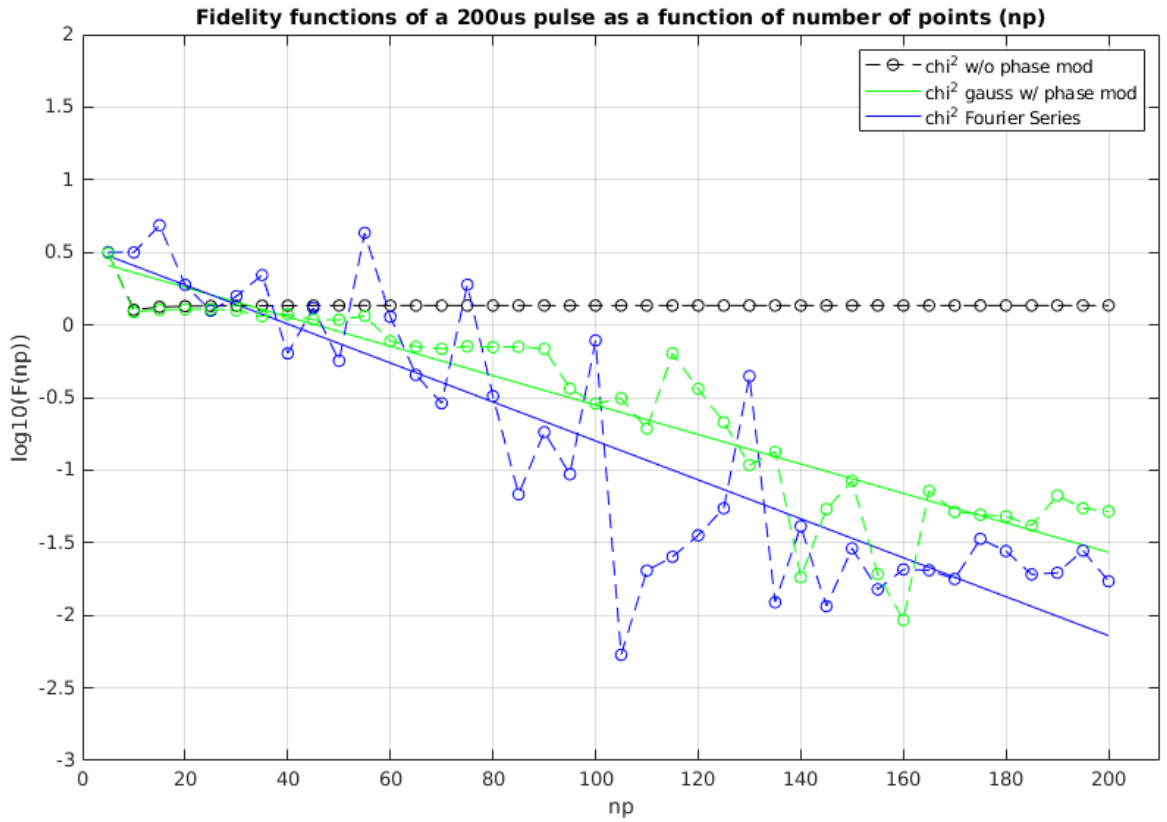


Figure 23 – Plot of $\log_{10}(\chi^2)$, where $\chi^2(U_t, U_g)$ is the Unitary loss function between the target unitary U_t and the generated one U_g , but plotted as a function of coarse graining np for 200 μs pulses of a $\mathbb{I} \otimes \text{Rot}_y(\pi)$ gate. For the same pulse types as in 22: Black dots are pulse type (1), green (2) and blue (3). The lines are the linear regressions, showing that the fully modulated pulses become better faster as a function of np in comparison with the phase modulated Gaussian.

testing.

Still, the issue of qubit control involves more than just the selection of frequency. Even though we have not discussed in detail the effects of the interacting hamiltonian, as the previous sections framed the problem mainly to Fourier transforms, it plays a major role in quantum information processing for protocols with longer duration, such as state preparation and control gates implementations. Since the control pulses have to be quite time consuming, the effects of the coupling become more relevant.

The $\frac{J}{2}\sigma_z^{(i)}\sigma_z^{(k)}$ elements in the hamiltonian of Equation (3.19) are responsible for the transfer of information from one qubit to another in the same molecule, given by the non-diagonal elements of the state matrix, and have an specific frequency equal to J . For the chloroform (heteronuclear) this frequency is around 215.1 Hz, while for the trifluorine (homonuclear) it has the value of $J_{i,j} = 128.1 \text{ Hz}, 47.65 \text{ Hz}, 69.86 \text{ Hz}$, for $(i,j) = (1,2), (1,3), (2,3)$. Therefore, our systems have usually the J -coupling from 10

to 100 Hz.

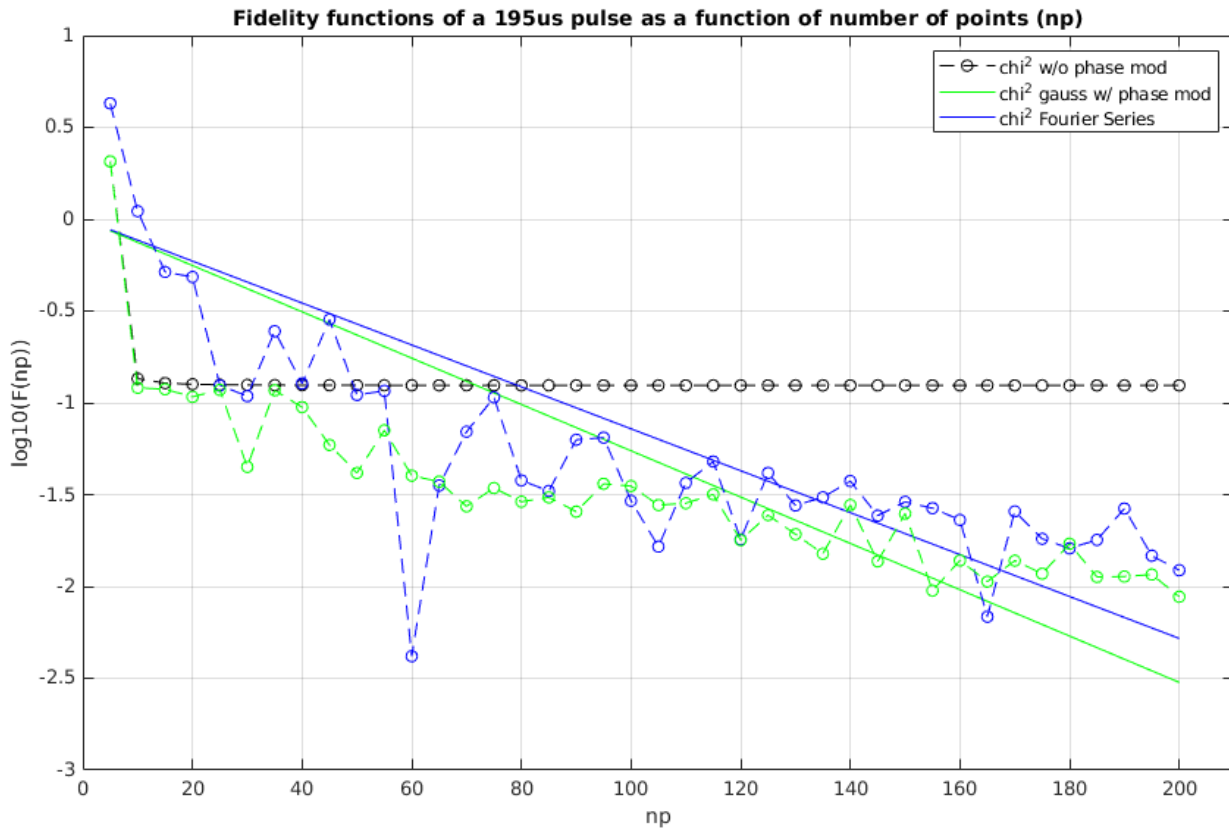


Figure 24 – Plot of $\log_{10}(\chi^2(U_t, U_g))$ as a function of np for three types of pulses in a period that is favourable for the usual Gaussian pulse (in black), Gaussian with modulated phase (green), and fully modulated by Fourier series (blue). Same notation as in Figure 23 is used.

Usual interaction time is expressed as multiples of $T_{int} = 1/J$, so that, in this case $T_{int} = 4.65$ ms for the chloroform and $T_{int} = 15$ ms for the weakest interaction in the trifluorine molecule. This interaction time is necessary for entangling gates, but since the decoherence time in NMR systems is between 2 to 4 seconds, the use of such gates is limited. T_{int} is of course larger than the 200 μ s of the pulses time scale, but as the pulse time increases its effects become more and more relevant. Some care is necessary with large fractions of this period. In Figure 23 the specific pulse time is unfavourable for the Gaussian pulse without phase modulation. Running the same protocol in the same Trifluorine molecule for 195 μ s (see Figure 24) shows that this specific time fractions are favorable for the fixed phase Gaussian pulses, as these have gained an order of magnitude (in term of the loss function value χ^2), but that, nonetheless, the modulated pulses are still robust and perform better than usual pulses. Additionally, this time the Gaussian pulse with phase modulation performs slightly better than the fully modulated pulse in this regime.

These plots show that modulated pulses offer a significant advantage in homonuclear systems, as the optimization not only selects the resonance frequency in a way that non-modulated pulses cannot, but that it also accounts for the interaction hamiltonian during the Fourier coefficient optimization. It should be noted that even if a dirac-delta, pulse in terms of frequency $\delta(\omega)$, was possible, the interacting hamiltonian would surely produce undesired effects and one would find that the resulting gate was not the intended one, as the neighboring qubits are also evolving and interacting at all times.

By looking at our choice of loss function χ^2 it is a remarkable property that it only takes into account the unitary U_g in the specific times t_0 and t_f , and is agnostic to the choice of path in the Bloch sphere that takes the qubits to the final state. These paths may be highly non-trivial, but the final state is guaranteed to be the target one.

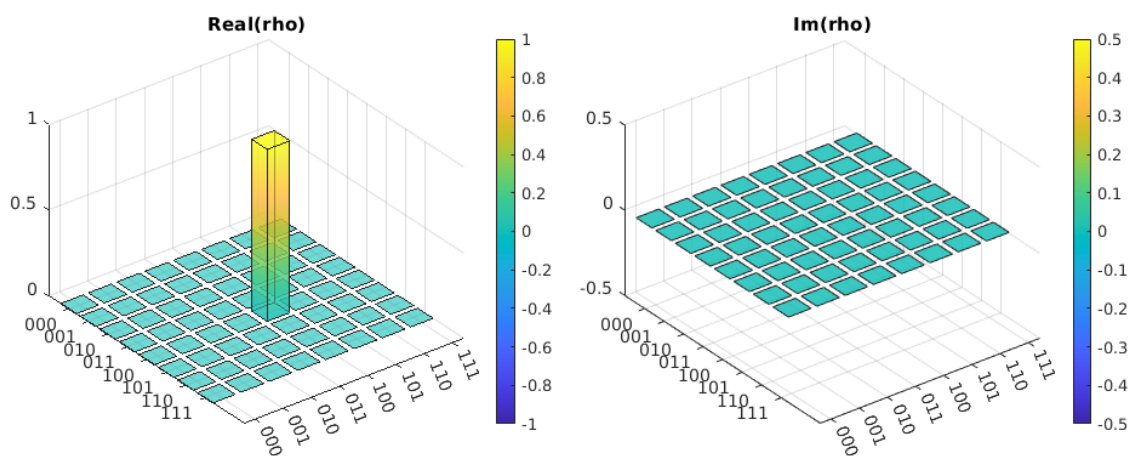


Figure 25 – Initial state of a homonuclear system, the density matrix is plotted and populations are represented by 3D bars. Real and Imaginary parts of the initial state $\rho(t_0)$, state is completely 100 (in the computational basis).

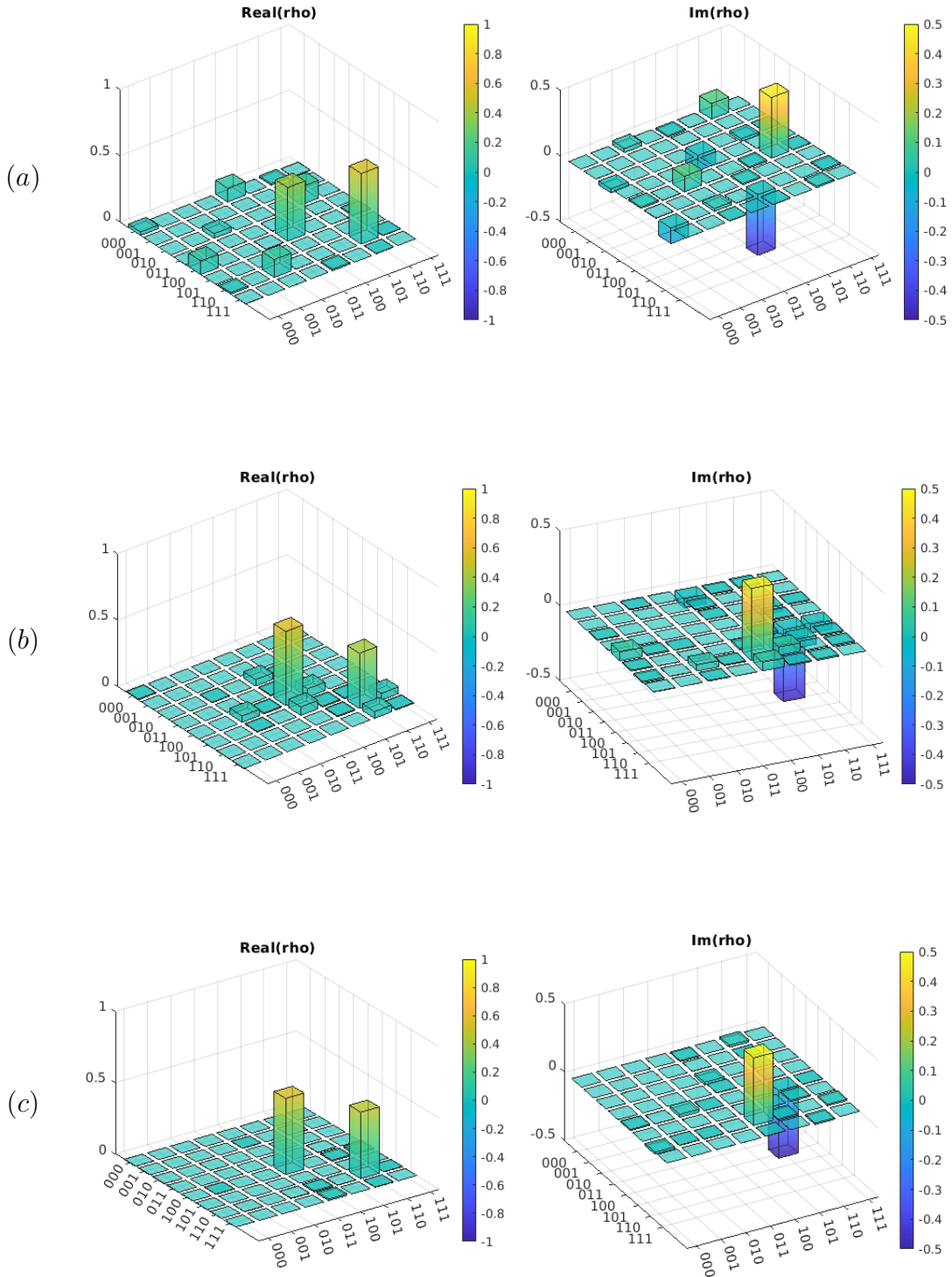


Figure 26 – Real and imaginary parts of $\rho(t_f)$ for (a) fixed phase Gaussian pulse; (b) Fourier series phase modulated Gaussian pulse; (c) Fully modulated by Fourier series. The gate fidelity is increased in the downward direction.

By setting an initial state $\rho(t_0) = |100\rangle\langle 100|$ for a three qubit molecule as the Trifluorine, i.e., the first qubit is in the excited state while the other two are in the fundamental state (see Figure 25), and applying pulses similar to the discussed above, the final state are the ones in Figure 26. The pulses being a rotation of $Rot_x(\pi/2)$ of the

second qubit should generate the final state

$$\rho(t_f) = \frac{1}{2} [|110\rangle\langle 110| + |100\rangle\langle 100| + i(|110\rangle\langle 100| - |100\rangle\langle 110|)].$$

The fixed phase Gaussian pulse has many populated elements of the density matrix that are not part of the desired final state, by optimizing the phase these are reduced and are localized near the expected final population as can be seen in Figure 26. Nonetheless, the Fourier series pulse has a much cleaner final state, as all other populations are almost zero. Hard square shaped pulses were not plotted, as these have such a bad performance that comparison is unnecessary. Non diagonal terms are mostly a product of the interacting hamiltonian, and are sometimes called *coherence elements* or *interference terms*.

6.4 Robustness to resonance offset

All prior considerations were done assuming that the pulse is focused on the resonance frequency of the target qubit. This means when a gate $\text{Rot}_x(\pi) \otimes \mathbb{I} \otimes \mathbb{I}$ is applied, the resonance is set to be on the first qubit. Although usual calibration of a pulse time or power is done on the qubit resonance, as this is where the effect is maximal in square pulses, when dealing with modulated pulses, it is expected that the optimization is flexible enough to select the frequencies in order to strike the resonance even though a detuning is present.

Remember that our optimization controls the frequency in both the amplitude and the phase in Equation (6.7). So if a frequency offset (ν_{off}) is applied, such that the pulse will be on the shifted frequency $\Delta\omega_{j,RF} = \omega_j - \omega_{RF} - \nu_{\text{off}}$, the optimization may find that the best frequency to pulse is one that corrects the detuning, such as $\omega'_{RF} = \omega_{RF} - \nu_{\text{off}}$. So that the pulsed frequency is then $\Delta\omega_{j,RF} = \omega_j - \omega'_{RF}$. So it is possible in theory that the optimization of modulated pulses is able to refocus the frequency. As will be made clear below, not only the modulated pulses are flexible enough to account for frequency offsets, but, there are also many possible advantages of pulsing out of resonance that are wildly under explored in the literature. Here we will discuss some of the possible techniques that leverage the possibility of out of resonance pulses.

6.4.1 Multi frequency pulses

A technique that is well established is of *linearly phase modulated pulses*. When dealing with homonuclear systems, the frequency distance between two qubits is of the order of 10 kHz, (e.g., Trifluorine frequencies in red in Figure 14). If one is interested in applying a gate to two qubits with a neighbouring frequency, it is possible to add a linear term to the phase modulation. This is sometimes called a *phase ramp*. Let us explain with the following rationale in [40, pg. 145], taking the hamiltonian of a single qubit, and adding a linear phase ramp $\frac{\Delta\phi}{\Delta t}t$, one gets

$$\begin{aligned}\mathcal{H}_{RF}(t) = & \hbar\omega_1(t) \left\{ \cos \left[\Delta\omega_{j,RF} \cdot t + \left(\phi + \frac{\Delta\phi}{\Delta t} t \right) \right] \sigma_x \right. \\ & \left. + \sin \left[\Delta\omega_{j,RF} \cdot t + \left(\phi + \frac{\Delta\phi}{\Delta t} t \right) \right] \sigma_y \right\} \\ \mathcal{H}_{RF}(t) = & \hbar\omega_1(t) \left\{ \cos \left[\left(\Delta\omega_{j,RF} + \frac{\Delta\phi}{\Delta t} \right) t + \phi \right] \sigma_x \right. \\ & \left. + \sin \left[\left(\Delta\omega_{j,RF} + \frac{\Delta\phi}{\Delta t} \right) t + \phi \right] \sigma_y \right\}\end{aligned}$$

so that now the new frequency is

$$\omega = \Delta\omega_{j,RF} + \frac{\Delta\phi}{\Delta t}. \quad (6.13)$$

This means that it is possible to control the frequency by modulating the phase of the Fourier series for the qubit phase. These modulations are called *multiphase pulses*, because it is possible to reach two resonance frequencies with a single pulse, in theory.

As the reader may note, this is not the optimization path we have chosen, nonetheless, because our phase optimization $\phi(t)$ is a Fourier series, any behavior present in linear phase ramps is a possible solution to our modulation, as Fourier series can approximate it with finite terms to a certain extent. However, because such series have an easy representation in frequency space, there is a more clever way to build selective pulses, i.e., to directly select a function that is narrow banded near the multiple desired frequencies. This means that, ideally, one would like to produce a pulse with exactly overlapping frequencies, such as in Figure 27.

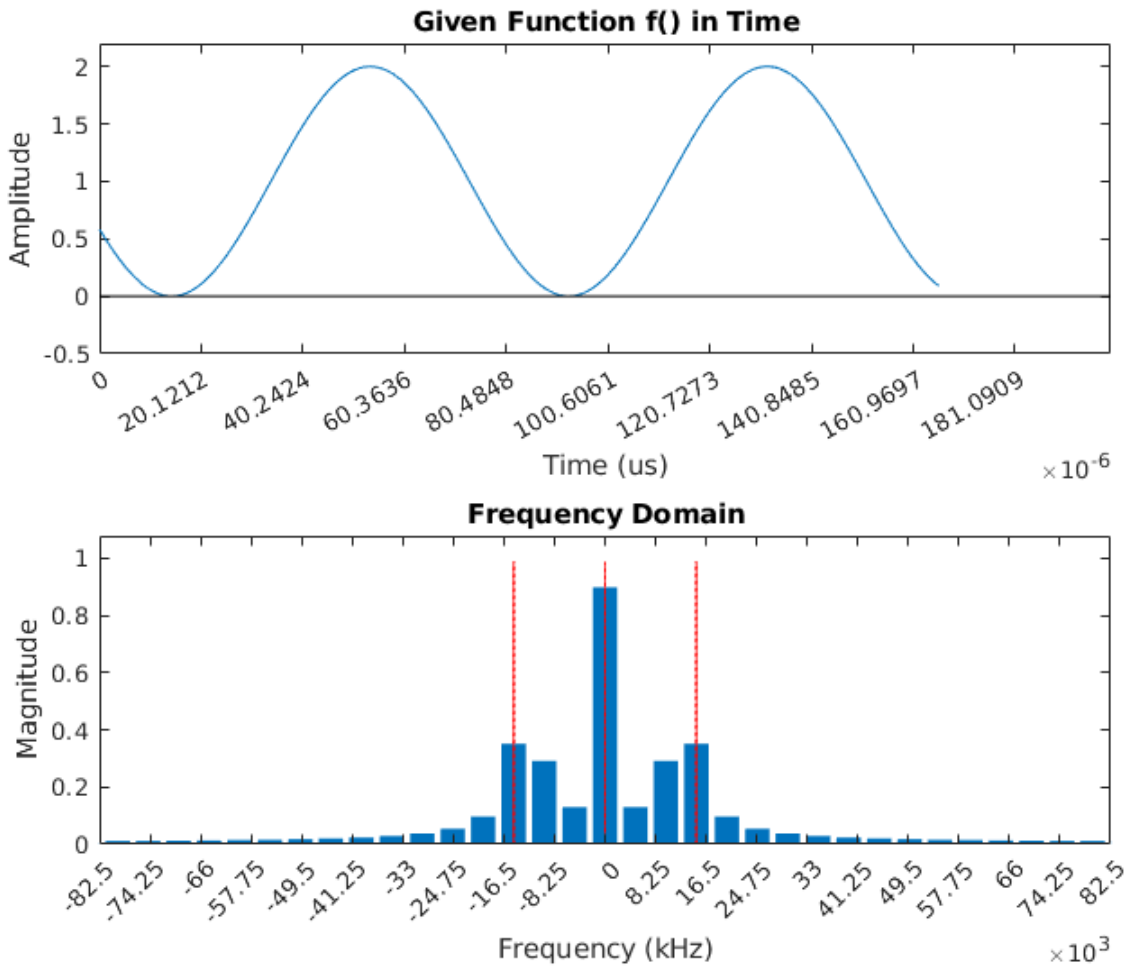


Figure 27 – Example of perfectly overlapped pulse for Trifluorine molecule, this pulse is simply a sinusoidal wave summed with a constant (top), while its Fourier Transform is plotted below. Here the red vertical lines indicate the resonance frequency for each of the qubits in the Trifluorine molecule.

This would offer more control as the height of the Fourier transforms are adjustable. It is easy to see that the modulation is such that out of resonance frequencies are low, while the pulse characteristic frequency overlaps nicely with the qubits resonance. This is a showcase of how selective the optimized pulses can be. However, these were not the pulses found by our optimization method. This suggests that the optimal pulses are most likely not the ones with perfect overlap. To see this, compare Figure 14 and 27, with the following graph of a modulated pulse for a homonuclear system in Figure 28.

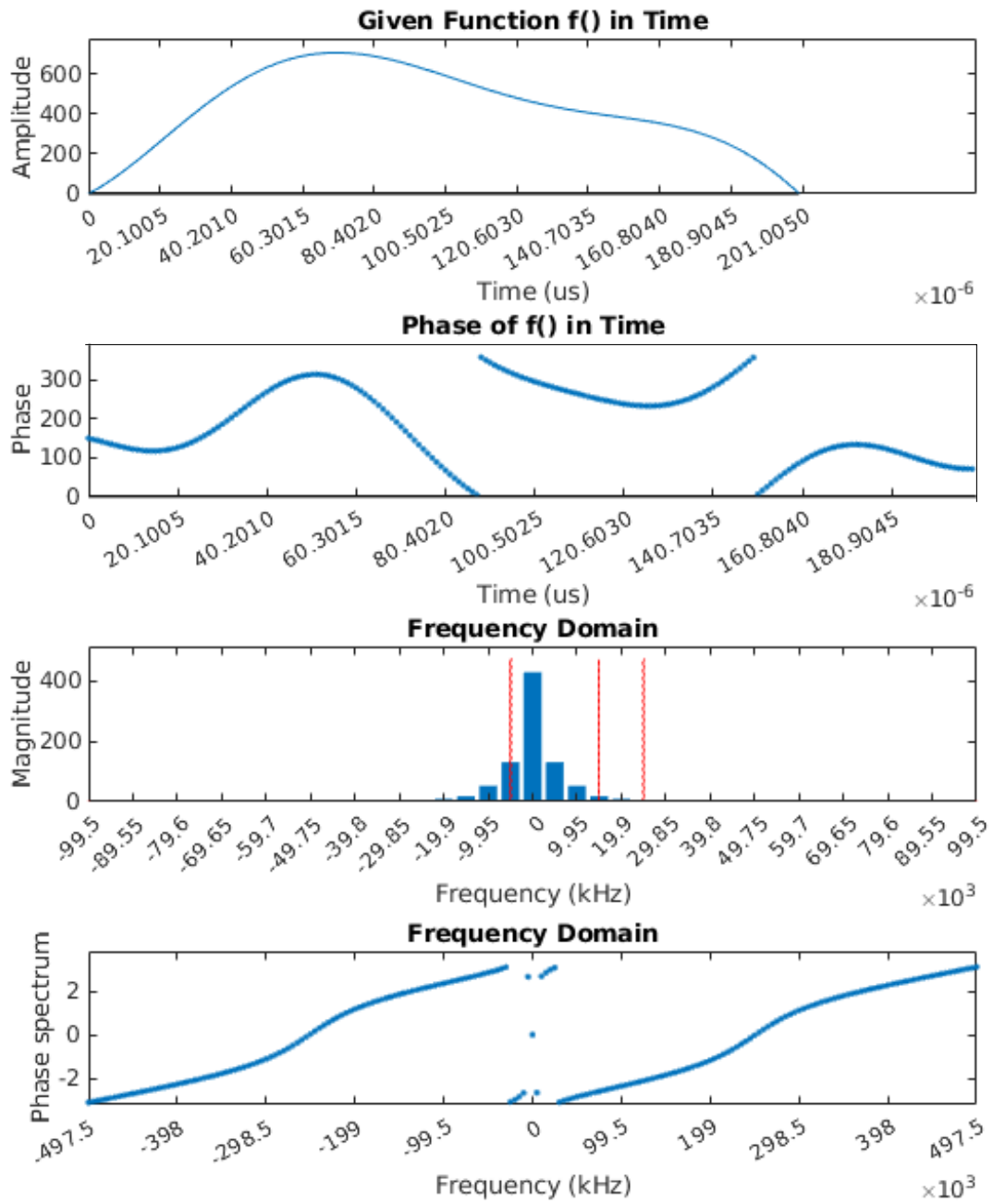


Figure 28 – Plot of a modulated pulse and its Fourier transform in a homonuclear system (Trifluor molecule, represented in Figure 9). Form top to bottom, the amplitude of the pulse is plotted in topmost graph, then the phase is plotted, followed by the Fourier Transform and the bottom graph is the Fourier Transform's phase. The red vertical lines indicate the qubits resonance frequency, an offset of $\nu_{\text{off}} = -25$ kHz from the first qubit (rightmost one) is applied prior to optimization.

One may then see that the optimization finds pulses that are not the perfect overlap of frequencies. This is an expected result when one takes into account that the pulse still has some effect on the qubit even when out of resonance. Such non-trivial effects, which may be hard for the human intuition to follow through, are nicely tamed by the Fourier series modulation. These effects will be further explored in the next subsections.

6.4.2 Robustness to offset (Heteronuclear case)

In the heteronuclear case, it is expected that the square pulse will perform better, but as a proof of principle let us consider modulated pulses. By looking at the Figure 14, it is clear that the 12 μ s square pulse in frequency domain is wide enough to account for tens of kHz of frequency offset. Now compare it to the following 25 kHz offset for a modulated pulse in Figure 29.

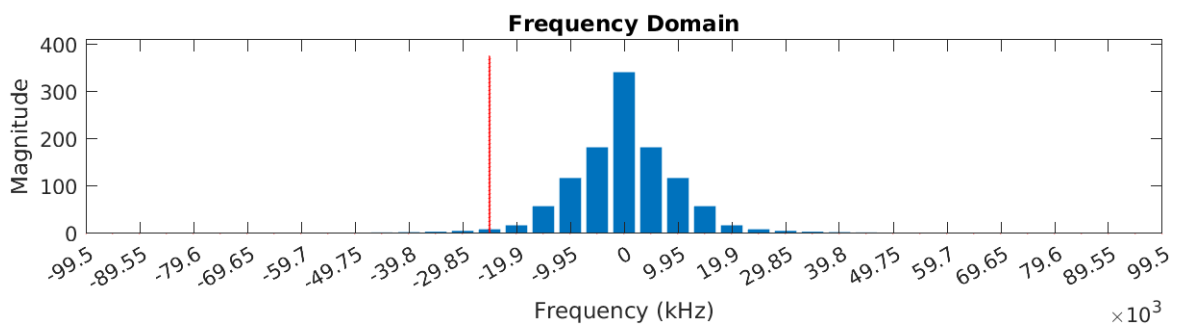


Figure 29 – Fourier transform of a modulated pulse for heteronuclear system (optimized for resonance) in blue. The qubit frequency (in red) is off by 25 kHz. This Figure shows that the optimized pulse is off resonance.

It is clear that the pulse is so out of resonance with the qubit that its effect will most likely be equivalent to the identity operator \mathbb{I} .

Now, for comparison purposes, we have tested numerically the effects of the offset in both the square and modulated pulse, for a $Rot_y(\pi/2)$ gate, from resonance to a 100 kHz offset, see Figure 30.

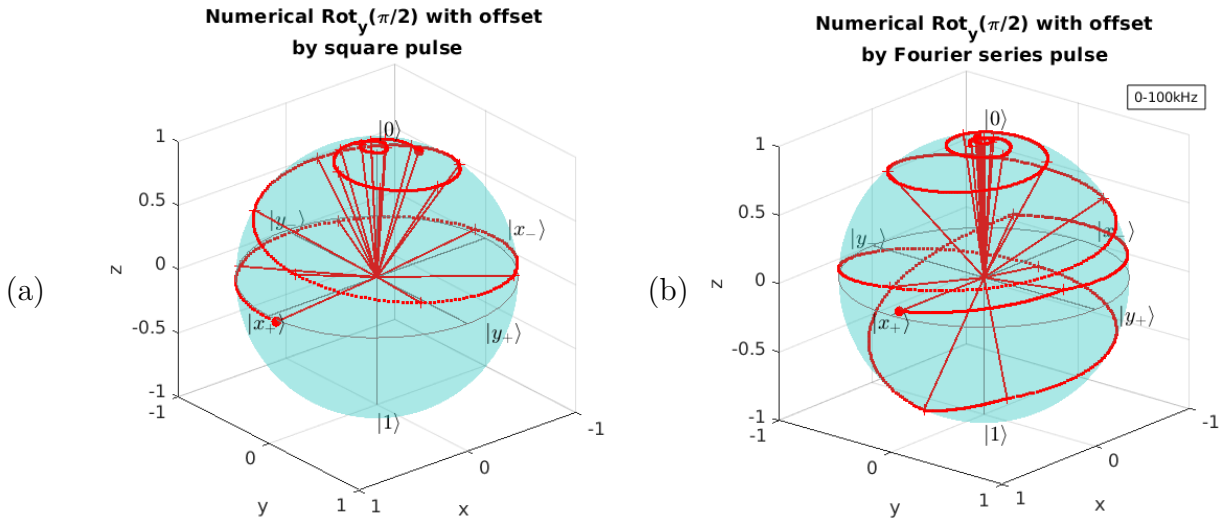


Figure 30 – Simulation of a $\pi/2$ angle on σ_y rotation ($\text{Rot}_y(\pi/2)$), gate applied to the Hydrogen (qubit 1) with an initial state $|0\rangle\langle 0|$ on the Cloroform molecule, i.e., heteronuclear system (the Carbon qubit is traced off), with an offsetted (a) square pulse and (b) Fourier series modulated pulse. Only the offsetted final states are plotted, with offset $\nu_{\text{off}} \in [0, 100]$ kHz. The resonance ($\nu_{\text{off}} = 0$ case) has the final state in $|x_+\rangle\langle x_+|$, but for each increasing offset on the pulse the final state shifts away from $|x_+\rangle\langle x_+|$ following the dotted path. Lines from the origin to the curve indicate a 5 kHz increment.

One may note that the offset has an effect of diverging the intended final state to a neighboring state in the Bloch sphere equator. This means that in this system, if one fixes the analysis for this specific initial and final states, applying a square pulse, offsetted by ≈ 7 kHz is about the same as applying a $\text{Rot}_x(\pi/2)$ gate instead of the intended $\text{Rot}_y(\pi/2)$. This effect is easily explained by looking at the Hamiltonian for the Heteronuclear system in the rotating frame, i.e., Equation (3.21). When one is on the (resonance) rotating frame, but has an offsetted pulse, the perceived effect is to have a “slow” moving Zeeman Hamiltonian, i.e.

$$\mathcal{H}_{\text{Zee}} = -\frac{1}{2}h(\nu_{\text{off}})\sigma_z \quad (6.14)$$

with an effective Larmor frequency equal to ν_{off} . So that when the gate is applied, the observed effect comes with the precession due to the Zeeman splitting. As there is no physical difference in applying a pulse in a resonant rotating frame with an offset, and applying a resonant pulse but in a offsetted rotating frame.

Note that, if one takes into account the state actual trajectory (in the Bloch sphere) of the offsetted pulse, it is not exactly the same as pulsing with a fixed phase difference (although the final states agree). What happens is that, the state drifts to $|y_-\rangle$ instead of $|x_+\rangle$ linearly, because the rotating axis is drifting due to having a lower frequency.

However, as the offset increases the gate loses resonant amplitude and the final state is no longer on the equator, leading to a weaker effect, and ending up as an identity in the limiting case of offset > 50 kHz. One may note that this is a numerical instance of the *rotating wave approximation* (RWA) used in Section 3.3, as the operator no longer has any effect on the target qubit if it is far from resonance. Moreover the 50 kHz threshold also justifies why one can not use this approximation in homonuclear systems.

The fully modulated pulse however loses fidelity to the target $|x_+\rangle$ state much faster, as the axis of rotation varies with the phase change $\phi(t)$, which is now represented in sums of sines and cosines. In Figure 31 only the first 25 kHz form Figure 30 are plotted to facilitate the visualization. One can then note that not only the effect of the change in rotation axis spoils the intended target, but also that the effective Larmor rotation above is also present which may degrade even further the precision on axis of rotation.

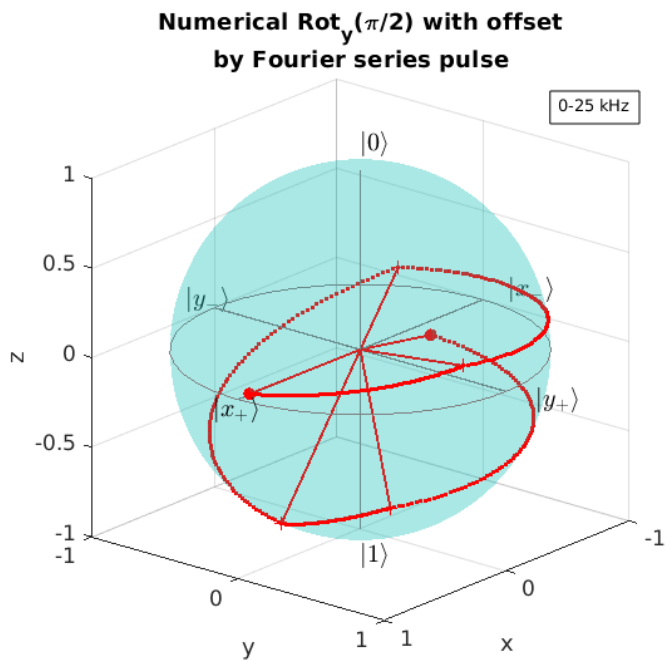


Figure 31 – Detail of the first 25 kHz of offset in the Fourier series modulated pulse in Figure 30. Initial state is $|0\rangle\langle 0|$ and the states after a $\text{Rot}_y(\pi/2)$ are plotted with increasing offset. The resonance ($\nu_{\text{off}} = 0$ case) has the final state in $|x_+\rangle\langle x_+|$, but for each increasing offset on the pulse the final state shifts away from $|x_+\rangle\langle x_+|$ following the dotted path. Lines from the origin to the curve indicate a 5 kHz increment. Notably, fidelity on the final state with $|x_+\rangle\langle x_+|$ is rapidly lost, indicating limitations to the use of offset in modulated pulses.

One could choose to visualize the same effect by looking at the gate fidelity, as in Figure 32.

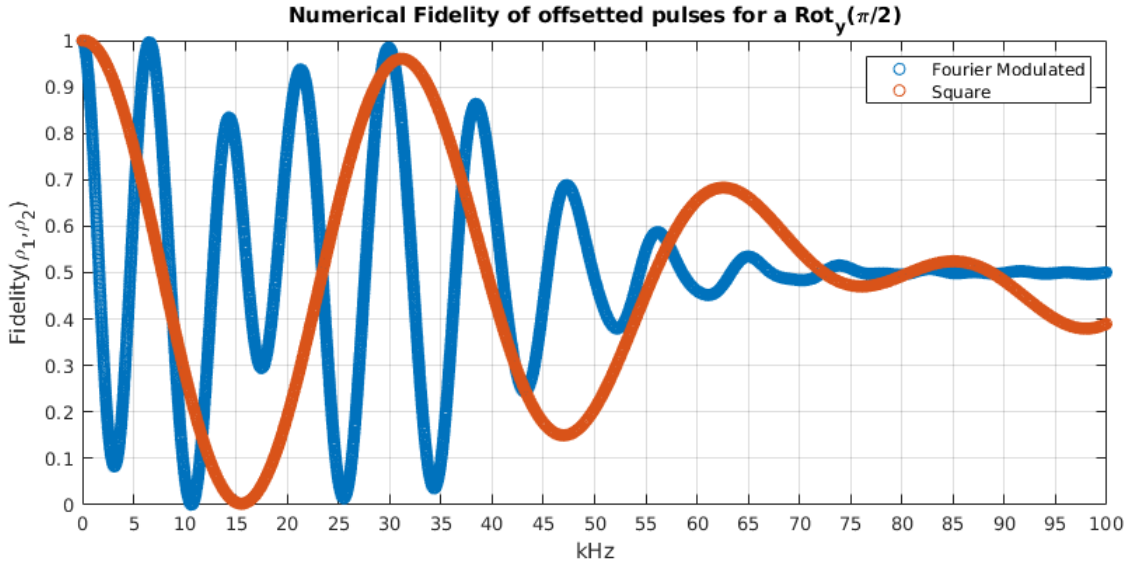


Figure 32 – Plot of numerical fidelities $F(|x_+, 0\rangle\langle x_+, 0|, \rho_f)$ of the final states ρ_f in Figure 30, as a function of the offset ν_{off} , for the square and modulated $\text{Rot}_y(\pi/2) \otimes \mathbb{I}$ gate in a Chloroform molecule (heteronuclear). The modulated pulse loses fidelity much faster than the square pulse.

A strong agreement with the experimental case is noted here, and the reader is invited to read Section 7.3 for the results in similar figures.

6.4.3 Robustness to offset (Homonuclear case)

For the following we have tested numerically the approximation U_g of the desired unitary U_t , to various frequency offsets from resonance to ± 100 kHz. The desired operation is a $\text{Rot}_y(\pi/2) \otimes \mathbb{I} \otimes \mathbb{I}$ gate. It is clear from Figure 14, that the 12 μ s square pulse is unable to select a single qubit, acting strongly on all three qubits in a Trifluorine homonuclear system. However, because the Fourier modulated pulse is very narrow banded it quickly loses control in a small frequency window. Nonetheless, the square pulse is so unselective that it is unable to produce a pulse with satisfactory fidelity.

In the case where there was only one qubit, or where the frequencies were very far apart, the square pulse performed well, however, in this homonuclear case, the bad performance in fidelity is justified by all three qubits being rotated simultaneously, losing selectivity. It should be clear from the earlier discussion and the graph in Figure 33, that modulated pulses are necessary for multi qubit control, as in this case the same techniques used in heteronuclear system are no longer applicable.

One more consideration should be taken into account about the nature of control by optimization. Until this very moment all tests shown were based on the premise of choosing the optimization at the resonance frequency and then studying its comportment out of the resonance frequency. However, we could have chosen to reverse this order,

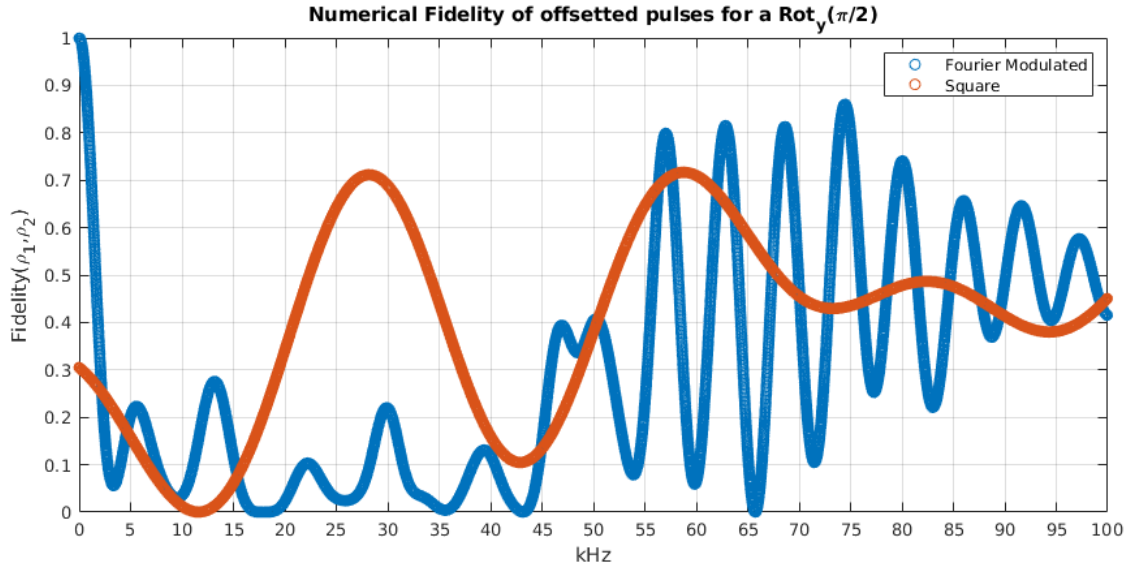


Figure 33 – Plot of numerical fidelities $F(|x_+, 00\rangle\langle x_+, 00|, \rho_f)$, as a function of offset ν_{off} , for the square and modulated $\text{Rot}_y(\pi/2) \otimes \mathbb{I} \otimes \mathbb{I}$ gate with offset from resonance frequency applied to the Trifluorine molecule (homonuclear).

i.e., choosing the offset first and then optimizing the Fourier coefficients to find the best out-of-resonance pulse. Because the optimization already takes into account the Zeeman part of the Hamiltonian, it is already very robust to this effect, as is shown by its good performance at the resonance in homonuclear systems. As discussed in Section 6.4.2, the addition of a offset in pulse frequency is effectively the same as adding an effective Larmor frequency to the qubit (proportional to this offset). In the heteronuclear system, the resonance frequency sets effectively $\mathcal{H}_{\text{Zee}} = 0$ (an approximation that can be done for all qubits due to the RWA regime), and therefore the effect of adding an offset is to put the qubit in motion around \hat{z} in the resonance rotating frame. In the homonuclear case, where the RWA is a bad approximation, all spins are precessing in the resonance rotating frame except for the one qubit that the pulse focuses on. So the pulse is already optimizing to fix this effect, or to take advantage of it for the neighboring qubits. Adding an offset is then an extra possibility to accelerate and/or to make slower said precession of the other qubits. It then may be that there is a optimal offset where all spins are precessing, but none is precessing too fast as to be out of reach to the control. One should bear in mind that, in contrast to the heteronuclear case, here the laboratory spectrometer can only pulse on one RF generator, where as in the heteronuclear case, the control is more refined, by taking advantage of simultaneous pulsing in two or more RF channels.

The following graphs in Figures 34 and 35 support the claim above. All graphs where generated with offsets from the resonance at the first qubit (the rightmost in frequency), where the applied operation was a single gate targeted to this qubit ($\text{Rot}_y(\pi/2) \otimes \mathbb{I} \otimes \mathbb{I}$), remember that the other qubits are separated by a chemical shift providing a frequency shift of -11.83 kHz and -29.16 kHz (as can be checked in Figure 9).

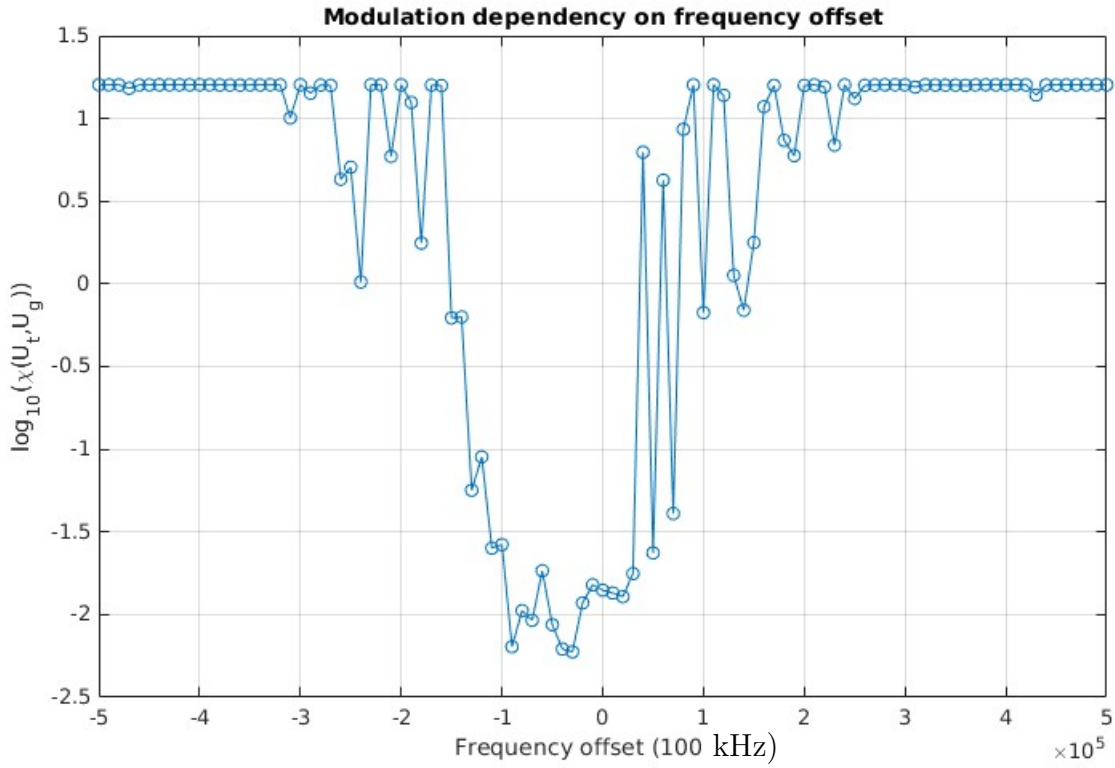


Figure 34 – The loss function $\chi^2(U_t, U_g)$ in a $\log_{10}()$ plot as a function of resonance offset, where zero offset means that it is focused on the first qubit resonance frequency, applying gate $\text{Rot}_y(\pi/2) \otimes \mathbb{I} \otimes \mathbb{I}$, for a homonuclear Trifluorine molecule. The modulation optimization is rerun for each point on the graph, and each dot on the graph is the best of 500 optimization runs. Top values are of $\chi^2 = 16$ as this is the maximal χ^2 loss for 3 qubit systems, lower values are of $\chi^2(U_t, U_g) \approx 0.006$.

Although the advantage of out of resonance optimization is not as obvious from just looking at these graphs. One may notice that the best optimization in Figure 35, is not in the range of the qubit frequencies, i.e., between resonance (0 kHz) and the leftmost qubit in ≈ -29 kHz, as the lowest point in the graph is around 15 kHz. One could then argue that the effect may be due to the random nature of the optimization, and should then configure noise. However, by fitting the curve to a second degree polynomial, which retains its functional form, it becomes evident that the amount of optimizations with the best results is shifted to the left. The minimum of the regression curve is indicated by a black dot, and is exactly on the frequency offset of $\nu_{\text{off}} = -12$ kHz, which is closer to the center qubit (although not quite it): if one restricts the regression to the points where the loss is $\chi(U_t, U_g) < 0.1$ then the regression gives an even more left-tilted frequency of $\nu_{\text{off}} = -14$ kHz, distancing it further from the center qubit, but now closer to the average frequency of the three qubits of ≈ 13.6 kHz.

To better detect the optimal frequency, we ran 10 times the optimization in the

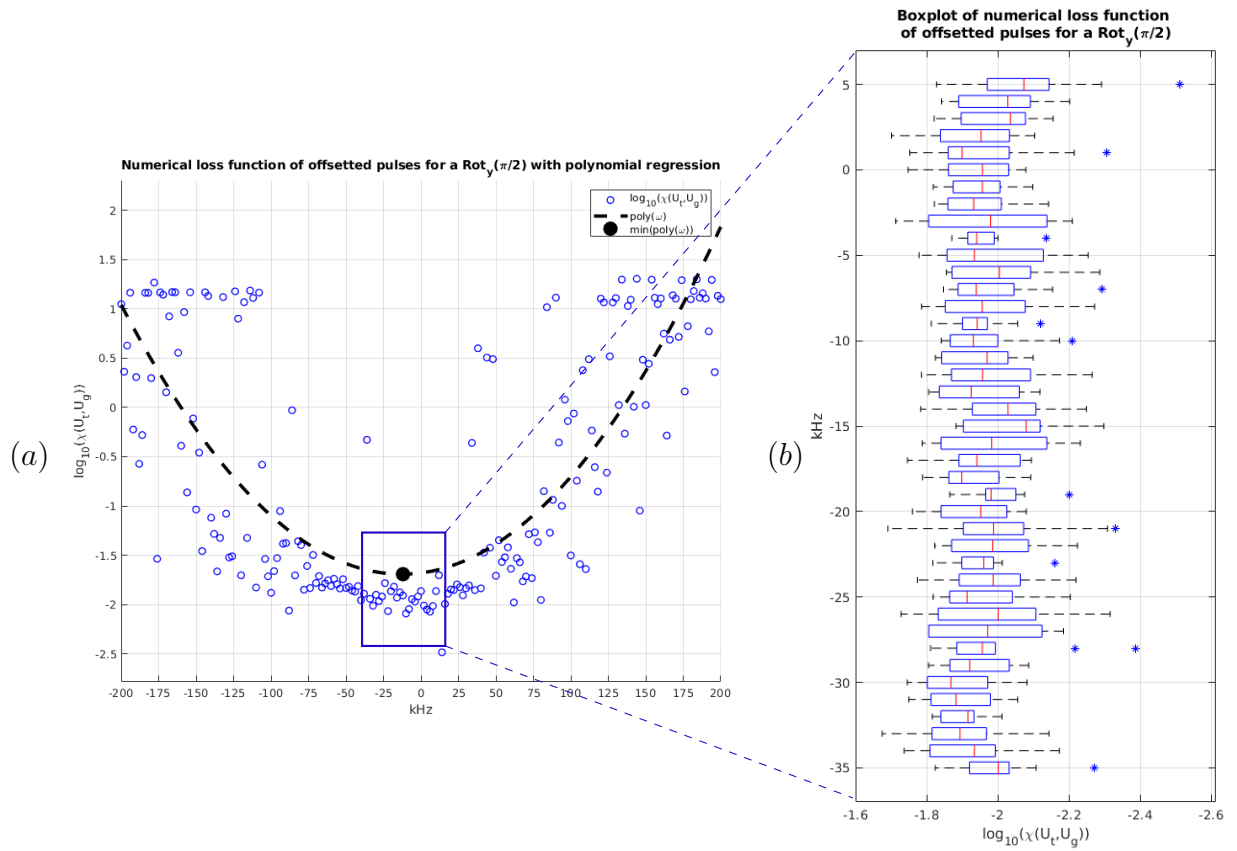


Figure 35 – Detail of Figure 34 with additional points (one for each 2 kHz) restricted to (a) $\nu_{\text{off}} = [-200, 200]$ kHz and plotting for every increment of 400 Hz, a second order polynomial regression is applied, and minimum of such regression is indicated at the black spot at $\nu_{\text{off}} = -12$ kHz, and (b) the region in the blue box is rotated and detailed as a box-plot of 10 rounds of the best of 200 optimizations (2000 optimizations in total), between $\nu_{\text{off}} = [-35, 5]$ kHz, where each box is an increment of 1 kHz in offset and outliers are plotted as asterisks.

smaller window of $[-35, 5]$ kHz with a coarse graining of 1 kHz and produced the box-plot in Figure 35 (b). Remember that we have chosen that each optimization runs 200 initial values and chooses the best one only to plot, this means that each box plot is of 4000 optimization runs⁴ even though only (the best) 20 points are taken to produce the statistical box. The total plot adds up to 77 hours of numerical processing. It is clear from this figure that there is no true advantage to pulsing in a certain frequency anywhere in this range. This is also a strong argument to discard the polynomial fit minimum discussed above as the best choice, as it shows that it is an effect of symmetry in the optimization landscape but not a true minimum, as the landscape is mostly flat in the interval containing all qubits.

Notwithstanding, the graphs show that our optimizations can find pulses that are

⁴ about 112.6 minutes of optimization for each box in the box-plot, when running parallel in a 64GB and a Core intel i7 12700K of 12 (2.70 – 4.90 GHz) core CPU

100 kHz out of resonance and still perform satisfactorily, proving an advantage in frequency reach that is not found in non-optimized pulses such as the Gaussian and square pulses with fixed phases, nor for first optimized then offsetted modulated pulses.

From this discussion one may conclude that the optimization does not find a better loss score only by pulsing on the average frequency, as we have seen that the best scores still depend on random factors of the optimizations initial coefficients. However, because the best scores agglomerate around the average frequency, it is expected that to aim for it configures as an educated guess for better control. Moreover, these tests show that the optimization is very robust in terms of frequency range, as it is still capable of controlling qubits very effectively in a 100 kHz window. It remains to be seen if this effect still occurs experimentally.

6.5 Two Qubit Gates

It should be clear from Section 6.4.1 that all pulses in a homonuclear systems are in a certain sense multi-qubit pulses. Because the frequencies are too similar, a pulse on resonance with a specific qubit, will inevitably affect its neighbors. Moreover, the optimization method developed in this work leverages this fact in its favor, and so acts on the other qubits to guarantee that only the desired target qubit changes state while the others will effectively sense an unitary that is approximately an identity operator at the final pulse duration time τ . However, these are only single qubit rotations (albeit many of them) and therefore are not interacting gates in the sense of making two qubits correlated, for this to happen a coupling interaction is necessary.

In a didactic environment, the first interacting gate in Quantum Computing presented is usually the C-NOT gate [27, p.27]. A gate where, when the second qubit action is conditional on the first, it is given by

$$\text{C-NOT}_{1 \rightarrow 2} = |0\rangle\langle 0| \otimes \mathbb{I} + |1\rangle\langle 1| \otimes \text{Rot}_x(\pi). \quad (6.15)$$

However, there is no special reason for $\text{Rot}_x(\theta)$ being the desired effect. Any other single qubit gate could be used, and so the general expression is of a *controlled unitary*

$$\text{C-U}_{1 \rightarrow 2} = |0\rangle\langle 0| \otimes \mathbb{I} + |1\rangle\langle 1| \otimes U. \quad (6.16)$$

In the NMR setting, as seen in Section 3.1, the interaction is realized by the term $\mathcal{H}_{\text{int}} = 2\pi\hbar \sum_{i \neq k}^N J_{ik} \sigma_z^{(i)} \sigma_z^{(k)}$ in Equation (3.4). This terms is capable of coupling two qubits in the same molecule, and because it is always present in the hamiltonian of the system, it acts all the time, even when the pulses are on. However for short pulses it is not an issue, the situation may differ for long pulses.

The J_{ik} terms may have a long periodicity, and so it is desirable to avoid multiple usages of such gates in NMR, to avoid decoherence in the system. For the Chloroform molecule, the coupling between the Hydrogen 1H and ^{13}C is of $J = 215.1$ Hz [6, p.93]. Then, the produced gate when left under free evolution in a heteronuclear system such as the Chloroform molecule, is given by

$$\exp\left\{\frac{\pi}{4}\sigma_z^{(H)} \otimes \sigma_z^{(C)}\right\}. \quad (6.17)$$

The usual time for interaction gates is of $3/(2J) = 2.32$ ms, about 1 order of magnitude more than the time of ≈ 200 μ s of the designed pulses, and 2 orders of magnitude when compared to usual square pulses ≈ 12 μ s. This means that the effects of the interaction hamiltonian, which are low for the usual square pulses, but is not negligible for the modulated pulse duration.

When dealing with square short pulses, the control has only access to definite X and Y rotation gates, the C-NOT gate in NMR has the form in circuit notation of Figure 36.

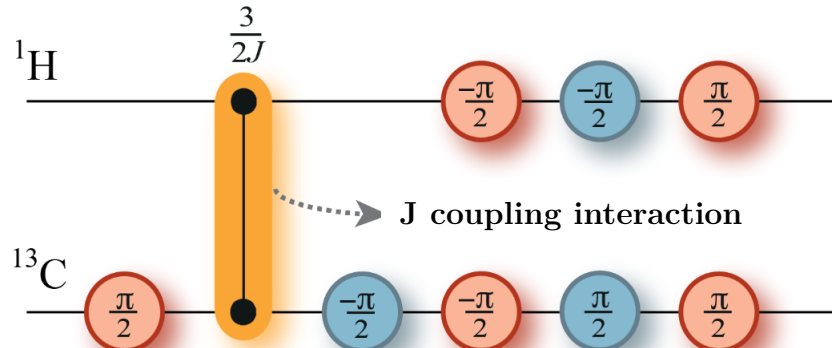


Figure 36 – Example of implementation of C-NOT gate in NMR on a Chloroform molecule, blue circles represent $Rot_x(\theta_x)$ and red ones are $Rot_y(\theta_y)$. Figure taken from [6, p.104].

As discussed in Section 6.2, while it provides good practices to separate X and Y pulses when pulsing with squared shaped amplitudes (as these have very definite straight paths on the Bloch sphere), it makes no sense to do this with modulated pulses, because the pulses are simultaneously X and Y rotations, due to the phase modulation. This means that the C-NOT can be reduced to 3 unitaries gate when using modulated pulses (instead of 9), as the circuit in Figure 37.

This configuration achieves reasonable results, as the optimization function finds unitaries that are good approximations of the C-NOT gate, see Figure 38. Bear in mind that this requires two optimizations: One for U1 and another for U2; the algorithm runs twice, and the J-coupling part is a free evolution (no optimization needed). This means

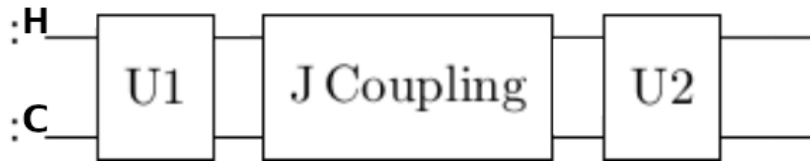


Figure 37 – Model of CNOT realized with modulated pulses, separating the circuit in three operations, based in Figure 36: U1, operations before free evolution; J-coupling, i.e., free evolution; U2 all 7 gates that come afterwards, but now reduced to a single multi-qubit gate.

that the total time of the gate is, $200\text{ }\mu\text{s}$ for each of the U1,U2, plus $2320\text{ }\mu\text{s}$ for the J coupling, giving $\tau_{\text{mod}} \approx 2.72\text{ ms}$, for a C-NOT. On the other hand, the duration of the usual C-NOT in Figure 36 is shorter, as the square pulses are in the order of $12\text{ }\mu\text{s}$, which puts the total gate time to $\tau_{\text{square}} \approx 2.4\text{ ms}$.

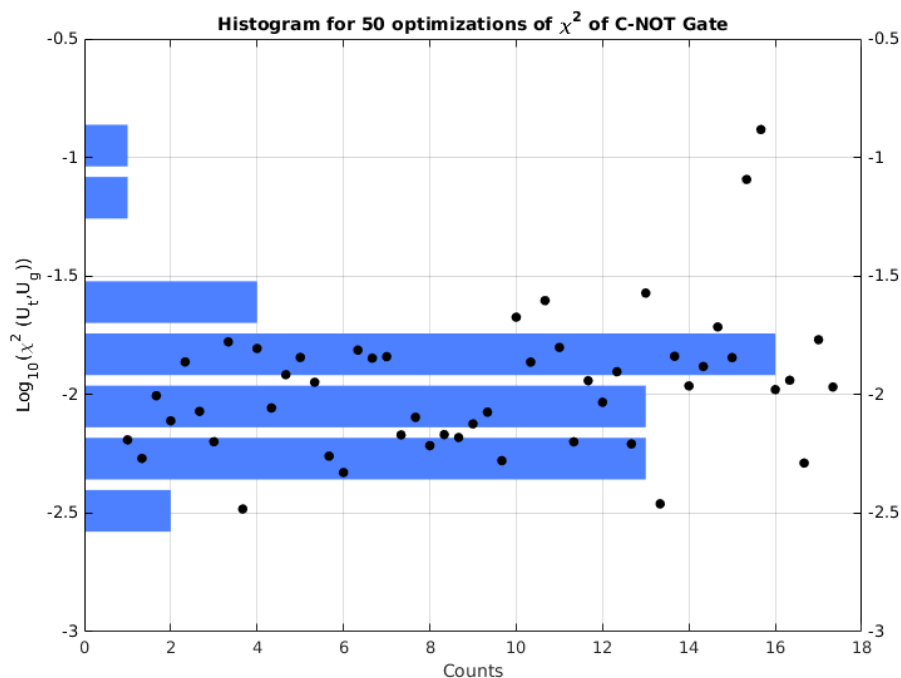


Figure 38 – Histogram and scatter-plot of 50 optimizations of the three gate circuit in Figure 39, producing a C-Not gate. As seen in the histogram, most of optimization find a χ^2 loss of between $10^{-1.5} \approx 0.03$ to $10^{-2.5} \approx 0.003$.

However, because \mathcal{H}_{int} is taken into account during the optimization of the Fourier coefficients, a new strategy for gate optimization is at hand. It is unnecessary to leave the gates U1 and U2 outside of the interaction time. Instead, one could overlap the gates, and then optimize for these very long gates. This is the motivation for the panels (a),(b), and (c) of Figure 39, where the modulated unitaries are gradually “pushed” inside the free evolution.

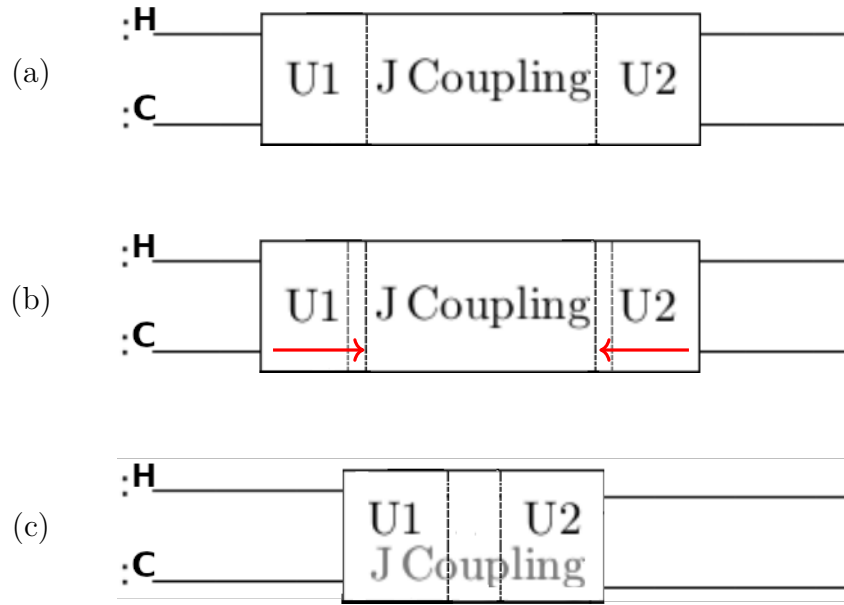


Figure 39 – Model of CNOT realized with modulated pulses. In (a) the same as in Figure 36 is done but with modulated pulses. (b), (c),(d) are increasing time reductions by incorporating the modulated pulses in the coupling time.

Such configurations were tested numerically, in the following manner: Define $U1(k = 0)$ as all gates prior to the interaction gate, and $U2(k = 0)$ all that come afterwards. Now, $U1$ instead of being a rotation on the second qubit, it is given by $U1'$, as in

$$U1'(k) = \exp\left\{\frac{k}{2 \cdot N_k} \frac{\pi}{4} \sigma_z^{(H)} \otimes \sigma_z^{(C)}\right\} \cdot U1(0), \quad (6.18)$$

where, coupling is now

$$J_{\text{Coupling}}(k) = \exp\left\{\frac{N_k - k}{N_k} \frac{\pi}{4} \sigma_z^{(H)} \otimes \sigma_z^{(C)}\right\} \quad (6.19)$$

and

$$U2'(k) = U2(0) \cdot \exp\left\{\frac{k}{2 \cdot N_k} \frac{\pi}{4} \sigma_z^{(H)} \otimes \sigma_z^{(C)}\right\}, \quad (6.20)$$

where N_k is the number of steps taking item (a) to item (c), in Figure 39, i.e., when $k = 0$ we have the fully separated case, and when $k = N_k$ the interaction gate is entirely overlapped by the two unitary gates. The $1/2$ factor in the expression of $U1'$ is to account for the symmetric overlap, as $U2'$ also overlaps from the other side and the product of the three gates as to obey the equation

$$U2'(k) \cdot J_{\text{Coup}}(k) \cdot U1'(k) = U2 \cdot J_{\text{Coup}}(0) \cdot U1 = CNOT. \quad (6.21)$$

This was tested with $N_k = 50$ steps, so that each step k gave an increment of $d\tau = 23 \mu\text{s}$ for each of the U_1, U_2 unitaries. To avoid short modulated gates, which would cause bad approximations, the first $k < 8$ iterations had a fixed $200 \mu\text{s}$ gate on each side, while only overlapping onto J_{Coup} , giving a total time of $(2732 - 23k) \mu\text{s}$. After $k \geq 8$ the total time is fixed on the $3/(2J)$ time duration, i.e., the U_1 and U_2 gates only become larger in expense of the interaction time. The loss function results are plotted in Figure 40

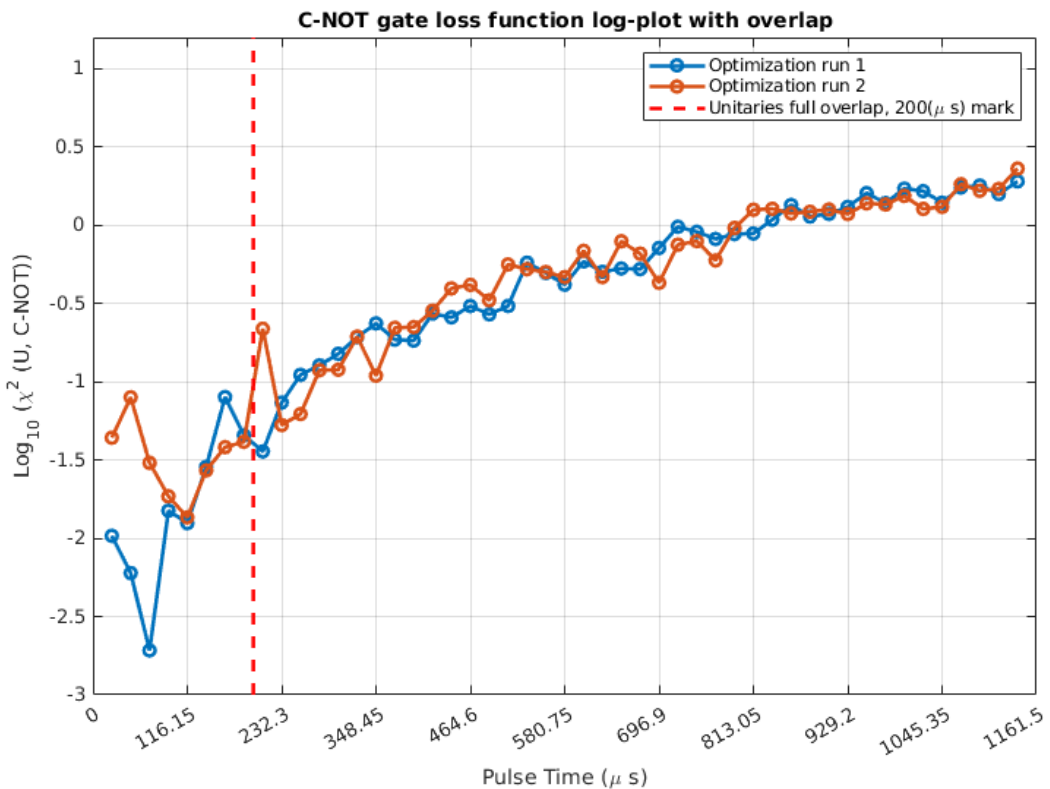


Figure 40 – \log_{10} plot of the $\chi^2(U_t, U_g)$ loss function for the overlapping C-NOT discussed in Figure 39. The same calculations in terms of fidelities is shown in Figure 41

Numerically, fidelities for separated gates are around $F(\rho_t, \rho_g) \approx 0.99971$. For the overlapping case, when $k = 0$, these are the same values, however, fidelities start diminishing already in the first steps of k and fall to values around 0.811 when in the full overlap case. See Figure 41 for the same argument as in Figure 40, but in terms of fidelities.

This means that, contrary to the expected outcome, modulated pulses can account for shorter durations in coupling gates than square pulses. However, there is a limit to the accuracy of the result. Since the best modulation for an interacting gate is no modulation at all, any optimization that pulses anything will only produce more errors. For this reason, after a certain overlap the gate starts to lose fidelity and begins to give bad results. We conclude that the best choice is to pulse only on the firsts and lasts hundreds

of μs , leaving most of the coupling to evolve freely.

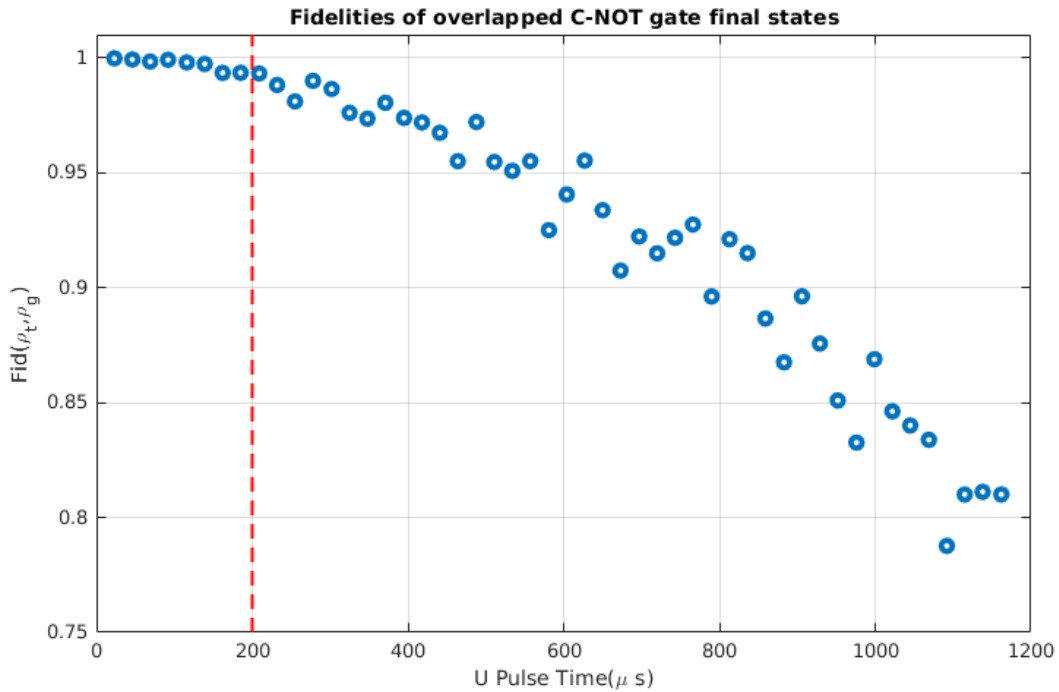


Figure 41 – Plot of the Fidelity function, defined in Equation (2.1.7), for the overlapping C-NOT discussed in Figure 39. The fidelity was calculated between a target state ρ_T resulting from the theoretical C-NOT, and the one resulting from the Fourier generated C-NOT gate ρ_g . Values for no overlap are ≈ 0.99971 , while the last values for big overlaps range around 0.8, showing that fidelity diminishes.

For homonuclear systems, however, these results may be different. Because, the free evolution of the system is not the two qubit interaction anymore, but multiple interactions instead, while at the same time the Zeeman hamiltonian can not be ignored anymore (remember Equation (3.19)). In this case, the free evolution can be a very complex phenomenon, specially when multiple qubits are involved. In this case, modulated pulses could bring an advantage as it is possible that correcting the Zeeman part and/or using it in favor of certain coupling elements while undermining others could direct the evolution to the desired unitary. This remains to be tested, and is left for future research.

Part III

Experiments in NMR

Chapter 7

Experimental Results

Now that the theory and simulations are set, the natural next step is to test whether they agree with experiments. We ran many pulses with varying parameters: type of pulse, time, number of sample points, number of coefficients for the Fourier series. For some of these pulses quantum process tomography was done, in order to guarantee that the rotations were driven by their respective generators.

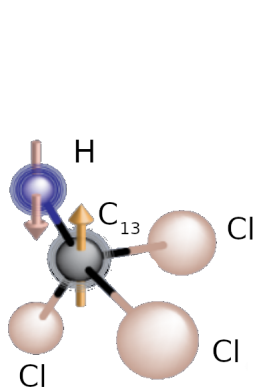


Figure 42 – To the left, the sample, a representation of the Chloroform with the Carbon 13 at its center. To the right, a picture of our lab: Our experimental setup consists of a Varian 500 MHz NMR spectrometer, a computer, and the electronics case to the right. On the table one can see the NMR tubes, with some molecular samples diluted in deuterated solution. Standard practice is to write quantum information pulse sequence processing protocols in C scripts, which are compiled and directly read by the VNMRj software used to operate the machine.

Even though modulated pulses is a technique that has true advantage only in homonuclear systems, due to unavailability of homonuclear samples, all tests were done with Chloroform sample, diluted in deuterated acetone, which is a heteronuclear molecule. As

a result, the gate fidelities observed were generally worse than simple hard pulse pulses, as will be clear below. However, future tests will probably be run with homonuclear systems, where we hope to see significant relative gains.

When calibrating the RF, we usually test for the square pulse, and adjust its time to align the resulting state with the expected final state of a rotation around Y of $\pi/2$. I.e., the initial state is $\rho(t_0) = |0\rangle\langle 0|$, and final state must be $\rho(t_f) = |x_-\rangle\langle x_-|$. This calibration may give different results depending on liquid nitrogen levels, temperature, specific shimming, and many other factors. For a power of 58 dB and $\pm H$ in the observer channel, we obtained 11.4 μ s, and for a power of 57 dB and ^{13}C in the decoupler channel we obtained 10.325 μ s. By setting these reference times, we can find the numerical value of the RF power so that all possible rotation angles are at hand. Also, by knowing the power necessary for the $\pi/2$ rotation, we now know the power bound to do numerical optimization of the modulated pulses. This is important in the sense that, in terms of best experimental practice, the modulated pulse optimization should be run after the spectrometer is already calibrated and shimming was already done. This means that the optimization should not take longer than a day or two, as by this time the calibration may not be the same as the input in the optimization. In our case this type of error is avoided since our optimization is in the order of minutes to tens of minutes, when running parallel in a 64GB and a Core intel i7-12700K of 12 (2.70 – 4.90 GHz) core CPU.

We decided to run with standard numbers of pulse time 200 μ s, $np = 200$, amplitude coefficients $s_A = 8$, phase coefficients $s_P = 14$, whenever values change, it will be said explicitly.

One more consideration has to be taken into account when addressing results in quantum computation in NMR. It is common, due to some approximations in the perturbative approach to the NMR state preparation, that the measured states have negative eigenvalues. For this reason, the usual fidelity measure (the Uhlmann fidelity) is a bad choice, as it relies on the supposition that states are “physical states”, i.e., they conserve probability and therefore have non-negative eigenvalues. So all fidelities written below are actually calculated by the formula

$$\mathcal{F}(\rho_1, \rho_2) = \frac{\text{Tr}(\rho_1 \rho_2)}{\sqrt{\text{Tr}(\rho_1 \rho_1)} \sqrt{\text{Tr}(\rho_2 \rho_2)}} \quad (7.1)$$

avoiding negative eigenvalues, as discussed in Section 2 and formula given in Definition (2.1.7). This measure agrees closely to the Uhlmann fidelity, and is very much standard in the NMR quantum computing literature. In anyway, QST followed by a maximum likelihood procedure will result always in physical states that better describe the experimental data. We also use Equation (2.1.7) for fidelity for the very reason that it is commonly used in NMR literature. With this in mind, let's proceed to the results.

7.1 Varying Pulse type

All tests ran 4 kinds of pulses, either applying rotations around x or around y of $\pi/2$ for comparison: Hard square pulses of $11.4\ \mu\text{s}$; and the three types of pulses of Figure 22. Except for the hard pulse, all the other three were tested in two cases: as *single* pulses (Sing), by operating only one qubit, or *simultaneous* pulses (Simul) operating two qubits simultaneously, see the table below. To clarify, simultaneous pulses are not operating two rotations, instead a simultaneous pulse on the second qubit is pumped to guarantee that the final gate is really a $\text{Rot}_{x_i}(\pi/2) \otimes \mathbb{I}$ gate. The reason for this is that, we expect single pulses to give worst results, because the second channel, even though it has to produce a pulse equivalent to the identity operator, has the function of eliminating undesired coupling between the two qubits during the unitary evolution of the system. Therefore a single qubit gate requires two channels modulating pulses. An observation has to be made, this would not be the case for a homonuclear system, as a single channel would be able to control multiple qubits with similar resonance frequencies, a second probe is necessary for the Chloroform as the qubits have very distant frequencies, being of different atomic number.

Table 2 – Pulse types and measured fidelities

Pulse type	Sing/Simul	Average Fidelity
Hard	Sing	0.9935
Gauss Fixed ϕ	Sing	0.4498
Gauss Modulated $\phi(t)$	Sing	0.9930
Full Modulation	Sing	0.9211
Full Modulation	Simul	0.9839

As we ran quantum process tomography for each of these pulses, the same pulse was applied to four different initial states, (e.g., $|0, 0\rangle\langle 0, 0|, |1, 0\rangle\langle 1, 0|, |x^{(+)}, 0\rangle\langle x^{(+)}, 0|, |y^{(-)}, 0\rangle\langle y^{(-)}, 0|$, where $y^{(-)}$ is the eigenket of σ_y associated with the negative eigenvalue), the average fidelity was measured as the average of the each of the resulting states with its expected outcome.

One may conclude that the hard pulse and the Gaussian with modulated phase are very similar in performance, while the other pulses not as much. Also the simultaneous full modulation has performed better than the single, as expected.

7.1.1 Oscillatory limits of RF generator

Given that the Gaussian pulse with modulated phase in Table 2 has achieved the best fidelity, it is natural to wonder why this is so. As the pulse tested had $200\ \mu\text{s}$, by the simulation results in Figure 23, it was expected that the Fourier series pulse would have a better performance. Of course, as the Fourier series pulse has more freedom in its

optimization, i.e., it has a higher dimensional parameter space, it can find better optima than the other ones, numerically. In spite of that, real RF generators may not have the necessary precision to reproduce such oscillations.

One way to control the oscillation strength is to reduce the number of coefficients in the Fourier series expansion. Because the phase oscillations gave good results with a high number (e.g., $s_P = 14$), we decided to test only a range of values for $s_A \in \{1, 3, 5, 7, 8, 14\}$. The specific pulse with $S_A = 8$ had half the frequency of the others, as initial values for optimization, which justifies it having a better fidelity, if strong oscillations is in fact the issue.

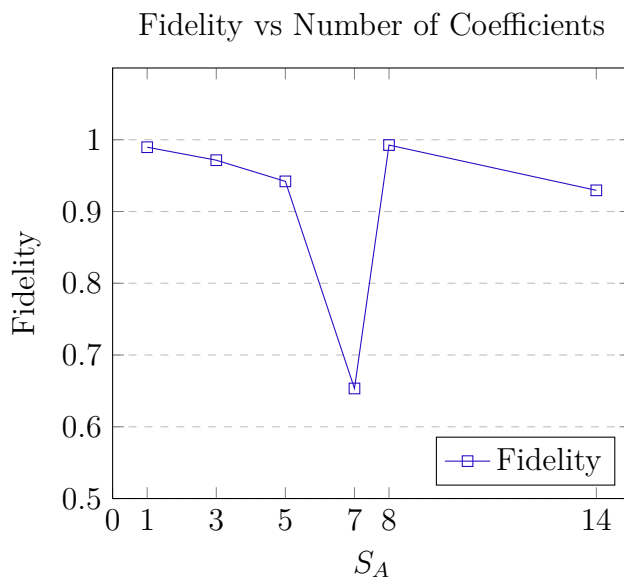


Figure 43 – Number of components in the amplitude Fourier series pulse: S_A value has a slight downward trend with higher coefficients. The value of the coefficient $S_A = 8$ has to be discussed, as it has a high fidelity, but it was a different point, because we tested a pulse with half the frequency of the other points in the graph, concurring with the hypothesis of strong oscillations.

Though the graph trend is not as strong and leaves some doubts, this preliminary data is somewhat suggestive. Because the Gaussian pulse with modulated phase gave such reliable pulses, while fully modulated pulses gave varying results, we concluded, by taking this graph into account, that our RF generator may have some trouble generating oscillations in the amplitude $\Omega(t)$, but not for the phase $\phi(t)$. Because the reference in the literature gave for a Brooker 700 MHz NMR spectrometer, the specific values of $S_A = 7, S_P = 14$, in [44], one could expect that this is the case for its own experiments. However, different spectrometers will have different capabilities and our setup may have some limitations in oscillation ranges for amplitude. We then concluded that inputting lesser coefficients is a rule of thumb for reliable pulses.

7.2 Varying time and number of points

By the discussion in the previous sections, one should expect that fidelity is an increasing function of both the pulse time and the fraction $dt = \Delta t/np$. This was verified by our experiments and gave the following results.

Table 3 – Fully modulated pulses for simultaneous and single RF probe, varying time and sample points (np)

Simul/Sing	Time (μs)	Sample points (np)	Fidelities
Sing	200	200	0.8975
	200	150	0.8801
	200	100	0.513
	150	150	0.6352
	150	100	0.6546
	100	100	0.9481
Simul	400	300	0.9666
	200	200	0.9926
	200	150	0.3894
	200	100	0.6621
	150	100	0.9528
	150	100	0.9499
	100	100	0.9419

However, it occurred that some pulses had a better fidelity, or above average, even though the time was small. So that, even though the trend of fidelity goes downwards with diminishing time, it may be true that a satisfactory point exists that is not found by large times. Also, one should always think about the trade-off that makes the shorter pulses more desirable, as computational time is limited in quantum information processing.

Moreover, the reader may have realized that some pulses have bad resulting fidelities (below 0.9). Although more tests are needed to determine the cause, it is possible that such bad pulses are not results of a lack of phase control but an effect of weak pulsing. We have tested the limit of the sensibility of the qubits to the square pulses, by pulsing many times but with diminishing amplitude, in order to find the threshold were the qubits did not feel the pulse anymore. This threshold is about 2% of the pulse maximum power.

Some Fourier optimizations resulted in pulse modulations that oscillated in very low amplitudes, it then produced experimental pulses that where not felt by the qubits. This effect occurs because, in the simulation, the whole amplitude is added to the hamiltonian, and then even low values add up to produce some effect. Since the pulses are long, even weak oscillations may end up producing the effect numerically, in the long term. Experimentally, however, the qubits are shielded by the electronic field caused by the surrounding electrons and the sample solution, which may dissipate the field or change it before it gets to the nucleus, leading to an effective zero field.

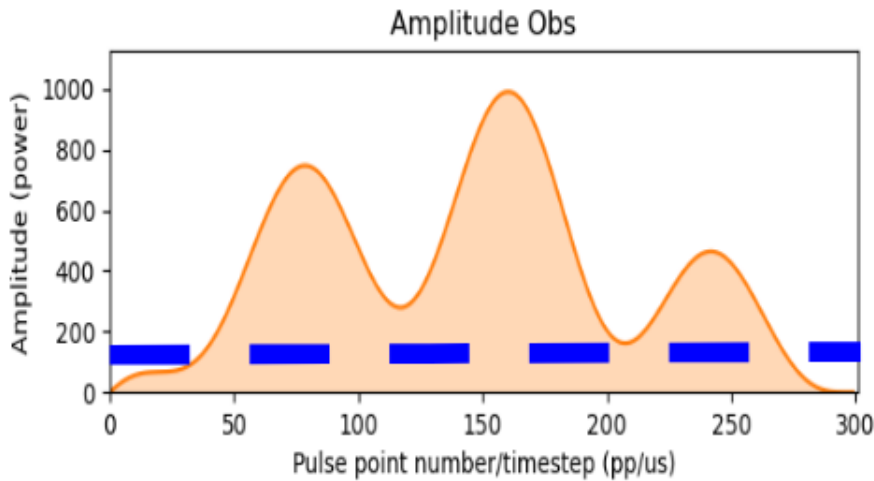


Figure 44 – Pulses with low fidelities in Table 3 may be due to the fact that low amplitudes are not felt by the spins, because there is electronic shielding due to the solvent. Limiting amplitude in the optimization by a threshold may solve this. One should add to the optimization a filter (e.g. two Heavyside functions) that set the numerical effect of the amplitude on the hamiltonian to zero whenever it is below the threshold (about 10% of amplitude).

To avoid this in future tests, one should add to the pulse simulating functions a Heaviside function to the pulse amplitude, which sets to zero below this sensitivity threshold, hence ensuring that only pulses above it are possible solutions to the optimization. See Figure 44, for a reference for the lower bound. This will also force the amplitude to rise quickly in the first time steps, which may lead to shorter pulses when needed, as it maximizes the effects early on.

7.3 Robustness to frequency offset

Going back to Equation (6.7), we wish to see if the pulse is robust to frequency offset, this means that we tested various values of $\Delta\omega = \omega_j - \omega_{RF}$, also called *detuning*. We compared the fully modulated pulse with $100\text{ }\mu\text{s}$ and $np = 100$ (and later $200\text{ }\mu\text{s}$ with $np = 200$), with the hard pulse. By the discussions in Figures 14 and 15, one expects that the hard square pulse would loose fidelity slowly, but would surely have a detuning, as its Fourier transform is smaller away from the resonance. On the other hand, the modulated pulse, having a thinner Fourier transform selective in frequency, should not feel much detuning, until suddenly falling out of resonance, as discussed in Section 6.4.2.

We tested offsets of 5 Hz steps (up to 100 Hz) from the resonance, but fidelities remained unchanged for both types of pulses, as seen in Figure 45. This shows that both pulses are robust to an error of hundreds of Hertz. In hindsight, the steps were too small to have any effect, as by looking at Figure 32, it is clear that effects are not sensible for less than 5 kHz.

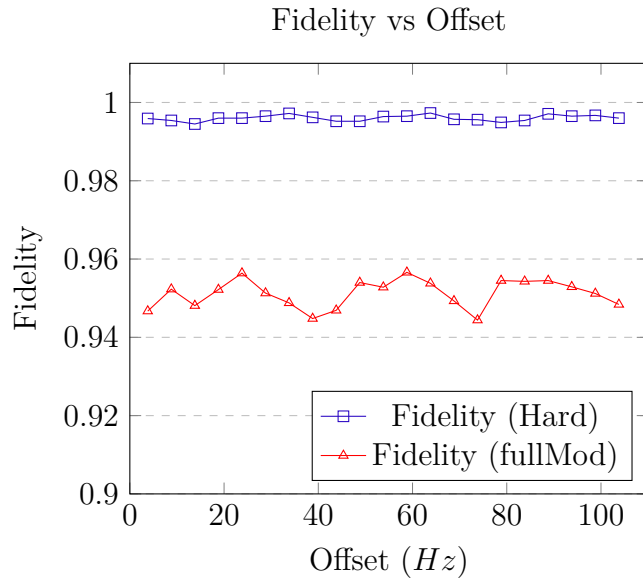


Figure 45 – Plot of two pulses (Hard/Square and fully modulated 100 μ s), and their fidelities. The data begins on resonance for ^1H . As the graph only contains fidelities from 0.9 to 1, one can see that the fidelity is practically unmoved by a 100 Hz offset, as it is indistinguishable from typical experimental noise.

To test the robustness to large offsets new experiments were done with 200 μ s pulses, with increments of 5 kHz. The reader is invited to compare these results with the ones in Section 6.4.2, as this provides experimental support to the numerical curves found there.

For the square pulse, the fidelity falls in accordance to the numerical data. As shown in Figure 46, where the blue curve is made of numerical points while the connected red dots are experimental.

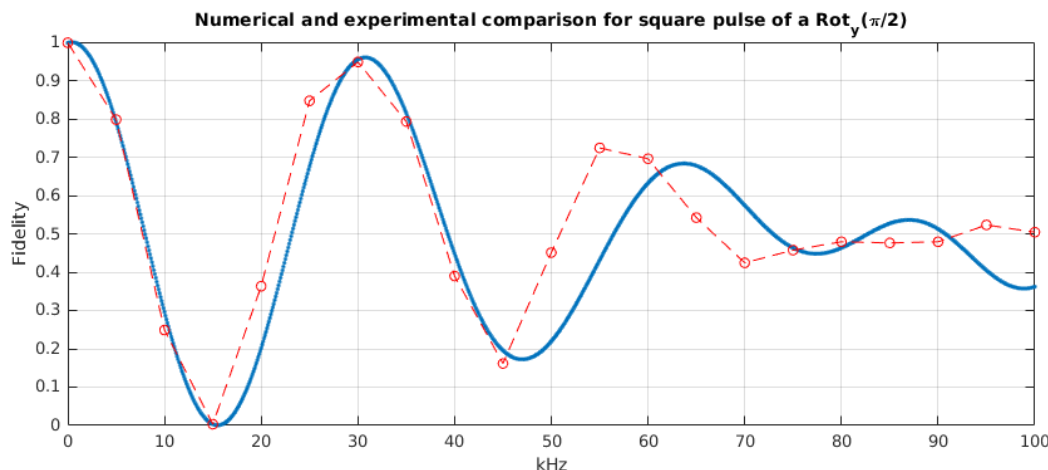


Figure 46 – Comparison of numerical (blue curve) and experimental dots (red) for the square/hard pulse. The graph shows the Fidelity for the square $\text{Rot}_y(\pi/2) \otimes \mathbb{I}$ gate being applied by an square pulse but with increasing offset from resonance frequency to 100 kHz out of resonance.

The same effect can be visualized in the Bloch sphere as in Figure 47, in this case the red curve on the Bloch sphere is the numerical curve, while the dark blue is the experimental one. In the blue curve, the vectors from the origin to the curve represent the actual experimental points each of a 5 kHz offset increment to the qubit resonance under a rotation of $\pi/2$ around the y axis, while the connecting dots are there for clarity. Ideally, the zero offset case (in resonance) should take the state $|00\rangle\langle 00|$ to the state $|x_+0\rangle\langle x_+0|$.

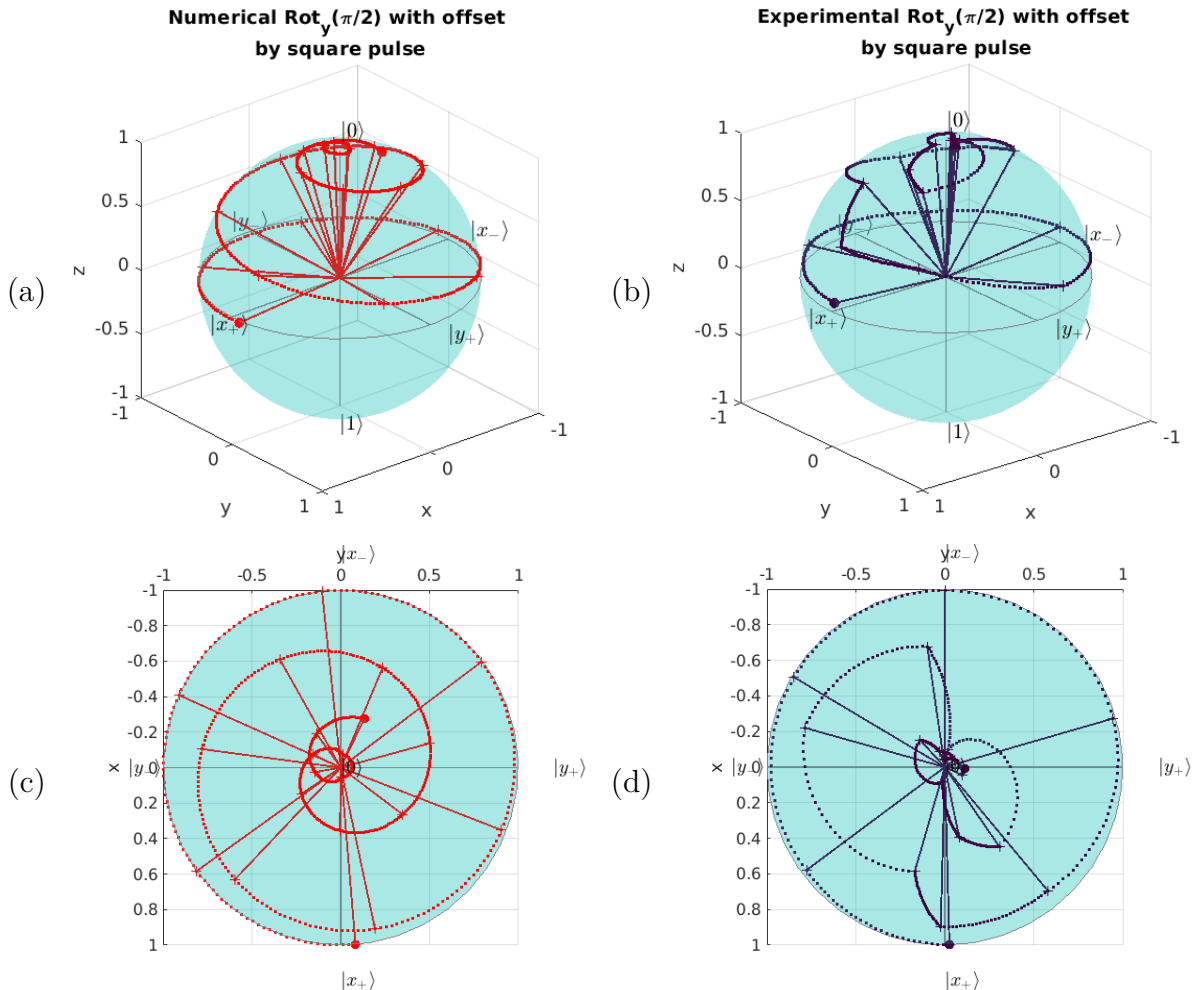


Figure 47 – $Rot_y(\pi/2)$ gate applied to $|0\rangle\langle 0|$ on the Chloroform molecule (the carbon qubit is traced off) with an offsetted square pulse. Results are (a) (c) Numerical and (b) (d) Experimental, where (c) and (d) are top views of the spheres above. Only the offsetted final states are plotted, with offset $\nu_{\text{off}} \in [0, 100]$ kHz. Lines from the origin to the curve indicate a 5 kHz increment, and in additionally (b) indicate the experimental points.

For the Fourier series modulated pulse, the fidelity tracks the numerical curve (blue) on tested points (red), however oscillates much faster than the chosen 5 kHz increment, as seen in Figure 48.

This curve is a showcase that, sometimes, what happens physically may be more complicated than the measured effect, because if one only looked at the experimental points, the

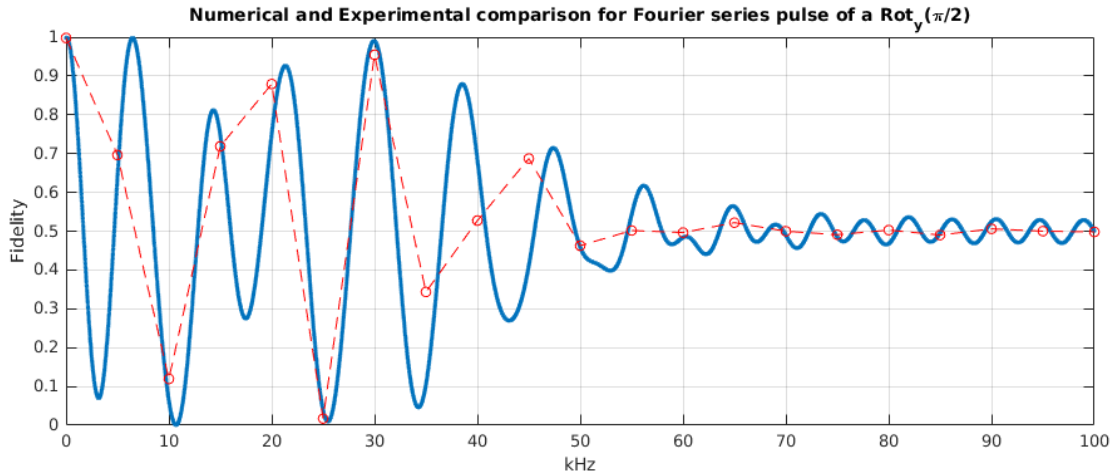


Figure 48 – Comparison of numerical (blue curve) and experimental dots (red). The graph shows the Fidelity for the same gate being applied by the Fourier modulated pulse but with increasing offset from resonance frequency to 100 kHz out of resonance. Experimental points agree with the numerical data.

impression would be that both the square and modulated pulses have a similar performance. A finer coarse-graining for the experimental points in this graph would reveal that the modulated pulse is much more sensitive than what was measured.

The non trivial nature of the offsetting effect on the modulated pulse can be further analyzed by looking at the one qubit Bloch vector, similarly as in item (b) of Figure 30, but comparing now with the experimental results.

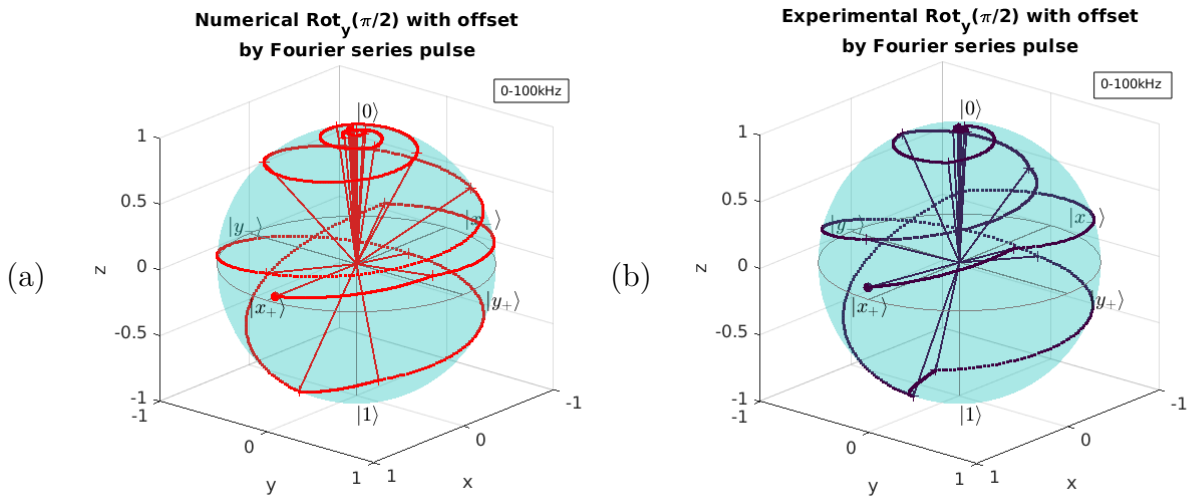


Figure 49 – Simulation of $\text{Rot}_y(\pi/2)$ gate applied to $|0\rangle\langle 0|$ on the Chloroform molecule (the carbon qubit is traced off) with an offsetted Fourier modulated pulse, being (a) numerical and (b) experimental. Only the offsetted final states are plotted, with offset $\nu_{\text{off}} \in [0, 100]$ kHz. Lines from the origin to the curve indicate a 5 kHz increment, and for (b) indicate actual experimental points.

It should be noted that both Figures (in dark blue) 49 and 47 are experimental

plots, and so are actually measurements of the target qubit by tracing out the second qubit and plotting on the Bloch sphere the resulting state. This is not an issue for the square pulse, as it is a single qubit gate, but one has to bear in mind that the modulated pulse is simultaneously pulsing in both qubits in the Chloroform molecule, and uses the carbon nucleus spin to correct via the interacting hamiltonian. Because this information is traced out when looking at the single qubit Bloch vector, it is unclear how this correction acts on the paths on the sphere. A deeper look into this could give interesting insights into the nature of control via interaction with neighboring qubits, possibly by repeating the experiment with the decoupler (Carbon) magnetic field turned off for comparison.

Moreover, the modulated pulses vary the phase in such a way that the rotation axis changes for every time step, but ends at the specified time as if it was a rotation around a fixed angle. This may cause another error contribution, besides the state rotation. This error is noticeable for states that are close or parallel to the intended axis of rotation, see the comparison for the numerical (error free) and experimental rotation $\text{Rot}_y(\theta)$ applied to the initial state $|y_+\rangle\langle y_+|$ as in Figure 50

These plots indicate that the offset causes a strong loss of phase precision, which is noticeable in this specific initial state, where the final Bloch vector oscillates wildly for small offsets, starting at $|y_+\rangle\langle y_+|$ and passing through the orthogonal states $|0\rangle\langle 0|$ and $|1\rangle\langle 1|$, for less than 10 kHz of offsetting. It could be argued that intensification of loss in phase control is restricted to the case where offsetting is present, as the discussion above may suggest. However, the error in phase is still present even when $\nu_{\text{off}} = 0$, i.e., in resonance, as seen in Figure 51

The final states are very discrepant when comparing the theoretical state and the experimental one, indicating that our model lacks precision in the case of almost parallel states and rotation axis; where no pulse (anything, for that matter) would produce better results.

One can then conclude that, even though the optimization is state independent (as it optimizes the unitary) care should be taken in which initial state the pulse is applied when in the experimental setting. Or one could choose to add to the optimization loss function in Equation (6.9) another term that penalizes pulses where these two vectors have a strong overlap, this would however change the nature of the optimization, as it would then be dependent on the initial state, which is something we actively avoided. It should minimize the following expression added to (6.9)

$$\mathcal{L}(\phi(t), \rho) = \frac{1}{\hat{n}_R \cdot \hat{v}_B} \quad (7.2)$$

where

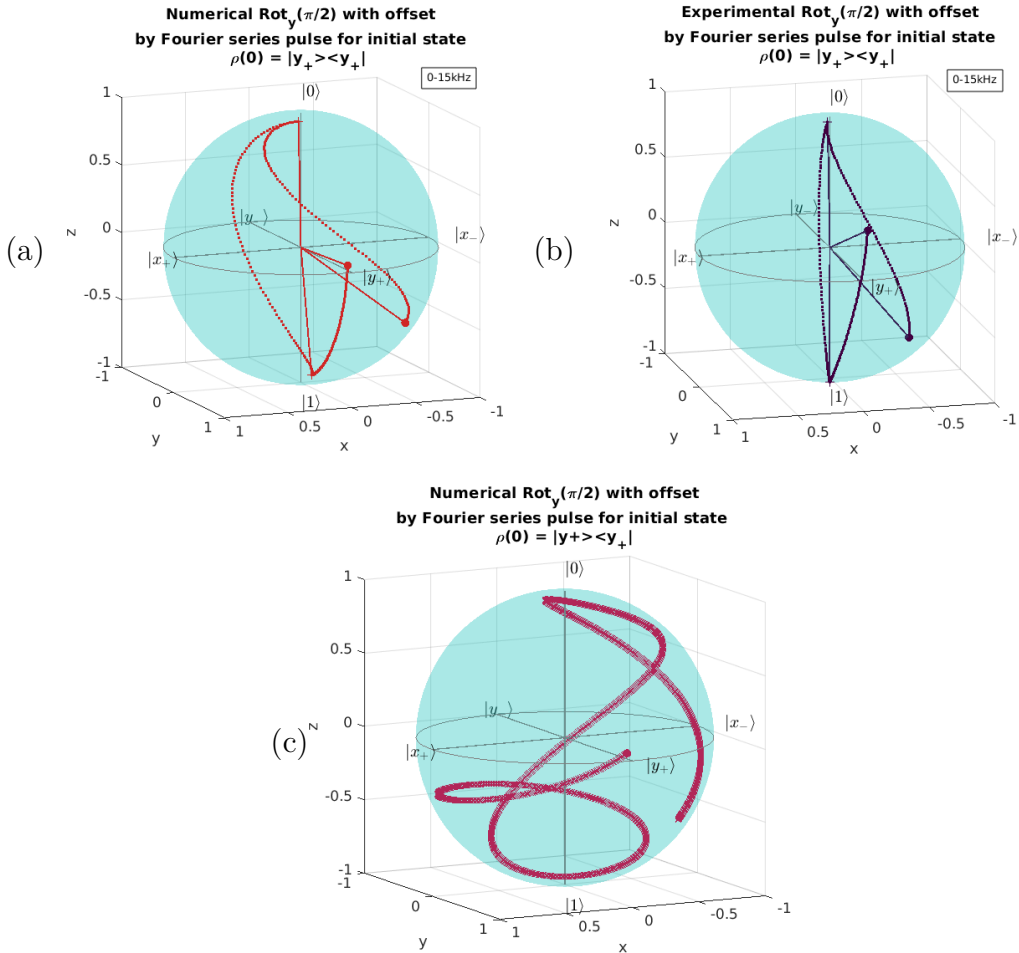


Figure 50 – Simulation of $\text{Rot}_y(\pi/2)$ gate applied to $|y_+\rangle\langle y_+|$ on the Chloroform molecule (the carbon qubit is traced off) with an offsetted Fourier modulated pulse, being (a) numerical and (b) experimental. Only the offsetted final states are plotted, with offset $\nu_{\text{off}} \in [0, 15]$ kHz. Lines from the origin to the curve indicate a 5 kHz increment, and for (b) indicate actual experimental points. (c) is the full numerical path, where all points are plotted

$$\hat{n}_R \cdot \hat{v}_B = [\cos(\phi(t)) \quad \sin(\phi(t)) \quad 0] \cdot \begin{bmatrix} \langle \rho \sigma_x \rangle \\ \langle \rho \sigma_y \rangle \\ \langle \rho \sigma_z \rangle \end{bmatrix}$$

It should be noted however, that this is a lesser constraint than optimizing directly on states, as there are infinitely many rotation axes that are orthogonal to the initial state. This is, however, subject for further research.

7.4 Experimental Quantum Process Tomographies

In this section we will further explore the discussion in Section 2.5, on Quantum Process Tomography, and explain in details an algorithm developed to detect the noise sources

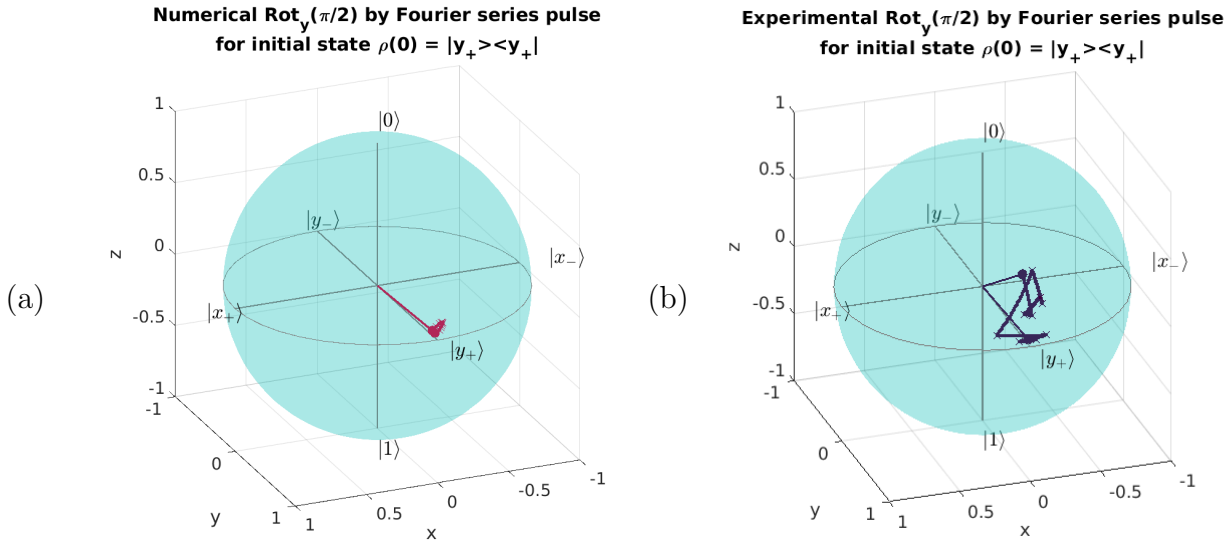


Figure 51 – Simulation of $\text{Rot}_y(\pi/2)$ gate applied to $|y_+\rangle\langle y_+|$ on the Chloroform molecule (the carbon qubit is traced off), being (a) numerical and (b) experimental. Lines from the origin to the a filled dot indicate initial and final state, while intermediary states for each $20 \mu\text{s}$ of the $200 \mu\text{s}$ pulse are plotted as crosses, which in (b) are the experimental dots. Lines on the sphere surface are only to connect the dots and make the order clearer, these are not the actual path.

in a given hardware, based on QPT. Ideally, after a trustworthy noise characterization is complete, one can then re-frame the discussion on Chapter 6 as a open quantum system control problem. The prior model built on pulse optimization relied on the assumption that the system evolutions where unitary and $\rho(t)$ evolved under the Equation (2.8), as stated in Equation (6.12) , which makes the theoretical framework easier to work with, but leads to inaccuracies, as it is effectively ignoring noise processes. Because the optimization algorithms are ready, this extensions is rather a modeling problem then an algorithmic one. Let us discuss how this could be possible.

7.4.1 An inverting algorithm for QPT

As we have discussed in Section 2.5, the Choi Process Matrix gives the coefficient of a Quantum Channel under the operator basis of choice. Notwithstanding, in the example given in that section, the question on how such coefficients are related to the noise parameters, in a combination of primitive maps description, is not quite straightforward, as the reader may note by the process given in the beginning of the example and the resulting expression in Equation (2.39). This problem becomes harder when multiple Pauli map noise sources are available, p_x, p_y, p_z , and even worse when amplitude damping is also present. Nonetheless, the Choi matrix should have all the noise and unitary evolution information present in it, as it fully characterizes the Quantum Channel. This then motivates us to search for a way to decompose the Quantum Channel in terms of the Pauli channels and

the generalized amplitude damping, by knowing only the Choi Process Matrix.

Let us start with a property of the Choi Matrix that already gives us plenty of information: Suppose we have a quantum system free of amplitude damping, then χ has a single eigenvalue λ with $|\lambda|=1$, if and only if the Quantum Channel is purely unitary.

Remember, that a unitary evolution is expressed as $\mathcal{E}(\rho) = U\rho U^\dagger$. This means that if χ has a single eigenvalue, then it can be diagonalized in such a way that one entry $\chi_{jj} = \delta_{ji}$. So that it has a single operator U , choosing to write the channel in a basis of $SU(2)$ that contains U , where $\sigma_k = \sum_{i=0}^3 u_i U_i$, where $\sigma_0 = i\mathbb{I}$, that makes

$$\begin{aligned}\mathcal{E}(\rho) &= \sum_{kl} \chi_{kl} \sigma_k \rho \sigma_l^\dagger \\ &= \sum_{nm} \tilde{\chi}_{nm} U_n \rho U_m^\dagger \\ &= \sum_{nm} \delta_{nj} \delta_{mj} U_n \rho U_m^\dagger \\ &= U_j \rho U_j^\dagger\end{aligned}$$

For the other direction of the proof, it is straightforward to note that if the process is unitary then clearly χ has a single element, and it is equal to one.

This already gives us a rudimentary criteria for evaluating the presence of noise in our system. One can check the eigenvalues of χ , if there are two, then the system is noisy. However, we wish to evaluate the type of noise with more detail than this.

Let us then develop an algorithmic approach that teaches us more about the nature of noise by looking at the Choi matrix. First we assume that all operations and noise in a single qubit gate is given by 9 parameters, given by a process vector

$$\vec{w} = (\theta_g, \theta_x, \theta_y, \theta_z, p_x, p_y, p_z, p_a, q_a) = (\vec{u}_{1 \times 4}, \vec{p}_{1 \times 5}) \quad (7.3)$$

where the vector that spans the first four entries \vec{u} is responsible for the unitary part of the process, i.e, θ_g is a global phase, θ_{x_i} are the rotation angles on the Bloch Sphere, so that $\theta \in [0, 2\pi]$, and the last 5 dimensions are spanned by \vec{p} , composed by the Pauli noises and the amplitude damping probabilities (p_a, q_a) , where $p_{x_i}, p_a, q_a \in [0, 1]$.

With such a vector in hand, then one can write the full channel simply by composing all of these channels as

$$\mathcal{E}(\rho) = e^{i\theta_g} \mathcal{E}_a(\mathcal{E}_{p_z}(\mathcal{E}_{p_y}(\mathcal{E}_{p_x}(\mathcal{E}_U(\rho))))) \quad (7.4)$$

where $e^{i\theta_g}$ is the global phase channel, $\mathcal{E}_U(\rho) = U\rho U^\dagger$ is the unitary part of the process, $\mathcal{E}_{p_{x_i}}(\cdot)$ are the Pauli noise channels, and $\mathcal{E}_{p_a}(\cdot)$ is the amplitude damping channel. We have

chosen the ordering of $U = \text{Rot}_z(\theta_z)\text{Rot}_y(\theta_y)\text{Rot}_x(\theta_x)$, so that the rotation in x occurs first and z last. This ordering is a particular choice so that our algorithm has a smaller set of operators to deal with, one could easily extend this by testing multiple orderings. As stated in Section 2.5, by measuring the states $\{|0\rangle\langle 0|, |1\rangle\langle 1|, |x_+\rangle\langle x_+|, |y_-\rangle\langle y_-|\}$ before and after the channel, we can find the χ matrix.

However, we wish to build an algorithm that solves the other direction of this issue: Given a process matrix χ (possibly experimental), how does one find the noise coefficients in the parameter vector (Equation (7.3))?. This type of problem, where one way of the function is already known but we are looking for ways to invert it, is called an *inverse problem*.

A possibility to this is a “trial and error” algorithmic approach to noise searching. By the same arguments in Section 6.2, we need a loss function, and an optimization task. The optimization function can be the same as the one chosen then, defined in Equation (6.9), where we have a quadratic function on the difference between the matrix elements, but this time the matrices are the experimental χ_{exp} and the one generated by a guess of parameter vectors $\chi(\vec{w}_0)$. So that

$$\chi^{(2)}(\chi_{exp}, \chi(\vec{w})) \geq 0 \quad (7.5)$$

and is zero whenever $\chi_{exp} = \chi(\vec{w})$.

So each step of the optimization is calculated via Nelder-Mead, and checks if the new parameter vector \vec{w}_{n+1} is such that $\chi^{(2)}(\chi_{exp}, \chi(\vec{w}_n)) \geq \chi^{(2)}(\chi_{exp}, \chi(\vec{w}_{n+1}))$

Unfortunately, as great as this seems, it is not enough to find the right set of parameters, since multiple different set of parameters give the same χ matrix. Let us demonstrate it through an example:

Suppose a rotation of π is applied in the X direction, remember that $\text{Rot}_x(\pi) = X$. So that the resulting state is $\rho(t) = X\rho(0)X^\dagger$. Now let us calculate the evolution of a π rotation around y and then a π around σ_z

$$\rho'(t) = ZY\rho(0)Y^\dagger Z^\dagger \quad (7.6)$$

$$= (-i)X\rho(0)(-i)X^\dagger \quad (7.7)$$

$$= X\rho X^\dagger = \rho(t) \quad (7.8)$$

where we have used the fact that $ZY = -iX^1$. This effect is not particular to the angle π chosen, nor to the gates chosen, and occurs for any angle chosen. This means that, if only the initial and final times of a process are taken into account, there is no way to

¹ More generally, $\sigma_i\sigma_j = i\epsilon_{ijk}\sigma_k$.

distinguish between these two processes. Because there are infinite possible angles that generate a level set on our loss functional $\chi^{(2)}$, it may converge to an optimal parameter vector, but there is no guarantee that it will find the desired parameter vector.

For the reasons above the following assumption is made in our search algorithm: The user knows the target unitary gate that should be implemented, i.e., the user knows \vec{u} in (7.3). This is justified by the pragmatic use of the algorithm: the user will usually be interested in discovering the noise in his system, and not the unitary part that has occurred in it. Also, because the χ matrix is symmetric when there is no amplitude damping, introducing noise also changes the symmetry in the coefficients distribution, so that the noise is more informative in the Chi matrix than the unitary part. This gives us hope that finding the noise is attainable.

With the assumption above, there is an educated guess for the initial parameters, which is to use the known parameters to restrict the parameter space and eliminate degenerate surfaces in at least 4 variables. In effect, we are reducing the dimensionality of parameter space by four.

Although the choice above is the best in the given circumstances, we will choose an initial guess of parameters that is user independent, but is inspired by the same reasoning above. Our algorithm obeys the initial parameter guess by taking the diagonal elements of the χ matrix and setting $\theta_i = \pi \cdot \chi_{ii}$, where $\theta_0 = \theta_g$, for $i = 0$, and θ_{x_i} for $i = 1, 2, 3$, assuming the 4x4 matrix elements are indexed starting on zero.

Let us give some of the results obtained. For a small set of angles (i.e., maximum 2 angles), and noise restricted to $p \leq 20\%$ (which is much above what is expected experimentally, usually below 5%), the algorithm performed well.

$$\hat{u} = \begin{pmatrix} \theta_g \\ \theta_x \\ \theta_y \\ \theta_z \\ p_x \\ p_y \\ p_z \\ p_A \\ q_A \end{pmatrix}, \quad \hat{u}_{\text{true}} = \begin{pmatrix} 0 \\ 0.3927 \\ 3.1416 \\ 0 \\ 0 \\ 0.05 \\ 0 \\ 0.08 \\ 0.08 \end{pmatrix}, \quad \hat{u}_{\text{gen}} = \begin{pmatrix} 1.1910 \\ 0.3927 \\ 3.1416 \\ -0.0 \\ 0.003 \\ 0.0529 \\ 0.0001 \\ 0.0744 \\ 0.0471 \end{pmatrix} \quad (7.9)$$

Results are more unpredictable when optimizing on 3 angles. As one can see, although we have not given the unitary angles explicitly, with the exception of the global phase, the generated parameter vector comes very close. For the noise parameters it also has shown lower than 5% error on the Pauli noise values, but for the amplitude damping parameters it has given results that are close but not satisfactory. The lack of precision on

the amplitude damping is justifiable by the fact that the algorithm lacks information, as 4 states in a MUB basis are not enough to fully characterize χ when amplitude damping is present, as it is no longer symmetric.

In terms of the produced Chi matrix, the result is indistinguishable for the human eye from the target matrix. See Figure 52

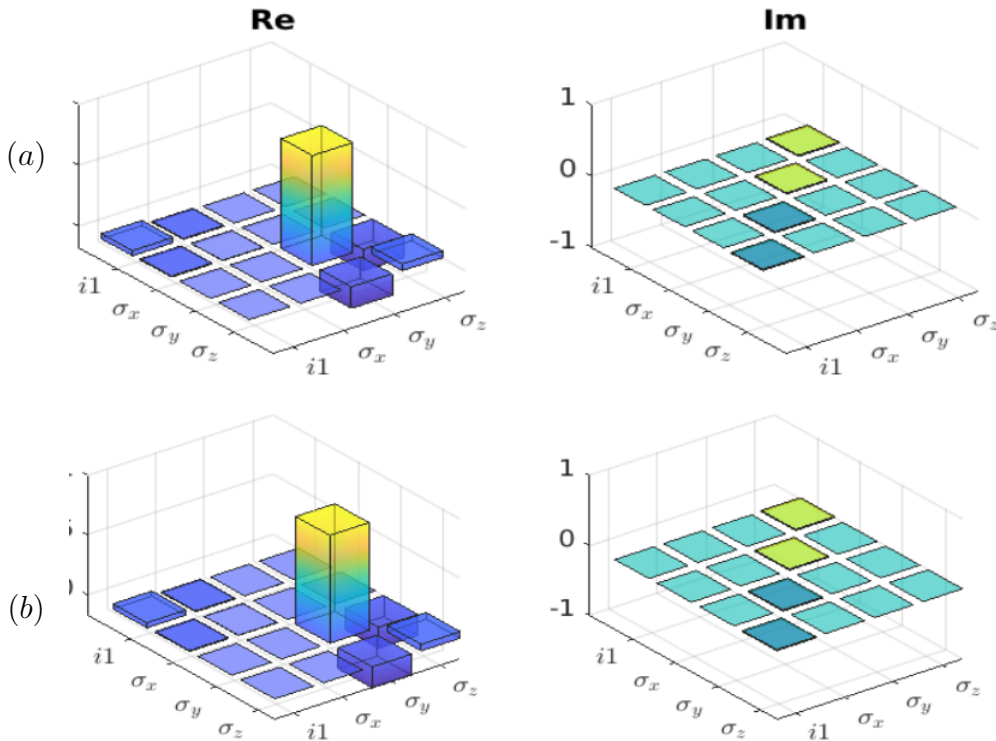


Figure 52 – Chi matrix representation of a quantum channel in the Pauli basis. The left plot ("Re") depicts the real components, while the right plot ("Im") showcases the imaginary components. Each block in these 3D plots corresponds to one of the 16 possible pairwise combinations of the Pauli matrices. The height and color gradient of each block signify the magnitude and phase of the coefficients in the Chi matrix. The matrix in (a) is the target, while (b) is the generated matrix.

7.4.2 Experimental Results

In what follows we will detail some experimental results concerning QPT in our NMR spectrometer. We experimented with the same full modulated Fourier series pulses that were examined in Section 7. This means that the tested molecule was the Chloroform and that the pulse being examined here is a Fourier series modulated pulse that is simultaneously pulsing on both qubits, even though it is a single qubit gate.

A reminder: As stated earlier, the second pulse (or decoupler pulse) uses the second qubit to correct the gate via the interacting part of the Hamiltonian (the scalar coupling). But since doing QPT in a large set of qubits scales very fast in the number of qubits, the

choice for a preliminary test was to run QPT only on the target qubit, i.e., by tracing out the second qubit. Because QPT actually retains information about noise but is not selective on what was traced out, some of the noise has provenance from the traced out qubit. It is expected, however, that most of the noise sources come from the environment and that this contribution is mostly negligible, as the control is already accounted for in the optimization algorithm discussed in Section 5. Also because we have chosen a specific operator basis that makes χ real, we have neglected the imaginary part of the matrix, for the sake of facilitating visualization, as these came out mostly zero in our tests as well.

Examining the initial and final states (already tracing out the second qubit) $\{|0\rangle\langle 0|, |1\rangle\langle 1|, |x_+\rangle\langle x_+|, |y_+\rangle\langle y_+|\}$ before and after the experimental channel, we have obtained the χ matrix in Figure 53. One can see that the theoretical matrix gives a very clean process, with elements strictly on the operator σ_y , as the desired process is exactly $Rot_y(\pi/2)$. The experimental one however is not as exact, and has contributions in both σ_x and σ_z . This is clear when one sees that in Figure 56, the state is drifted out of the target by some contribution in x and z by rotating it out in these specific directions.

$$\vec{u}_{FS} = \begin{pmatrix} 2.3834 & 0.6196 & 1.1903 & 0.3285 & 0.0992 & 0.0001 & 0.0290 & 0.0002 & 0.0873 \end{pmatrix} \quad (7.10)$$

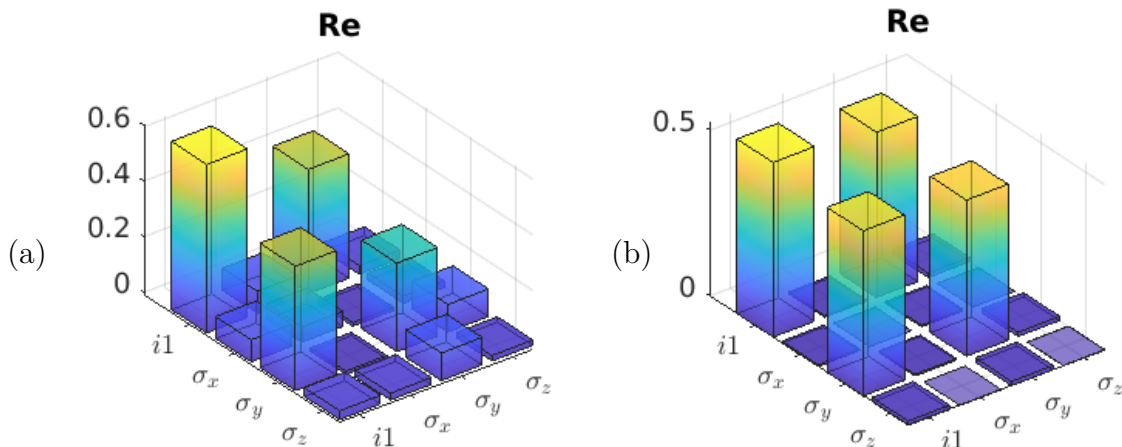


Figure 53 – Choi matrix for a $Rot_y(\pi/2)$ gate produced by a Fourier series modulated pulse. In (a) we have the Experimental Chi-matrix, retrieved by our algorithm, with the retrieved pauli and amplitude damping noise vector \vec{p} given as the last point (in time $t = 200 \mu s$ in Figure 57, while in (b) the Choi-matrix is found by straightforward QPT, as the simulation is noiseless. The found parameter vector is given in Equation (7.10)

The same test, a $Rot_y(\pi/2)$, was run on a QPT of the square pulse, i.e., the usual pulse of choice for heteronuclear systems. In this case the results are shown in Figure 54. The same effects, although in a lesser contribution, are also present on the square pulse,

as the elements out of the $i\mathbb{I}$ and σ_y elements are non-zero. One should bear in mind that some of the captured errors are also due to initial state preparation and due to the QST used to obtain the QPT Choi Matrix.

$$\vec{u}_H = \begin{pmatrix} 2.7498 & 0.0460 & 1.5157 & 0.0955 & 0.0266 & 0.0924 & 0 & 0.0001 & 0.0777 \end{pmatrix} \quad (7.11)$$

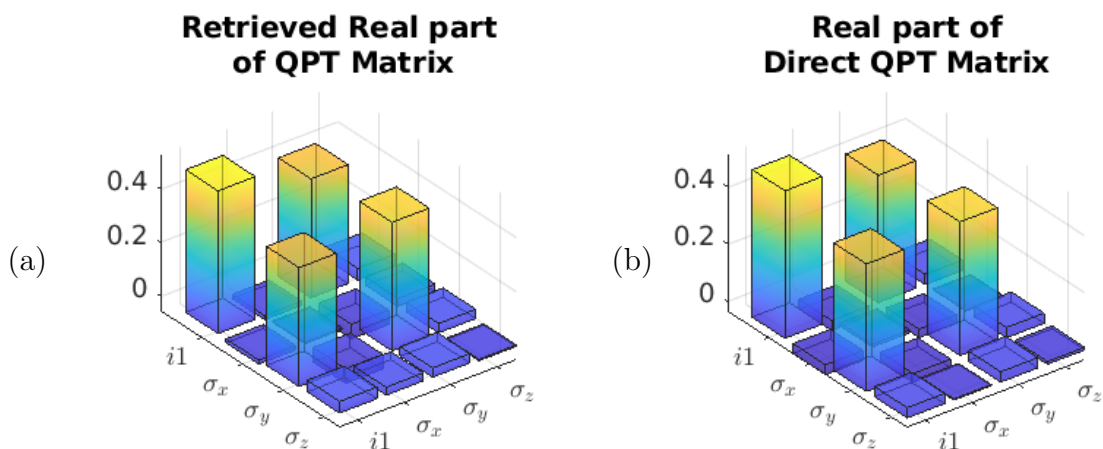


Figure 54 – Experimental Choi matrix for the square pulse applying a $Rot_y(\pi/2)$ gate. In (a) the retrieved experimental matrix, by our algorithm and (b) the Matrix by straightforward QPT with the experimental data. The parameter vector for (a) is given in Equation (7.11).

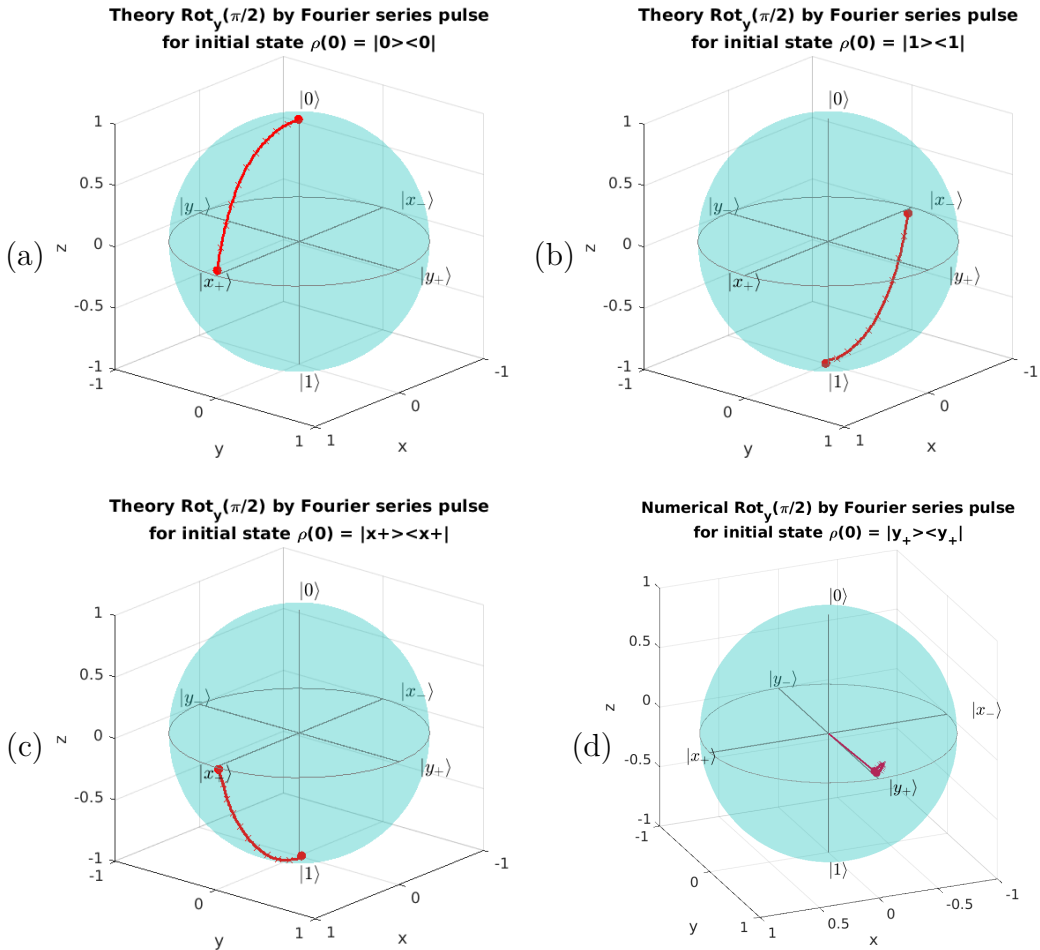


Figure 55 – QPT in time on the Bloch Sphere of theoretical Fourier series pulse, initial states are (a) $|0\rangle\langle 0|$, (b) $|1\rangle\langle 1|$, (c) $|x_+\rangle\langle x_+|$, (d) $|y_+\rangle\langle y_+|$

Contrary to expected, the square pulse has a larger noise coefficients, and this unexpected since the modulation does not oscillates, so that there should be less error on the RF source, but also because the square pulse is 20 times shorter in time than the modulated one, there is less time for interacting with the environment and for decoherence to be present. The noise coefficients however are much larger than what is usually observed in our system, getting up to almost 10%, while the expected would be around 2% or less. This observation by itself already casts some doubt our method so far. Let us examine more tests in what follows.

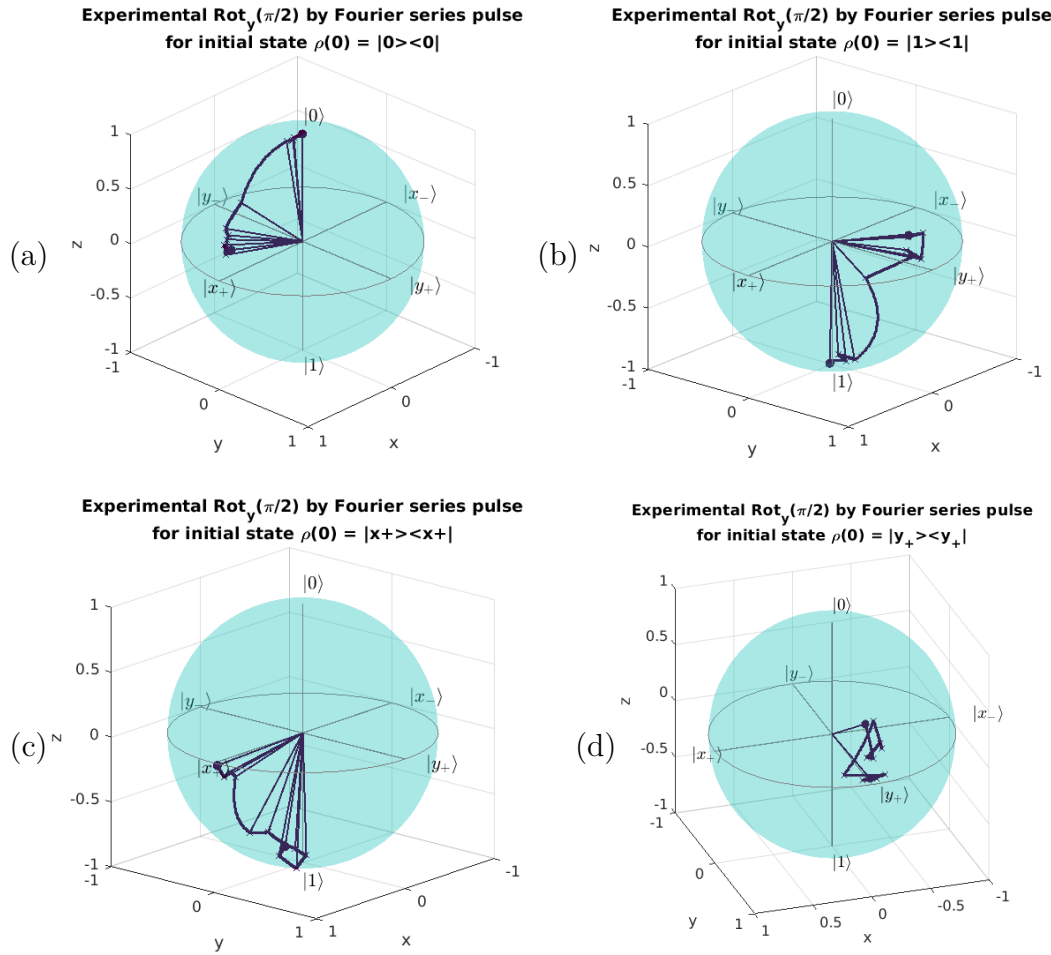


Figure 56 – Bloch Sphere of Stroboscopic measurements of experimental Fourier series pulse, initial states are (a) $|0\rangle\langle 0|$, (b) $|1\rangle\langle 1|$, (c) $|x_+\rangle\langle x_+|$, (d) $|y_+\rangle\langle y_+|$. Lines from the origin to the state represent experimental data, while lines connecting such states are only pictorial

Much has already been said about how the pulses are optimized so that at the final time τ_f the generated unitary matches the desired one, but the intermediary steps, when $t \in (0, \tau_f)$ and the chosen path in the Bloch sphere are mostly arbitrary. Then more experimental tests were conducted in order to check if the channel is respected during the pulse duration. Of course, by looking at the path on the Bloch Spheres given in Figures 55 and 56, it is clear that the desired path on the Bloch sphere is respected, for the initial states $\{|0\rangle\langle 0|, |1\rangle\langle 1|, |x_+\rangle\langle x_+|\}$, but not for $\{|y_+\rangle\langle y_+|\}$, as was already discussed in the end of Section 7.3.

To test if the channel is respected and then double check the inversion algorithm, QPT was run in the intermediate time steps. As the tested pulse had a total time of 200 μ s, we decided to measure it at each 20 μ s. We have called this technique a *Stroboscopic QPT*, as we are able to measure (or "see") the state only in a certain partition of time, in the same manner as when a stroboscopic light is used to measure the position of a particle.

To do this the state was prepared in each of the QPT basis, and then evolved for $k \cdot 20 \mu\text{s}$, where $k \in \{0, 1, \dots, 10\}$ steps. For each k the experiment was initiated once again, as measured states no longer represent the desired process after measurement. The resulting matrices and Pauli vectors \vec{p} are given in Figure 58 for each time-step k , while the plot in Figure 57 shows the evolution of noise for each of the elements in the Pauli vector \vec{p} .

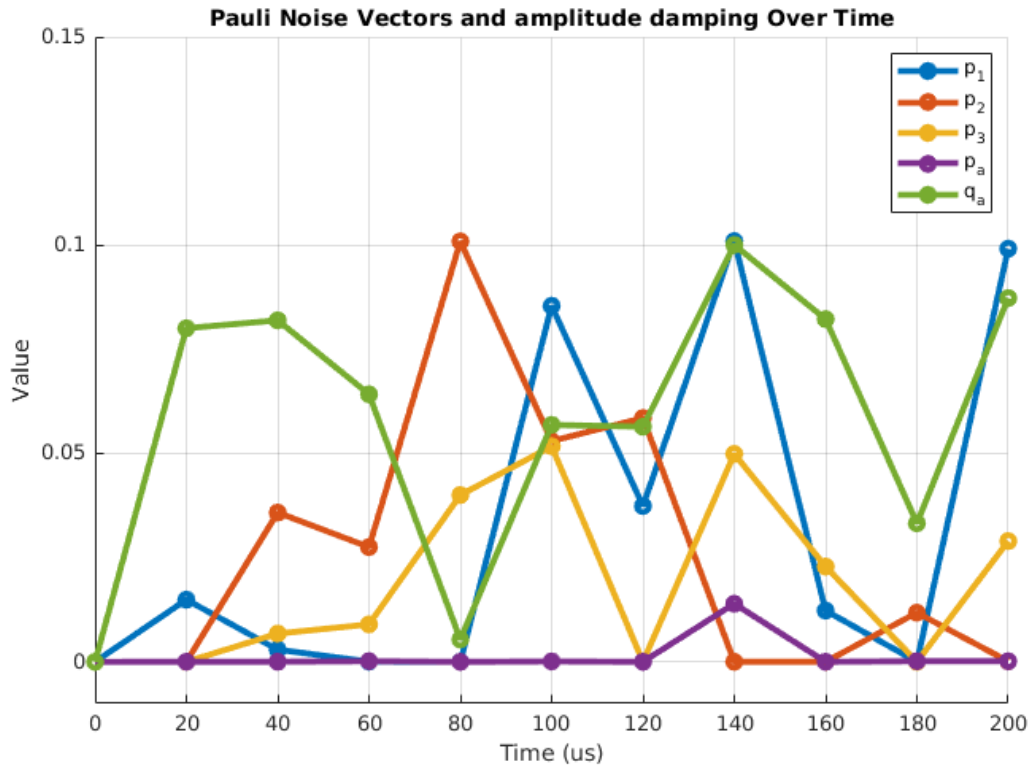


Figure 57 – Plot of retrieved Pauli Noise vector and amplitude damping for each $20 \mu\text{s}$ of the Fourier Series pulse.

Although Plots in Figures 56, 57 and 58 give an interesting visualization of the noise processes, it is clear that the variance is too big to make significant affirmations on the typical pulse noise. For what the graph in 57 shows the Pauli noises oscillates between p_x and p_y , while the noise in p_z is lower. However the amplitude damping, which we would expect to be almost zero oscillates wildly. It is highly improbable that the noise in our system reaches such levels as 10%. This indicates that our method is surely flawed, and more studies are in need to make rebuild it in a way that detects where these flaws come through and fix them. For the moment being, it is not clear how to solve this, and we conclude that the method is unreliable for experimental use.

Possibly other methods of inverting noise could be used, one such possibility would be to apply some analytical solutions to noise deconvolution as done in [35]. However such methods are quite limited in their use cases, and do not offer the generality required for NMR quantum devices. Another possibility is to find a spectral decomposition of

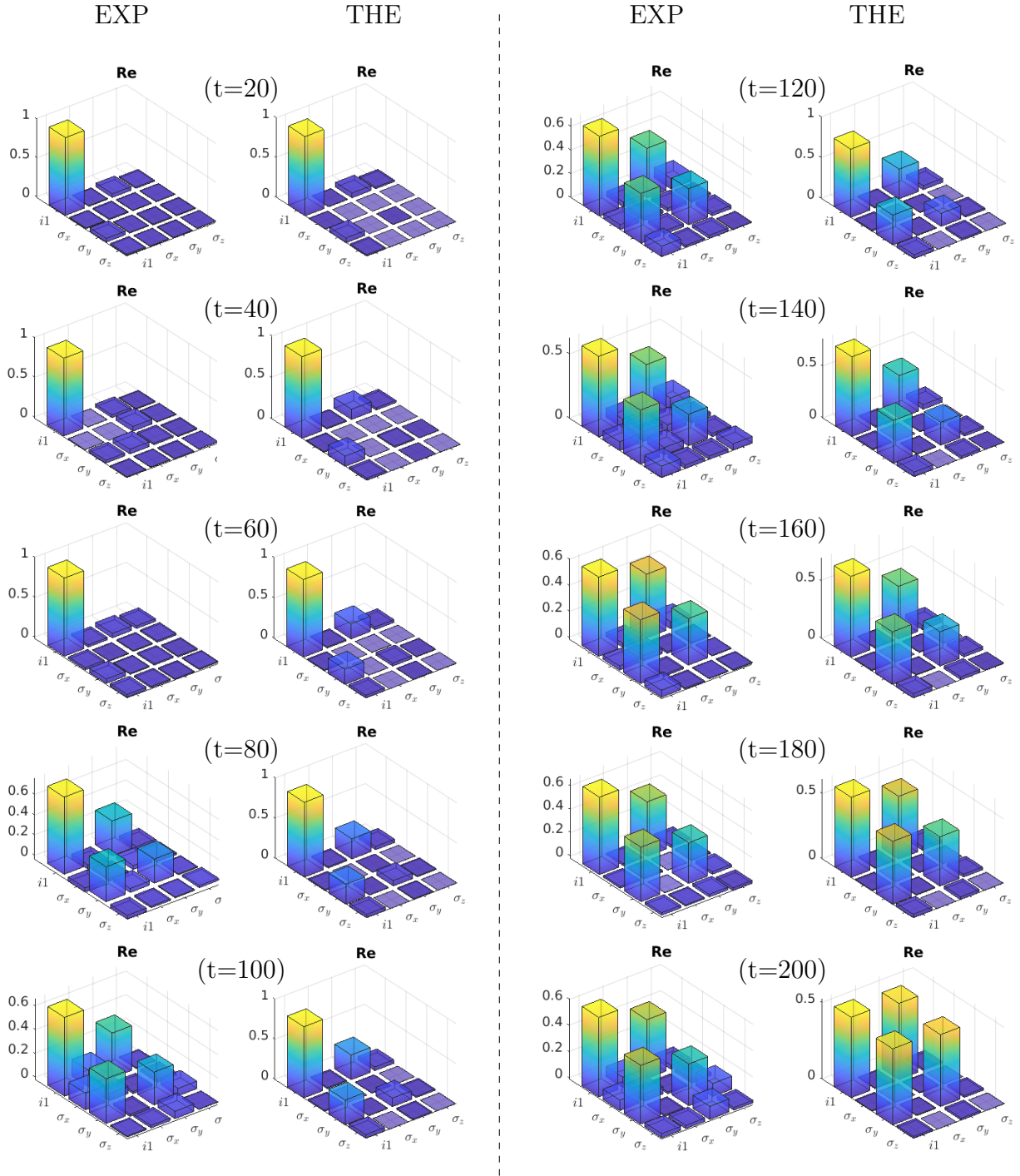


Figure 58 – Stroboscopic QPT for the Fourier Series modulated pulses, the EXP column matrices are the retrieved matrices for each QPT at the specific time, the noise parameters for each time are plotted in Figure 57. The THE column is the numerical pulse Chi matrices by straight forward QPT (not retrieved).

the typical noise, as done in [5, p.11] and apply noise spectral filters, this is a common technique in classical noise correction. Another solution also proposed and implemented in Reference [5] is to estimate ad-hoc complex parameters for the hamiltonian, and then these can be incorporated in the simulation, making it non-hermitian. All of these possible solutions are out of the scope of this work due to deadline limitations.

We end the discussion by suggesting how to implement noise via Choi matrix noise estimation in the next subsection, as if the problem of large variance above is solved the next step would be a natural way forward.

7.4.3 Adding noise to the control optimization

The same algorithm made to optimize the pulses was edited so that now one can input noise in this same parametrization, i.e., as a vector $\vec{p} = (p_x, p_y, p_z, p_A, q_A)$. To do this the loss function can no longer be the difference between the generated unitary and the target unitary as in Equation (6.9). As the generated pulse assumes that the system is noisy, and will not produce a perfect unitary evolution, so the $\chi^{(2)}(U_g, U_t)$ is not a good choice anymore. To solve this a new optimization function has to be defined, there are some possibilities: 1) Because the noise is low, then we can guarantee that the larger eigenvalue λ_{\max} of the Choi matrix will correspond to the unitary part of the process, even if it is $\lambda_{\max} \leq 1$. So even if the process is noisy, one could choose to select the unitary part of the process, by finding λ_{\max} , and the associated eigenvector \vec{n}_{\max} so that $U_g = \vec{n}_{\max} \cdot \vec{\sigma}$, and then take the difference $\chi^{(2)}(U_g, U_t)$ as done has been done earlier to the unitary case. Option 2) is to optimize on the states. However, to avoid that the pulse becomes state specific, regarding the discussion above, the natural choice to have maximal information was to build an optimization function that measures the distance between an ensemble of ensembles, where multiple MUB basis pass through our channel and the difference is taken for all of them. A third option 3) is to estimate complex parameters in the hamiltonian, as done in [5, p.24], this can be done by use of Q-Ctrl's company software tools, and then the full estimated hamiltonian can be used in the direct estimation of Equation (6.11).

Because the first choice becomes quite computationally consuming for larger systems, as it is known that finding eigenvalues has a computational complexity of $\mathcal{O}(n^3)$, while the second relies on matrix multiplication, which is not as computationally intense, we have opted for the second approach ².

So the method goes as follows: Get the set of the necessary MUBs for your Hilbert space B , the size of this set has to be $N = d^2$, as discussed in Section 2.5, where d is the dimension of the Hilbert space. For each state in this set pass it through the target unitary channel, resulting in the set $O_t = \{U_t \rho U_t^\dagger | \rho \in B\}$. Now find a RF modulation that generates an unitary gate U_g , and apply the composition of noise channels to U_g as in Equation (7.4), this results in the generated output states set $O_g = \{\mathcal{E}_{\text{noise}}(U_g \rho U_g^\dagger) | \rho \in B\}$. Calculate the elementwise difference of the states in O_t and O_g

² The third option seemed also quite promising, but was left for a possible future research project.

$$\chi^{(3)}(U_g, U_t, \vec{p}) = \sum_{\rho \in B} \sum_{nm} \left[Re(U_t \rho U_t^\dagger - \mathcal{E}_{\text{noise}}(U_g \rho U_g^\dagger)) \right]_{nm}^2 + \left[Im(U_t \rho U_t^\dagger - \mathcal{E}_{\text{noise}}(U_g \rho U_g^\dagger)) \right]_{nm}^2 \quad (7.12)$$

Use a minimization algorithm that minimizes $\chi^{(3)}$, by variations on U_g , i.e., on the Fourier series parameters as in Equation (6.11).

We can now unite both discussions on pulse modulation and the reverse search algorithm for QPT. By finding the typical noise of our spectrometer, it is possible to add such noise to the simulation and then making a more robust model, which would in turn lead to pulses that are more robust to the noise. Note that the type of noise in our system can be from multiple sources, as the noise will be specific to the molecule being used, the solvent used in the sample, the quality of the RF generator, and the homogeneity of the B_0 field (which varies week by week in a given experiment and is the less constant factor in this list). Nonetheless, the algorithm built above is agnostic to the source of noise, as it labels all noise in the same 4 types listed in Section 2.5.

Ideally, whenever one has a good shimming and has found the typical power for the right time for $Rot_y(\pi)$ square pulse. One can then run some (square) pulses on MUB states and run QPT on them to find \vec{p} . Then, the Fourier coefficient optimization can be run (taking tens of minutes), and have efficient pulses ready to use. This whole process may take from 5 h to 12 h to be completed, as the initial shimming is the most time consuming part.

However, as discussed earlier, the noise parameter estimation problem still has to be solved, and although the noise pulse optimization is ready to use, we shall refrain on saying more on the subject and finally proceed to the conclusions of this work.

Part IV

Conclusion and further research

Conclusion and Future Research

Conclusion

This thesis has shown some particularities in the field of qubit control in NMR Quantum Information Protocols. Central to our achievements is the development and successful implementation of an optimization algorithm. This algorithm, designed to optimize Fourier series coefficients of RF modulation, inspired by the methods introduced in Reference [44], has proven instrumental in enhancing the precision and efficiency of qubit manipulation, mostly for homonuclear systems. The implementation of this algorithm not only demonstrates the capability to refine quantum control mechanisms but also reinforces the potential of algorithmic approaches in complex quantum systems, and should be later tested for larger systems with multiple qubits.

One of the most intriguing aspects of this research has been the exploration and understanding of out-of-resonance pulsing. Our findings in this area have not only expanded our knowledge of quantum dynamics but have also provided valuable insights into the subtleties of qubit behavior under these conditions. We found that, contrary to intuition, there is no preference for a specific frequency in a homonuclear system, as the optimization algorithm showed no statistical bias. These insights have interesting implications for future quantum experiments and technologies, potentially leading to more robust and versatile quantum computing platforms at the UFABC group, or any other NMR Quantum Information Processing group, for that matter. The same methods can be adapted to other platforms as in nitrogen vacancy centers in diamonds or superconducting qubits.

Following these significant advancements, our focus shifted to the study of QPT in NMR spectroscopy. The challenges and intricacies of QPT were met with a comprehensive approach, both in theoretical understanding with practical experimentation. Our research contributed to a comprehension of the limits of algorithmic approaches to noise discovery within these systems. The results of this exploration have not validated our algorithmic approach to QPT, but have shown interesting paths for further investigation and improvement, discussed below.

In conclusion, this dissertation stands as a testament to the power of innovative algorithmic strategies in advancing the field of Quantum Information and control protocols.

The successful optimization of qubit control through Fourier series coefficients, the novel insights into out-of-resonance pulsing, and the in-depth analysis of QPT collectively represent a contribution to our understanding and capabilities in quantum information science. As this research journey concludes, it leaves a foundation for future explorations and advancements in the ever-evolving and fascinating world of quantum technology in the near time.

The remainder of the conclusion is devoted to suggestions on further research directions using machine learning, and a possibility of a repository to facilitate the use of our optimizations.

Machine learning Quantum control assistant

In view of the previous discussion, it should be clear that there are many methods for qubit control in NMR that rely on well founded theory, both physical and mathematical. Nonetheless, all theory should be, in principle, steered by experimental practice, if its goals are to create science of practical use. Sometimes the relation between theory and practice is not obvious and requires a lot of intuition and experience. However, when time is of the matter, it may be impossible to evaluate what are the relevant variables, under these circumstances other tools are available to reduce time costs, we propose a *machine learning* (ML) facilitator to solve this problem.

Machine learning has received a lot of attention in recent years, given its huge success with large sets of data [18, p.18]. Despite appearing as black boxes, there is much knowledge that can be gained by the use of such tools. It surely is not an overstatement to say that data analysis together with machine learning are a set of algorithms whose purpose is to find correlations where they are not evident, and we propose to use it in this way.

For future research, we intend to build a *Neural Network* (NN) that takes as input a target unitary U_t and gives as output the optimal metaparameters of the pulse optimization discussed in the prior sections. By “meta parameters” we mean, parameters that are chosen prior to the pulse optimization, that is: pulse time τ_f ; number of points np ; maximum coefficients in the Fourier series S_A, S_P ; the ζ_l that bound the amplitude in Equation (6.10); Offset/detuning of the pulse; pulse maximum power; etc.

The Neural Net would then be trained in both numerical data and experimental data, making it more sensitive to the limitations of our laboratory setup, and therefore designed to give experimental parameters that are tailor-made for our local purposes. To incorporate experimental data to the training, we plan to run another long battery of experiments, this time with a larger number of variations in parameters. Ideally, this kind of training can be done in what is called in the area as *on-line* training, where the NN

is interacts continuously with the spectrometer, suggesting and testing data. This would make the learning specific to the spectrometer the NN is learning from.

Nonetheless, such experimental data is usually limited, given that its acquisition is very much time-consuming, so that the use of numerical data to enlarge the data set is common practice in this matter. The limits of how much the data set must be leveraged with numerical results is still to be tested. To incorporate this data in the training is straightforward, as one could train with a loss function such as

$$\mathcal{L}(U_t, \tau_f, np, S_A, S_P, \zeta_1, \zeta_2, \text{offset}, \text{power}) = \frac{\alpha_{\text{ex}} \cdot \chi_{\text{ex}}^2 + \alpha_{\text{num}} \cdot \sum^M \chi_{\text{num}}^2}{\alpha_{\text{ex}} + \alpha_{\text{num}}}, \quad (7.13)$$

where the α terms are determined on train tests. Together with this loss function, other weights can be added, for example: one could set the limit of depth of the desired quantum algorithm, e.g. τ_{tot} and M_G gates, and restrict that the modulated gates should be always smaller than a fraction of the total time, i.e.,

$$\mathcal{L}_{\text{t-bound}} = \max(0, \tau_f - \tau_{\text{tot}}/M_G),$$

so a final loss function may always be constructed to be

$$\mathcal{L}_{\text{tot}} = \mathcal{L} + \lambda \sum^{N_{\text{bound}}} \mathcal{L}_{\text{bounds}}. \quad (7.14)$$

making the training very goal oriented.

Machine learning quantum process tomography

Following this topic and the discussion in Section 2.5 and 7.4, the reader may have concluded that a deterministic algorithm is not flexible enough to deal with such a large set of parameters and variable experimental practice. For this reason we have tested a machine learning algorithm for the same inverse problem, i.e., given a Chi-Matrix, find the noise parameter vector that generates such Chi-Matrix.

The intuition behind such use is that, by providing enough data, the algorithm could learn the noise types. The simulation is the same as discussed in Section 7.4, but the loss function has to be changed. As we hoped to use QPT from experimental data to retrieve the noise. So the Machine Learning algorithm would receive an experimental Chi matrix as input, and then should output the noise parameters that generated this matrix. We built a large data-set of 10^4 , \vec{u} , parameter vectors and 10^4 , 4x4 Chi matrices χ , resulting from such vector inputs. So the learning was as follows:

1. Input a χ_{in} matrix, possibly flattened, in a dense neural network. So the input layer has 32 entries, 16 for the real part of the flattened χ_{in} and the other 16 for the imaginary part.
2. The neural net should output a 9 entry vector \vec{u}_{out} .
3. This vector should be used to produce a χ_{out} Chi matrix, by direct QPT
4. Calculate the loss function by finding the distance between χ_{in} and χ_{out} .
5. update the neural network weights and biases so that the loss function minimizes.

The desired loss function could then be $\chi^{(2)}(\chi_{\text{in}}, \chi_{\text{out}})$ as defined in Equation (6.9). However, one could introduce an extra term called a *regularization*, to force a certain output vector type, by providing some smoothing to the parameter space and enhance fitting [24, p.57], so that the new loss function becomes

$$\mathcal{L}_{\text{total}}(\chi_{\text{in}}, \chi_{\text{out}}, \vec{u}_{\text{in}}, \vec{u}_{\text{out}}) = \chi^{(2)}(\chi_{\text{in}}, \chi_{\text{out}}) + \mathcal{L}(\vec{u}_{\text{in}}, \vec{u}_{\text{out}}) \quad (7.15)$$

$$= \chi^{(2)}(\chi_{\text{in}}, \chi_{\text{out}}) + \|\vec{u}_{\text{in}} - \vec{u}_{\text{out}}\|^2. \quad (7.16)$$

Because both functions that are summed up are locally convex, the optimization should work. However this is not what we have found. This algorithm was built, and we tested many possibilities: either with or without regularization; changing architectures to (Convolutional Neural Networks) CNN , or even Autoencoders. None of these options where enough to make the net loss function converge. Some initial minimization is present, but the final values are far from anything but a fit. This makes the resulting neural network too unreliable.

One possible issue is that the problem is highly non invertible, and so searching for a inverse algorithm in this manner would not work. The problem for the invertibility is discussed in Section 7.4, and the main argument is that infinite different angles and noises would provide the same Chi-matrix, as one can see in Equation (7.8). The regularization above was a failed solution.

Another way would be to reduce the domain space. One could run a Stroboscopic QPT, and build a Neural Network that must pass through certain time checkpoint Chi-matrices in training. So that instead of trying to find the \vec{u}_{in} for the whole process, the Net could partition the total time τ_f in N parts and set checkpoints at each $\Delta t = \tau_f/N$ to check if the process Chi matrix makes sense in all checkpoints, i.e., it should produce the Chi matrix of each $\chi(n\Delta t)$, for $n \in \{0, \dots, N\}$. This would restrict the domain of parameters, as only the processes that passed through specific checkpoints on the path on the Bloch Sphere would be the right ones.

One could then build a loss function as

$$\mathcal{L} = \sum_{n=0}^N \chi^{(2)}(\chi_{\text{in}}(n\Delta t), \chi_{\text{out}}(n\Delta t)). \quad (7.17)$$

Or instead rely on a Neural Network architecture that can learn dynamical processes such as Recurrent Neural Networks. If this solution suffices remains to be seen by further research.

Repository

If the endeavor of creating a neural net assistant for experimental qubit control, that is tailor-made for each laboratory spectrometer, gives satisfactory results. Then, the next step would be to write documentation to the code, and a walk-through of how to, and which, experimental data is necessary to train the neural net model. Our optimization code (which is already more than 4 thousand lines long), will be uploaded to a GitHub repository, together with the documentation and experimental walk through, where it can be downloaded and the neural net trained to the specific purposes of the local lab. The main goal is to make it as easily accessible so that it is as “plug and play” as possible. This approach surely incentivizes use and, if made open-source, makes it easy for community and user contributions.

We hope to build an algorithm that saves time spent in the laboratory tuning and calibrating pulses, opening more time to actual research. This idea is mostly inspired by the paper from the Q-Ctrl group [5] that provides very similar services on commercial premisses.

Finally, our algorithm, focusing on the optimization of Fourier series coefficients in RF modulation, can greatly enhance qubit manipulation precision in homonuclear systems. Additionally, our investigation into out-of-resonance pulsing has yielded new insights into quantum dynamics, challenging previous assumptions. While our exploration into QPT encountered challenges, it has opened promising paths for future research. Overall, this work not only contributes to the quantum information science field but also paves the way for further innovation, through any of these discussed ventures.

Bibliography

- [1] Kartiek Agarwal and Ning Bao. “Toy model for decoherence in the black hole information problem”. In: *Physical Review D* 102.8 (Oct. 2020). ISSN: 2470-0029. DOI: [10.1103/physrevd.102.086017](https://doi.org/10.1103/physrevd.102.086017). URL: <http://dx.doi.org/10.1103/PhysRevD.102.086017>.
- [2] E. Akkermans, P. E. Wolf, and R. Maynard. “Coherent Backscattering of Light by Disordered Media: Analysis of the Peak Line Shape”. en. In: *Physical Review Letters* 56.14 (Apr. 1986). Number: 14, pp. 1471–1474. DOI: [10.1103/PhysRevLett.56.1471](https://doi.org/10.1103/PhysRevLett.56.1471). (Visited on 03/07/2023).
- [3] Eric Akkermans and Gilles Montambaux. *Mesoscopic Physics of Electrons and Photons*. Cambridge University Press, 2007.
- [4] George B. Arfken, Hans J. Weber, and Frank E. Harris. *Mathematical Methods for Physicists*. Elsevier, 2013. DOI: [10.1016/b978-0-12-384654-9.00030-x](https://doi.org/10.1016/b978-0-12-384654-9.00030-x).
- [5] Harrison Ball et al. “Software tools for quantum control: improving quantum computer performance through noise and error suppression”. en. In: *Quantum Science and Technology* 6.4 (Oct. 2021), p. 044011. DOI: [10.1088/2058-9565/abdca6](https://doi.org/10.1088/2058-9565/abdca6). URL: <https://iopscience.iop.org/article/10.1088/2058-9565/abdca6> (visited on 07/19/2023).
- [6] Tiago Barbin. “Avanços teóricos e experimentais em Termodinâmica Quântica”. pt. PhD thesis. UFABC, 2016.
- [7] G. Benenti and G. Casati. *Principles of Quantum Computation*. Publication Title: Fundamentals of Quantum Optics and Quantum Information. 2007. ISBN: 978-981-256-345-3. DOI: [10.1007/978-3-540-34572-5_9](https://doi.org/10.1007/978-3-540-34572-5_9).
- [8] Gaurav Bhole et al. “Experimental and Theoretical Analysis of Drag Forces in Micromechanical-Beam Arrays”. en. In: *Physical Review Applied* 13.3 (Mar. 2020), p. 034003. DOI: [10.1103/PhysRevApplied.13.034003](https://doi.org/10.1103/PhysRevApplied.13.034003). URL: <https://link.aps.org/doi/10.1103/PhysRevApplied.13.034003> (visited on 07/01/2023).
- [9] Felix Binder et al., eds. *Thermodynamics in the Quantum Regime: Fundamental Aspects and New Directions*. Cham: Springer International Publishing, 2018. ISBN: 978-3-319-99045-3. DOI: [10.1007/978-3-319-99046-0](https://doi.org/10.1007/978-3-319-99046-0).

- [10] Dolev Bluvstein et al. “Logical quantum processor based on reconfigurable atom arrays”. en. In: *Nature* (Dec. 2023). ISSN: 0028-0836, 1476-4687. DOI: [10.1038/s41586-023-06927-3](https://doi.org/10.1038/s41586-023-06927-3). URL: <https://www.nature.com/articles/s41586-023-06927-3> (visited on 01/05/2024).
- [11] Heinz-Peter Breuer and Francesco Petruccione. *The Theory of Open Quantum Systems*. Oxford University PressOxford, Jan. 2007. DOI: [10.1093/acprof:oso/9780199213900.001.0001](https://doi.org/10.1093/acprof:oso/9780199213900.001.0001).
- [12] Davide Candoli et al. “PULSEE: A software for the quantum simulation of an extensive set of magnetic resonance observables”. en. In: *Computer Physics Communications* 284 (Mar. 2023), p. 108598. DOI: [10.1016/j.cpc.2022.108598](https://doi.org/10.1016/j.cpc.2022.108598). URL: <https://linkinghub.elsevier.com/retrieve/pii/S0010465522003174> (visited on 03/11/2023).
- [13] H. S. Carlaw. “A historical note on Gibbs’ phenomenon in Fourier’s series and integrals”. In: *Bulletin of the American Math. Soc* 8 (31 Oct. 1925).
- [14] Y.-W. Cho et al. “Highly efficient optical quantum memory with long coherence time in cold atoms”. en. In: *Optica* 3.1 (Jan. 2016). Number: 1, p. 100. DOI: [10.1364/OPTICA.3.000100](https://doi.org/10.1364/OPTICA.3.000100). URL: <https://opg.optica.org/abstract.cfm?URI=optica-3-1-100> (visited on 11/07/2022).
- [15] Michael A. Nielsen & Isaac L. Chuang. *Quantum Computation and Quantum Information*. 10th. Vol. 15. Cambridge University Press, June 2011. DOI: [10.1007/s100510051166](https://doi.org/10.1007/s100510051166).
- [16] Claude Cohen-Tannoudji, Bernard Diu, and Franck Laloë. *Quantum mechanics, volume 1*. en. 2nd ed. Berlin, Germany: Blackwell Verlag, Oct. 2019.
- [17] John B. Conway. *A Course in Functional Analysis*. 2nd ed. Vol. 96. Graduate Texts in Mathematics. New York: Springer-Verlag, 1990, p. 399. ISBN: 978-0-387-97245-9.
- [18] Anna Dawid et al. “Modern applications of machine learning in quantum sciences Abstract In these Lecture Notes , we provide a comprehensive introduction to the most recent ad- In memory of Peter Wittek”. In: (2022).
- [19] Sebastian Deffner and Steve Campbell. *Quantum Thermodynamics: An introduction to the thermodynamics of quantum information*. Morgan & Claypool Publishers, 2019.
- [20] Kabir Dubey. *The Fourier Uncertainty Principles*. Lecture notes. 2021. URL: <https://math.uchicago.edu/~may/REU2021/REUPapers/Dubey.pdf>.
- [21] N. Dupont et al. “Quantum State Control of a Bose-Einstein Condensate in an Optical Lattice”. en. In: *PRX Quantum* 2.4 (Oct. 2021), p. 040303. DOI: [10.1103/PRXQuantum.2.040303](https://doi.org/10.1103/PRXQuantum.2.040303). URL: <https://link.aps.org/doi/10.1103/PRXQuantum.2.040303> (visited on 10/11/2023).

- [22] Robert Martin Eisberg and Robert Resnick. *Quantum physics of atoms, molecules, solids, nuclei and particles; 2nd ed.* New York, NY: Wiley, 1985. URL: <https://cds.cern.ch/record/105889>.
- [23] Evan M. Fortunato et al. “Design of strongly modulating pulses to implement precise effective Hamiltonians for quantum information processing”. en. In: *The Journal of Chemical Physics* 116.17 (May 2002), pp. 7599–7606. ISSN: 0021-9606, 1089-7690. DOI: [10.1063/1.1465412](https://doi.org/10.1063/1.1465412). URL: <https://pubs.aip.org/jcp/article/116/17/7599/185235/Design-of-strongly-modulating-pulses-to-implement> (visited on 12/06/2023).
- [24] Aurélien Géron. *Hands-on Machine Learning with Scikit-Learn, Keras, and TensorFlow (2019, O’reilly)*. Publication Title: Hands-On Machine Learning with R. O’Reilly Media, 2017. ISBN: 978-1-4920-3264-9.
- [25] G. Balieiro Gomes et al. “Quantum decoherence effects in neutrino oscillations at DUNE”. In: *Physical Review D* 100.5 (Sept. 2019). ISSN: 2470-0029. doi: [10.1103/physrevd.100.055023](https://doi.org/10.1103/physrevd.100.055023). URL: <http://dx.doi.org/10.1103/PhysRevD.100.055023>.
- [26] E. Hewitt and R.E Hewitt. “The Gibbs-Wilbraham phenomenon: An episode in fourier analysis”. In: *Arch. Hist. Exact Sci.* (21 1979). URL: <https://doi.org/10.1007/BF00330404>.
- [27] Jack D. Hidary. *Quantum Computing: An Applied Approach*. Publication Title: Quantum Computing: An Applied Approach. 2021. ISBN: 978-3-030-83273-5. doi: [10.1007/978-3-030-83274-2](https://doi.org/10.1007/978-3-030-83274-2).
- [28] Dan Iverson et al. *VnmrJ User Programming*. A 0708. For Varian, Inc. Innova and Mercury/plus NMR Systems with VnmrJ 2.2MI software installed. Varian, Inc. 3120 Hansen Way, Palo Alto, California 94304, May 2008. URL: <https://www.agilent.com/library/usermanuals/public/0199937900a.pdf>.
- [29] Jonathan A. Jones. “Quantum Computing with NMR”. en. In: *Progress in Nuclear Magnetic Resonance Spectroscopy* 59.2 (Aug. 2011). arXiv:1011.1382 [quant-ph], pp. 91–120. doi: [10.1016/j.pnmrs.2010.11.001](https://doi.org/10.1016/j.pnmrs.2010.11.001). URL: <http://arxiv.org/abs/1011.1382> (visited on 07/01/2023).
- [30] Navin Khaneja et al. “Optimal control of coupled spin dynamics: design of NMR pulse sequences by gradient ascent algorithms”. en. In: *Journal of Magnetic Resonance* 172.2 (Feb. 2005). Number: 2, pp. 296–305. doi: [10.1016/j.jmr.2004.11.004](https://doi.org/10.1016/j.jmr.2004.11.004). URL: <https://linkinghub.elsevier.com/retrieve/pii/S1090780704003696> (visited on 12/17/2022).

- [31] Christiane P. Koch et al. “Quantum optimal control in quantum technologies. Strategic report on current status, visions and goals for research in Europe”. en. In: *EPJ Quantum Technology* 9.1 (Dec. 2022). arXiv:2205.12110 [quant-ph], p. 19. DOI: [10.1140/epjqt/s40507-022-00138-x](https://doi.org/10.1140/epjqt/s40507-022-00138-x). URL: <http://arxiv.org/abs/2205.12110> (visited on 10/10/2023).
- [32] Andrew J. Larkoski. “General analysis for observing quantum interference at colliders”. In: *Physical Review D* 105.9 (May 2022). ISSN: 2470-0029. DOI: [10.1103/physrevd.105.096012](https://doi.org/10.1103/physrevd.105.096012). URL: <http://dx.doi.org/10.1103/PhysRevD.105.096012>.
- [33] Michel Le Bellac. *Quantum Physics*. Ed. by Patricia de Forcrand-Millard. Cambridge University Press, Mar. 2006. ISBN: 9781107602762. DOI: [10.1017/cbo9780511616471](https://doi.org/10.1017/cbo9780511616471). URL: <http://dx.doi.org/10.1017/CBO9780511616471>.
- [34] Malcolm H. Levitt. *Spin dynamics: basics of nuclear magnetic resonance*. 2nd ed. Wiley, 2008.
- [35] Stefano Mangini, Lorenzo Maccone, and Chiara Macchiavello. “Qubit noise deconvolution”. en. In: *EPJ Quantum Technology* 9.1 (Dec. 2022). arXiv:2112.03043 [quant-ph], p. 29. DOI: [10.1140/epjqt/s40507-022-00151-0](https://doi.org/10.1140/epjqt/s40507-022-00151-0). URL: <http://arxiv.org/abs/2112.03043> (visited on 07/04/2023).
- [36] M. Mohseni and D. A. Lidar. “Direct Characterization of Quantum Dynamics”. en. In: *Physical Review Letters* 97.17 (Oct. 2006), p. 170501. DOI: [10.1103/PhysRevLett.97.170501](https://doi.org/10.1103/PhysRevLett.97.170501). URL: <https://link.aps.org/doi/10.1103/PhysRevLett.97.170501> (visited on 10/17/2023).
- [37] M. Mohseni, A. T. Rezakhani, and D. A. Lidar. “Quantum Process Tomography: Resource Analysis of Different Strategies”. en. In: *Physical Review A* 77.3 (Mar. 2008). arXiv:quant-ph/0702131, p. 032322. DOI: [10.1103/PhysRevA.77.032322](https://doi.org/10.1103/PhysRevA.77.032322). URL: <http://arxiv.org/abs/quant-ph/0702131> (visited on 10/17/2023).
- [38] James D. Murray. *Mathematical Biology 1: An Introduction*. 3rd. Interdisciplinary Applied Mathematics. Springer, 2007. ISBN: 0387952233; 9780387952239; 9780387224374; 0387224378.
- [39] Duff Neill and Wouter J. Waalewijn. “Entropy of a Jet”. In: *Physical Review Letters* 123.14 (Sept. 2019). ISSN: 1079-7114. DOI: [10.1103/physrevlett.123.142001](https://doi.org/10.1103/physrevlett.123.142001). URL: <http://dx.doi.org/10.1103/PhysRevLett.123.142001>.
- [40] Ivan S. Oliveira. *NMR quantum information processing*. en. 1st ed. Amsterdam ; London: Elsevier, 2007. ISBN: 978-0-444-52782-0.
- [41] Alan V. Oppenheim, Alan S. Willsky, and S. Hamid Nawab. *Signals and System*. 2nd. Prentice Hall, 1996. ISBN: 0-13-814757-4.

- [42] J. P. S. Peterson et al. “Experimental demonstration of information to energy conversion in a quantum system at the Landauer limit”. en. In: *Proceedings of the Royal Society A: Mathematical, Physical and Engineering Sciences* 472.2188 (Apr. 2016). Number: 2188, p. 20150813. DOI: [10.1098/rspa.2015.0813](https://doi.org/10.1098/rspa.2015.0813). URL: <https://royalsocietypublishing.org/doi/10.1098/rspa.2015.0813> (visited on 03/05/2023).
- [43] John P. S. Peterson et al. “Experimental characterization of a spin quantum heat engine”. en. In: *Physical Review Letters* 123.24 (Dec. 2019). arXiv:1803.06021 [cond-mat, physics:quant-ph], p. 240601. DOI: [10.1103/PhysRevLett.123.240601](https://doi.org/10.1103/PhysRevLett.123.240601). URL: [http://arxiv.org/abs/1803.06021](https://arxiv.org/abs/1803.06021) (visited on 05/15/2023).
- [44] John P.S. Peterson, Roberto S. Sarthour, and Raymond Laflamme. “Enhancing Quantum Control by Improving Shaped-Pulse Generation”. en. In: *Physical Review Applied* 13.5 (May 2020). Number: 5, p. 054060. DOI: [10.1103/PhysRevApplied.13.054060](https://doi.org/10.1103/PhysRevApplied.13.054060). URL: <https://link.aps.org/doi/10.1103/PhysRevApplied.13.054060> (visited on 11/30/2022).
- [45] John Preskill. “Quantum Computing in the NISQ era and beyond”. In: *Quantum* 2 (Aug. 2018), p. 79. DOI: [10.22331/q-2018-08-06-79](https://doi.org/10.22331/q-2018-08-06-79).
- [46] C. A. Ryan et al. “Liquid-state nuclear magnetic resonance as a testbed for developing quantum control methods”. en. In: *Physical Review A* 78.1 (July 2008). Number: 1, p. 012328. DOI: [10.1103/PhysRevA.78.012328](https://doi.org/10.1103/PhysRevA.78.012328). URL: <https://link.aps.org/doi/10.1103/PhysRevA.78.012328> (visited on 03/16/2023).
- [47] J. J. Sakurai. *Modern Quantum Mechanics (Revised Edition)*. 1st ed. Addison Wesley, Sept. 1993. ISBN: 0201539292. URL: <http://www.worldcat.org/isbn/0201539292>.
- [48] Roberto S Sarthour, Juan D Bulnes, and Salvador B Belmonte. “Computac^{ao} Qu^{ntica} via Resson^{ncia} Magn^{tica} Nuclear”. pt. In: (2002), p. 65.
- [49] E. SCHRÖDINGER. “Are there Quantum Jumps?: PART II”. In: *The British Journal for the Philosophy of Science* 3.11 (Nov. 1952), pp. 233–242. ISSN: 1464-3537. DOI: [10.1093/bjps/iii.11.233](https://doi.org/10.1093/bjps/iii.11.233). URL: <http://dx.doi.org/10.1093/bjps/iii.11.233>.
- [50] Marlan Scully and M Suhail Zubairy. *Quantum optics*. 1997.
- [51] R. Shankar. *Principles of Quantum Mechanics*. Springer US, 1994. ISBN: 9781475705768. DOI: [10.1007/978-1-4757-0576-8](https://doi.org/10.1007/978-1-4757-0576-8). URL: <http://dx.doi.org/10.1007/978-1-4757-0576-8>.
- [52] Carlos Henrique da Silva Vieira. “Investigações Experimentais sobre Flutuações Incertezas e Limites em Termodinâmica Quântica”. PhD thesis. Santo André, SP: Universidade Federal do ABC, Jan. 2023.

- [53] Giacomo Torlai et al. “Quantum process tomography with unsupervised learning and tensor networks”. en. In: *Nature Communications* 14.1 (May 2023), p. 2858. DOI: [10.1038/s41467-023-38332-9](https://doi.org/10.1038/s41467-023-38332-9). URL: <https://www.nature.com/articles/s41467-023-38332-9> (visited on 07/22/2023).
- [54] Inc. Varian. *VNMRJ Command and Parameter Reference*. Rev B 1207. Pub. No. 01-999346-00, Rev. B 1207. Technical writer and editor: Everett Schreiber. Varian, Inc., 2007. URL: <https://www.agilent.com/cs/library/usermanuals/public/0199934600b.pdf>.
- [55] C.H.S. Vieira et al. “Exploring quantum thermodynamics with NMR”. In: *Journal of Magnetic Resonance Open* 16–17 (Dec. 2023), p. 100105. ISSN: 2666-4410. DOI: [10.1016/j.jmro.2023.100105](https://doi.org/10.1016/j.jmro.2023.100105). URL: <http://dx.doi.org/10.1016/j.jmro.2023.100105>.
- [56] Ye Wang et al. “Single-qubit quantum memory exceeding ten-minute coherence time”. In: *Nature Photonics* 11.10 (Sept. 2017), pp. 646–650. DOI: [10.1038/s41566-017-0007-1](https://doi.org/10.1038/s41566-017-0007-1).
- [57] Mark Wilde. *Quantum Information Theory*. Vol. 23. Publication Title: Foundations in Signal Processing, Communications and Networking. 2021. ISBN: 978-1-107-17616-4. DOI: [10.1007/978-3-030-62938-0_4](https://doi.org/10.1007/978-3-030-62938-0_4).
- [58] Bin Yan and Nikolai A. Sinitsyn. “Analytical solution for nonadiabatic quantum annealing to arbitrary Ising spin Hamiltonian”. In: *Nature Communications* 13.1 (Apr. 2022). ISSN: 2041-1723. DOI: [10.1038/s41467-022-29887-0](https://doi.org/10.1038/s41467-022-29887-0). URL: <http://dx.doi.org/10.1038/s41467-022-29887-0>.
- [59] Manjin Zhong et al. “Optically addressable nuclear spins in a solid with a six-hour coherence time”. In: *Nature* 517.7533 (Jan. 2015), pp. 177–180. DOI: [10.1038/nature14025](https://doi.org/10.1038/nature14025).

Appendix

APPENDIX A

Appendix 1: Wilbraham-Gibbs Constant in the square function example

The following calculations are pretty straightforward, and are intended to show the numeric value of the overshoot in Figure 18, i.e., for the Fourier series of the square of height l and width $2T_1$, assuming periodicity of $4T_1$. At first I did not intend to write them here, but as most examples I found used the fact that the partial sum of S_N can be written as

$$S_N(t) = \frac{l}{2} + l \cdot \sum_{n=1}^N \frac{\sin\left(\frac{\pi n}{2}\right)}{\left(\frac{\pi n}{2}\right)} \cos\left(\frac{\pi n}{2T_1}t\right) \quad (\text{A.1})$$

$$= \frac{l}{2} + l \cdot \sum_{n=1}^N Sinc\left(\frac{\pi n}{2}\right) \cos\left(\frac{\pi n}{2T_1}t\right), \quad (\text{A.2})$$

and that, near the discontinuity, with $t = T_1/2N$, in the limit of $N \rightarrow \infty$ the expression could be approximated by a Riemannian sum¹. As the reader may agree, I found that taking the limit of $N \rightarrow \infty$ in a expression that we wish to show properties only when N is finite defeats the purpose of the demonstration. Let us proceed in a different manner.

The maximum of the square function is l . On the other hand, being S_N a smooth function, we can find the maxima by taking its derivative

$$S'_N = l \sum_{n=1}^N \sin\left(\frac{n\pi}{2}\right) \sin\left(\frac{n\pi}{2T_1}t\right)$$

using trigonometric identities for the sum of angles of the sine,

¹ The reader may refer to the Wikipedia page for the Gibbs Phenomenon to evaluate a similar example.

$$\sum_{n=1}^N \sin\left(\frac{n\pi}{2}\right) \sin\left(\frac{n\pi}{2T_1}t\right) = \sum_{n=1}^N \cos\left(\frac{n\pi}{2}(1 + \frac{t}{T_1})\right) + \cos\left(\frac{n\pi}{2}\right) \cos\left(\frac{n\pi}{2T_1}t\right)$$

where the second term in the sum is zero. Using the following trigonometric identity

$$\sum_{n=0}^N \cos n\theta = \frac{\sin \frac{\theta}{2} + \sin\left((N + \frac{1}{2})\theta\right)}{2 \sin \frac{\theta}{2}},$$

we are left with

$$-1 + \sum_{n=0}^N \cos\left(\frac{n\pi}{2}(1 + \frac{t}{T_1})\right) = -1 + \frac{1}{2} + \frac{\sin\left(\frac{\pi(N+1)}{2}(1 + \frac{t}{T_1})\right)}{2 \sin\left(\frac{\pi}{2}(1 + \frac{t}{T_1})\right)} = 0,$$

then

$$\sin\left(\frac{\pi(N+1)}{2}(1 + \frac{t}{T_1})\right) = \sin\left(\frac{\pi}{2}(1 + \frac{t}{T_1})\right),$$

which can be written as

$$\sin\left(\frac{\pi N}{2}(1 + \frac{t}{T_1}) + \frac{\pi}{2}(1 + \frac{t}{T_1})\right) = \sin\left(\frac{\pi}{2}(1 + \frac{t}{T_1})\right).$$

This equation is satisfied when

$$\frac{\pi N}{2}(1 + \frac{t}{T_1}) = 2k\pi, \quad \forall k \in \mathbb{Z}.$$

So the maxima must be when

$$t = T_1\left(\frac{2k}{N} - 1\right). \tag{A.3}$$

Given that N is finite, and t bounded by the period $4T_1$, one can cycle through all k and find the global maximum. Or by examining the Figure 18, it is clear that it is near $t = \pm T_1$. The closest one should be the largest, and is exactly when

$$t_m = T_1 - \frac{2T_1}{N}, \tag{A.4}$$

i.e., when the fastest oscillating term is halfway through its periodicity.

Finally, by calculating the overshoot as the difference between the function and the partial Fourier sum, we obtain

$$|f(t_m) - S_N(t_m)| = l \cdot (0.089489872236 \dots) \tag{A.5}$$

as expected.